Ultrashort and Ultraintense Electromagnetic Pulses

Inaugural-Dissertation

zur Erlangung des Doktorgrades
der Mathematisch-Naturwissenschaftlichen Fakultät
der Heinrich-Heine-Universität Düsseldorf

vorgelegt von

Daniel an der Brügge
aus Essen

Dezember 2010

aus dem Institut für theoretische Physik I
der Heinrich-Heine-Universität Düsseldorf

Gedruckt mit der Genehmigung der Mathematisch-Naturwissenschaftlichen Fakultät der Heinrich-Heine-Universität Düsseldorf

Referent: Prof. Dr. A. Pukhov

Koreferenten: Prof. Dr. K.-H. Spatschek und Prof. Dr. G. Paulus

Tag der mündlichen Prüfung:

Contents

Chapter 1

Introduction and Background

In the last centuries, physics has constantly been extending its frontiers towards the extremes. Astrophysical theories deal with the universe as a whole and particle physics describes structures in the sub-nucleon range. Regarding ultrafast processes, we are now living in an era, in which femtosecond (1fs $= 10^{-15}$s) and even attosecond ($1\,\mathrm{as} = 10^{-18}\,\mathrm{s}$) time scales start to become accessible to scientific investigation. In order to observe anything happening in such an exceedingly short period of time, it is necessary to have a "camera" or a "flash light" with an "exposure time" in the same order of magnitude. This work deals with the physics of such "flash lights".

Let us now begin with a brief look at the development of ultrashort and ultraintense lasers and their applications.

1.1 Development of Ultrashort Relativistic Laser Pulses

In the 1980's, the invention of the "Chirped Pulse Amplification" (CPA) technique lead to the opening of an entirely new area of research: the physics of relativistic laser-plasma interaction. Using the CPA technique, electromagnetic energy can be focused in both time and space to reach unprecedented intensities. The fields are so strong that an electron inside the field will be accelerated to almost the speed of light within a time shorter than an optical half-cycle, which for visible light is in the order of a femtosecond ($10^{-15}\,\mathrm{s}$). The history of ultrashort relativistic laser pulses started in 1985 with the invention of the CPA technique by Strickland and Mourou [1]. The principle of this technique is not hard to explain.

We start with an extremely short, but low energy light pulse, as it can for example be generated by a Ti:Sa-laser, making use of mode-locking. The possibility of amplifying these pulses directly is limited. Because of their extreme shortness, their intensity becomes extremely high already at moderate energies. Intensities of some gigawatts per square centimetre would

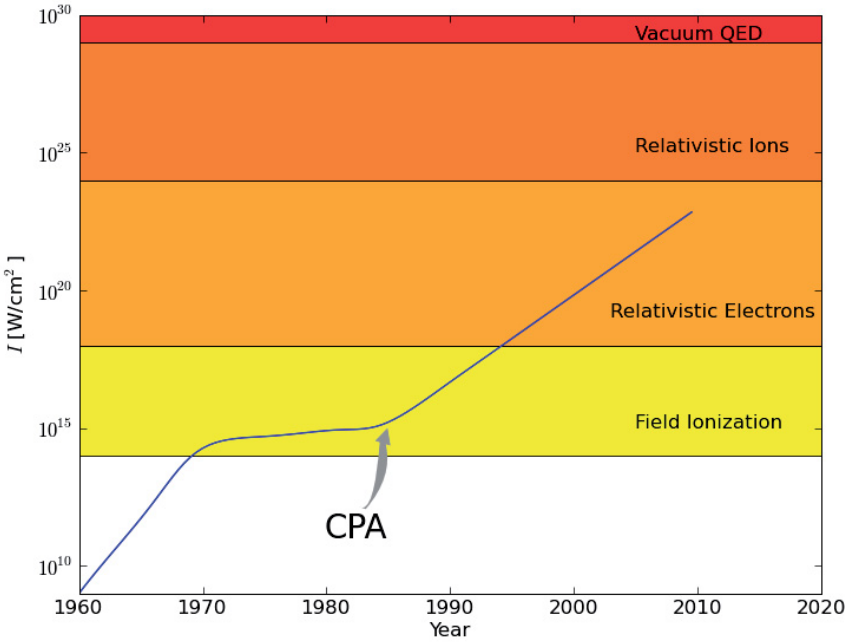

Figure 1.1: Schematic diagram of the history of highest intensity laser pulses

damage the gain medium so that amplification is not possible in the usual way. Therefore, the pulse has to be stretched in a controlled manner, so that the energy density goes down without losing the pulse energy. The stretching is done by adding a "chirp", i.e. a controlled temporal variation of the frequency, to the pulse phase. In this way, the stretching is reversible. The chirped pulse is then amplified using either a conventional laser amplifier or optical parametric amplification [2] in a nonlinear crystal. The latter case promises to allow for even higher intensities than conventional CPA and is referred to as OPCPA (optical parametric chirped pulse amplification). After the amplification stage, the pulse is compressed again, and is ready to be focused to the target of interest.

Figure 1.1 shows the historical development of the highest reachable laser intensities schematically. The physics of laser-plasma interaction started off in the 1970's, when laser fields became strong enough to directly ionize matter. A good introduction to the physics of laser-plasma interaction in the sub-relativistic regime is given in the book by Kruer [3].

In the mid-eighties the invention of CPA put an end to a temporary stagnation in the development of high intensity lasers. Eventually this brought laser-plasma physics to a new level: the laser-plasma became relativistic. In this regime, it is convenient to characterize the laser field with the dimen-

sionless parameter $a_0 \equiv eA_0/m_e c^2$, where A_0 is the peak vector potential of the pulse. a_0 corresponds to the maximum transverse momentum an electron gains inside the laser field in units of $m_e c$. Today relativistic laser-plasma physics can be explored even in university scale labs, e.g. the ARCTURUS laser system at the university of Düsseldorf is able to produce fields of about $a_0 \sim 10$. A broad overview of phenomena in this regime is found in Ref. [4].

The next big step will be accomplished when laser fields reach a strength of $a_0 \sim 1000$. At that point, not only the electrons, but also the ions will directly be accelerated to relativistic velocities. The European ELI (extreme light infrastructure) project [5], which at the moment is in its preparatory phase, aims at this regime.

When the laser field approaches the Schwinger limit [6] of $8 \times 10^{18}\,\mathrm{V/m}$, it will be possible to study electron-positron pair creation and other exotic quantum electrodynamic (QED) effects in vacuum. This corresponds to an intensity of $I \sim 8 \times 10^{30}\,\mathrm{W/cm^2}$, but some signatures of QED, such as vacuum polarization, should already be observable at considerably lower intensities, therefore the limit in Fig. 1.1 was put to $10^{29}\mathrm{W/cm^2}$. Notice also the difference in the units of the threshold parameters: Whereas for the electrons or ions to become relativistic, a_0 respectively $I\lambda^2 \propto a_0^2$ is the crucial quantity, in the case of vacuum QED, I itself is important. Thus higher frequencies, which can be focused down to smaller spots, are not very suitable to easily observe ion relativistic effects, but can in principle very well be used to approach the Schwinger limit. High harmonics generated at solid surfaces may provide a means to reach this limit in not-so-distant future. We explain the possibility of coherent harmonic focusing in chapter 3.

1.2 Relativistic Laser-Plasma Interaction

Light with an intensity of $I > 10^{14}\mathrm{W/cm^2}$ ionizes almost any material almost instantly. Therefore, the interaction of ultraintense lasers with matter has to be understood as *laser-plasma interaction*. Due to the extreme shortness of the laser pulses considered in this work, we are mainly interested in the response of the electrons, which is much faster than the ion response due to their higher charge to mass ratio q/m. The central parameter characterizing the interaction is therefore the electron density n_e. If the electron density is below the critical density $n_e < n_c \equiv \epsilon_0 m_e \omega_0^2/e^2$, so that the laser pulse can propagate inside the plasma, we talk about *underdense* plasmas. This is the case for plasmas generated from gases. For $n_e > n_c$, the laser pulse is reflected and we talk about *overdense* plasma. For laser-plasmas generated from solids, peak densities of the order of $10^2\, n_c$ are typical.

If the product of intensity and the square of the wavelength reaches a value of $I\lambda^2 > 10^{18}\mathrm{W}\,\mu\mathrm{m}^2/\mathrm{cm}^2$, the plasma electrons are accelerated to velocities close to the speed of light c. In this relativistic regime, the boundary

between underdense and overdense is shifted due to the change in the effective electron mass. Now, the governing parameter is $S \equiv n_e/(a_0 n_c)$ with a_0 and n_c as defined above, which separates overdense ($S > 1$) from underdense ($S < 1$) plasmas.

The relativistic character of the interaction gives rise to strongly nonlinear behaviour of the system, opening up the possibility for converting the laser energy to several channels, such as intense XUV or x-ray radiation or quasi-monoenergetic relativistic particle beams.

For example, an intense laser pulse travelling through underdense plasma generates a wake in the plasma density. The longitudinal electric field in this wake can be exploited to accelerate electrons [7]. On top of that, for highly relativistic and sufficiently short laser pulses, that wakefield condenses to a single "bubble" [8, 9]. This bubble captures electrons from the plasma in its field and accelerates them to a quasi-monoenergetic spectrum with energies on the MeV or even GeV scale.

The exposure of overdense plasmas with relativistic light bears further intriguing potential. One of the most exciting phenomena here is the generation of intense high harmonics. The produced radiation can reach up to x-ray frequencies and is coherently emitted in the form of attosecond pulses. Additional interesting features of relativistic laser-overdense plasma interaction are the acceleration of ions and the generation of huge magnetic fields. A comprehensive survey of topics in relativistic laser-plasma interaction according to the state of the art of 2005 is found in Ref. [4].

The use of nano-structured targets can further enhance the possibilities offered by ultra-intense lasers. An example for this are ultrathin foils or nanoscale droplets. If these are hit by a relativistic laser pulse, all electrons are extracted from the material, leading to highly compressed electron bunches travelling within the laser pulse.

1.3 Thesis Outline

The three main topics of this work are covered in the following three chapters, each framed individually by a short introductory section and a final section that summarizes the most important results of the chapter.

Pulses of some of the latest generation lasers are so short that their envelope contains only a few optical cycles. At this point, the classical analytical description of a laser pulse breaks down. Therefore, novel methods to mathematically represent these pulses are needed. In chapter 2 of this thesis[1], a new concept is introduced, tested and discussed. We show that our concept is both clearly superior to more conventional approaches and very convenient for the use in numerical simulations.

[1] Chapter 2 is based on the publication Ref. [10], but it has been largely extended to now also account for arbitrary Hermite-Gaussian modes.

Chapters 3 and 4 both are about the generation of pulses in the attosecond time range, both exploiting non-linear relativistic effects induced by ultraintense laser pulses. However, apart from these commonalities the discussed strategies are different:

Chapter 3 deals with the generation of high harmonics at solid density plasma surfaces[2]. The basic principle of this scheme is as straightforward as it is effective: a relativistically intense ($I\lambda^2 \gg 10^{18}\,\mathrm{W\,cm^{-2}\,\mu m^2}$) laser pulse creates a plasma on a solid surface and is reflected. Due to relativistic nonlinearities in the interaction of the laser pulse with the plasma electrons, the reflected radiation contains harmonics of the fundamental laser frequency. These harmonics are locked in phase and are therefore emitted in the form of attosecond pulses. Despite its apparent simplicity, this process is rich in intriguing physical details.

An alternative scheme consists in driving an electron bunch to high velocities with one high power laser pulse and then scatter a probe pulse at the accelerated electron bunch to upconvert its frequency via the relativistic Doppler effect. This method possibly offers the advantage of enhanced control over the generated pulse structure, since the driver and probe pulses are distinct here. We study this scheme[3] in chapter 4.

A brief conclusion of the whole thesis is found in chapter 5. After that, there is an appendix, describing some of the mathematical techniques used in this thesis.

[2]Parts of chapter 3 are based on the publications [11, 12].

[3]Chapter 4 is based on results that have been presented at the SPIE Europe Optics and Optoelectronics Conference [13].

Chapter 2

Propagation of Ultrashort Electromagnetic Pulses in Vacuum

One of the most fascinating lines of development in laser technology [14] leads to the concentration of electromagnetic energy in smaller and smaller space-time regions. These laser pulses may contain not more than a few optical cycles and can be focused down to a single wavelength - sometimes called the λ^3-regime. Additionally, the ability to control the carrier envelope phase (CEP) of the pulse increased drastically [15, 16]. Possible applications for these well controlled pulses range from high-gradient electron acceleration [17–20] over the generation of ultrashort, coherent x-ray flashes [21–23] to attosecond spectroscopy [24]. At the point where the duration of the pulse approaches its cycle duration, conventional analytical representations of light pulses, based on the assumption of (near-)monochromaticity, break down.

As in the case of extremely focused beams [25, 26], the vectorial character of light gains importance for extremely short pulses. There is an interdependence between the spatio-temporal pulse shape and its polarization which needs to be analyzed carefully. Not all field structures conceivable in a simplified 1D geometry ($\nabla_\perp = 0$) can be realized as finite energy, localized 3D wave packets, as we are going to demonstrate in section 2.1. Commonly used models are shown to be consistent only for a certain choice of the carrier envelope phase (CEP). In consideration of the growing ability to control the CEP and its increasing relevance for short pulses, this is not sufficient. To find a set of realistic wave packet solutions, the *second potential* is introduced, which allows for consistent analytical representation of arbitrary phased and polarized electromagnetic wave packets.

To complete the analytical description, we need a solution of the scalar wave equation in an approximation that is adequate for extremely short, focused pulses. In our approach (section 2.2) we follow the work of Porras

[27] and employ the analytic signal. The results are written down in a closed analytical form. The presented, handy form is particularly convenient for use in numerical simulations. We also generalize the solution to arbitrary Hermite-Gaussian modes, including radially polarized ones. Because of their strong and purely longitudinal fields on the optical axis, radially polarized pulses appear to be highly interesting for electron acceleration [19, 20]; this idea will be followed up on in chapter 4.

In section 2.3, all solutions undergo rigorous numerical testing. Any significant error would show up after the solutions have been propagated by the self-consistent electromagnetic field solver. It turns out that the new pulse representation is clearly superior to the standard approach in the sense that it produces by far less artifacts both at the pulse initialization region and at the region of the propagated pulse.

2.1 Second Potential Representation

In this section, we introduce the second potential as a straightforward method to transform a localized, finite energy (square integrable) solution of the scalar wave equation into a localized, finite energy solution of the complete set of Maxwell equations. As we will see, this task is not fulfilled by simply assigning the scalar wave solution to a component of one of the fields or potentials. Therefore, the second potential is, besides its practical use, also of fundamental physical significance.

It is well known, that an electromagnetic pulse can be represented by its four-potential $A^\alpha = (\phi, \mathbf{A})$. Each component satisfies the vacuum wave equation: $\Box A^\alpha = 0$. We use the Lorenz gauge $\partial_\alpha A^\alpha = 0$ and further set the scalar potential to zero $\phi = 0$, which can be done in vacuum without loosing generality. Because of $\phi = 0$, the Lorenz gauge coincides with the Coulomb gauge

$$\nabla \cdot \mathbf{A} = 0 \tag{2.1}$$

here. Now the fields are written as $\mathbf{E} = -c^{-1}\partial_t \mathbf{A}$ and $\mathbf{B} = \nabla \times \mathbf{A}$. We are interested in finite energy pulse-like structures, so that $\mathbf{A}$ may be required to be a localized function: $|A| \to 0$ for $r \to \infty$. Thereby, the vector potential is uniquely defined. This can be seen since any change of $\mathbf{A}$ that meets the above conditions would result in measurable changes in the electric or magnetic fields.

In laser physics, it is common to choose an analytical solution to the wave equation for the main, i.e. transverse components of the pulse. Then the longitudinal component can be determined via integration: $A_z = \int_z^\infty \nabla_\perp \cdot \mathbf{A}_\perp dz$. However, this integral can yield a non-vanishing longitudinal potential component far from the actual pulse region, since commonly used solutions to the wave equation do not satisfy the condition

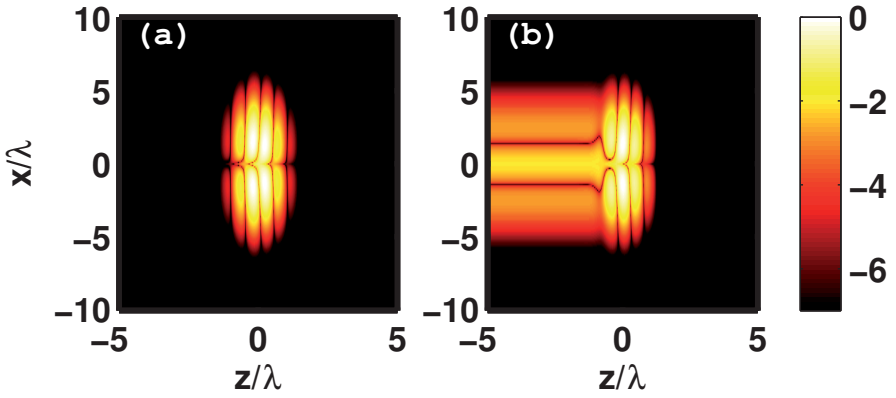

Figure 2.1: Logarithm of the square transverse magnetic field $\log_{10}\left((B_y/B_0)^2\right)$ in the $y = 0$ plane resulting from an ultrashort, linearly polarized, (a) sine- and (b) cosine-phased Gaussian potential. The pulse duration is $c\tau = 0.5\,\lambda$ and focal spot width $\sigma = 2\,\lambda$.

$$\int_{-\infty}^{\infty} \nabla_\perp \cdot \mathbf{A}_\perp dz \stackrel{!}{=} 0 \tag{2.2}$$

for ultrashort pulses. This component cannot simply be ignored, but causes non-zero longitudinal electric and transverse magnetic fields, an example of which is shown in Fig. 2.1b. Although these fields have a small amplitude of the order $\mathcal{O}\left((c/\omega\sigma)^2\right)$, they in fact even contain an infinite amount of energy because of their infinite extension.

To get a realistic finite energy pulse, the choice of the transverse vector potential is restricted by Eq. (2.2). This is a fundamental difference to the 1D case, where such a restriction on the waveform does not exist. Before the consequences of this restriction are discussed in detail, let us introduce the second potential $\mathbf{\Psi}$, which enables us to describe a reasonable set of realistic pulse structures in a more convenient way. We simply define it as the vector potential to the vector potential, thus:

$$\nabla \times \mathbf{\Psi} \equiv \mathbf{A}. \tag{2.3}$$

Of course, each component of $\mathbf{\Psi}$ has to satisfy the wave equation $\Delta\Psi_i - \frac{1}{c^2}\partial_t^2\Psi_i = 0$. Then, the wave equation for $\mathbf{A}$ and the Coulomb gauge readily follow from Eq. (2.3) and there are no restrictions like (2.2) on the choice of the second potential components. This means that, unlike the components of the vector potential which are unique but still coupled by Eq. (2.1), the components of the second potential are completely decoupled but not uniquely determined.

To bridge the gap from the second potential to more classical representations of electromagnetic radiation, it proves useful to split $\mathbf{\Psi}$ up into its

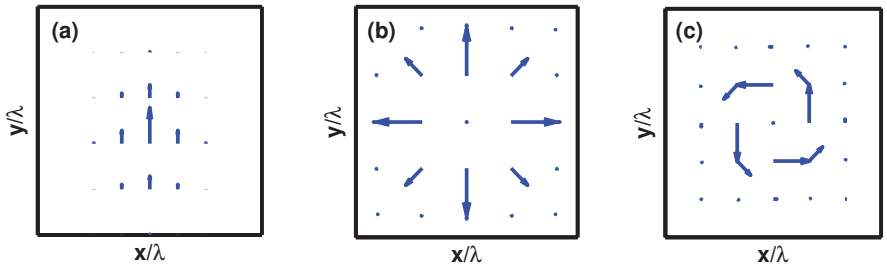

Figure 2.2: Schematic diagrams visualizing the difference between (a) linear/circular/elliptic, (b) radial and (c) azimuthal polarization. The diagrams depict characteristic electric field structures in a plane orthogonal to the beams propagation direction.

longitudinal component $\hat{\mathbf{e}}_z \cdot \mathbf{\Psi}$ and its transverse component $\hat{\mathbf{e}}_z \times \mathbf{\Psi}$. For a large class of laser pulses, it is convenient to choose $\hat{\mathbf{e}}_z \cdot \mathbf{\Psi} = 0$. Then Eq. (2.3) becomes $A_z = -\nabla_\perp \cdot (\hat{\mathbf{e}}_z \times \mathbf{\Psi})$ and $\mathbf{A}_\perp = \hat{\mathbf{e}}_z \times \partial_z \mathbf{\Psi}$. In the near-monochromatic case $\partial_z \sim -i\omega/c$ we get $\hat{\mathbf{e}}_z \times \mathbf{\Psi} \approx ic\mathbf{A}_\perp/\omega$, hence in the long pulse limit the transverse component $\hat{\mathbf{e}}_z \times \mathbf{\Psi}$ is, except for a constant complex factor, identical with the transverse components of the vector potential.

Let us point out that each electromagnetic pulse in vacuum can be represented solely by the *transverse component of the second potential*, subsequently abbreviated as TSP. This is easily seen, since it can be obtained by taking the integral $\hat{\mathbf{e}}_z \times \mathbf{\Psi} = \int_z^\infty \mathbf{A}_\perp dz'$ from an arbitrary vector potential in Coulomb gauge. To make the representation unique, we demand the condition $|\mathbf{\Psi}| \to 0$ for $|\mathbf{r}| \to \infty$ in the half-space $x > 0$, so that $\hat{\mathbf{e}}_z \times \mathbf{\Psi}$ is unambiguously given by the just mentioned integral. Then, for a vast class of laser pulses including all linearly, circularly and radially polarized modes, $\mathbf{\Psi}$ will vanish at infinity in all directions. To understand this, we write the integral condition (2.2) in terms of the TSP:

$$\nabla_\perp \cdot \left(\hat{\mathbf{e}}_z \times \mathbf{\Psi}|_{z=-\infty} \right) = 0. \tag{2.4}$$

In general, it possesses non-trivial solutions, corresponding to structures, where the fields produced by $\mathbf{\Psi}$ at $z \to -\infty$ vanish, but $\mathbf{\Psi}$ itself does not.

However, we look at important special cases. For linear polarization ($\Psi_x = 0$), one can easily show that Eq. (2.4) has none but the trivial solution. The same is true for circular polarization, which we define by $\Psi_y = i\Psi_x$, and the components are assumed to be analytical functions. Eq. (2.2) then only has solutions of the type $\Psi(x + iy)$, so there is no non-trivial solution that fulfils the boundary condition. For both linear and circular, and also the more general case of elliptic polarization, the electric field vector points in the same direction everywhere in one plane transverse to the propagation

direction, see Fig. 2.2a. Another interesting structure is the radially polarized pulse, see Fig. 2.2b. With the help of the TSP it can be represented as $\hat{\mathbf{e}}_z \times \mathbf{\Psi} = f(r_\perp, z, t)\mathbf{r}_\perp$. Again, there is no non-trivial finite energy solution to (2.4) of this form.

Summarizing, for realistic linearly, circularly or radially polarized pulses, the condition Eq. (2.2) simply reduces to:

$$\hat{\mathbf{e}}_\mathbf{z} \times \mathbf{\Psi}|_{z=-\infty} = \int_{-\infty}^{\infty} \mathbf{A}_\perp dz \stackrel{!}{=} 0. \tag{2.5}$$

In other words, all localized linearly, circularly and radially polarized electromagnetic pulses can be represented by a localized TSP.

Commonly used analytical wave packet solutions do in general not fulfil the above condition when directly assigned to $\mathbf{A}_\perp$. Take, for instance, a pulse with a Gaussian longitudinal profile, $A_y(x = 0,\, y = 0,\, z,\, t = 0) = a_0 \exp\left[-(z/c\tau)^2\right] \cos(2\pi z/\lambda)$, then $|\Psi_x(z = -\infty)| = a_0 c\tau\pi^{1/2} \exp\left(-(c\tau/2\lambda)^2\right) \neq 0$, meaning that some field components would extend to infinity as in Fig. 2.1. Unlike the cosine-phased Gaussian, the sine-phased potential may in principle be used for A_y, as the integral vanishes here [see also Fig. 2.1(a)]. Assigning an exact Gaussian profile to the transverse electric field directly instead of the vector potential does not help. Rather, by calculating the second potential of such a pulse it is not hard to prove that this structure does not exist for *any* phase.

Besides for the representation of linearly, circularly or radially polarized pulses as shown above, the TSP could in principle also be used for the representation of azimuthally polarized pulses [Fig. 2.2(c)]. Therefore, one could choose $\hat{\mathbf{e}}_z \times \mathbf{\Psi} = f(r_\perp, z, t)\hat{e}_\varphi$. Notice that this interesting mode does not produce any longitudinal field at all. However, for this sort of function Eq. (2.4) possesses non-trivial solution, meaning that the TSP does not have to vanish as $z \to -\infty$ for each localized pulse shape. Therefore, this kind of structure is more generally represented by the longitudinal component $\hat{\mathbf{e}}_z \cdot \mathbf{\Psi}$ of the second potential instead of the transverse one. E.g., assigning a Gaussian profile to $\hat{\mathbf{e}}_z \cdot \mathbf{\Psi}$ yields an Hermite-Gaussian TE_{01} mode with azimuthally polarized electric field.

2.2 Solution of the Wave Equation for Short Pulses

In the previous section, we reduced the problem of finding a pulse-like solution to the Maxwell equations to the easier problem of finding a sufficiently accurate solution to the scalar wave equation $\Box\Psi = 0$. But also the commonly used solutions of the scalar wave equation are not appropriate for extremely short pulses, as they generally make use of the assumption of quasi-monochromaticity. We now look for more appropriate solutions. They later may be inserted for an arbitrary component of $\mathbf{\Psi}$.

Fourier transforming the scalar wave equation in time and the spatial directions transverse to the beam propagation direction z yields $\partial_z^2 \tilde{\Psi} = -((\omega/c)^2 - k_\perp^2)\tilde{\Psi}$, with the general solution

$$\tilde{\Psi}(z, \mathbf{k}_\perp, \omega) = \tilde{\Psi}\Big|_{z=0} \exp\left(-iz\sqrt{\left(\frac{\omega}{c}\right)^2 - k_\perp^2}\right). \tag{2.6}$$

Next, the focal spot profile $\tilde{\Psi}(z=0)$ has to be chosen. We are interested in functions that are both physically significant and mathematically handy. Therefore, we consider Hermite-Gaussian modes, which can be defined via the following $\mathbf{k}_\perp$-dependence:

$$\mathrm{HG}_{mn}: \qquad \tilde{\Psi}\Big|_{z=0} \propto k_x^m k_y^n \exp\left[-(k_\perp \sigma/2)^2\right]. \tag{2.7}$$

Here, we introduced the beam waist diameter σ. Note that in general, it may depend on the frequency ω. To be able to analytically carry out the inverse Fourier transformation in the transverse dimensions, we have to Taylor expand the square root in Eq. (2.6). For most focused pulses we can assume $c^2 k_\perp^2 \ll \omega^2$ and then neglect fourth order terms in the Taylor series, thus

$$\sqrt{(\omega/c)^2 - k_\perp^2} \approx \omega/c - c k_\perp^2/(2\omega). \tag{2.8}$$

This is the paraxial approximation. In section 2.3 we show, that this approximation allows us to use focal spot sizes down to $\sigma \sim \lambda$ and still obtain a reasonable accuracy. After inserting Eq. (2.7) into Eq. (2.6), we calculate the inverse Fourier transform in the transverse directions:

$$\hat{\Psi}_{mn}(\mathbf{r}) \propto \left(\frac{\omega\sigma^2}{2cz + i\omega\sigma^2}\right) \partial_x^m \partial_y^n \exp\left[-\frac{r_\perp^2}{\sigma^2 - 2icz/\omega} - iz\omega/c\right]. \tag{2.9}$$

Before we can find out the time dependence of the pulse, it is necessary to choose the frequency dependence of the focal spot size σ. At least three consistent choices seem to be interesting:

1. Constant focal spot size for all frequencies in the spectrum: $\sigma = const.$ Approximately, this is the case for high harmonics generated by relativistic plasma surfaces. We are going to discuss this case in section 3.3.

2. Constant beam divergence $\theta = \lambda/\pi\sigma$ for all frequencies in the spectrum, meaning $\sigma \propto 1/\omega$. This is probably the closest description to conventionally focused laser pulses in experiments.

3. Constant Rayleigh length $z_{Rl} = \pi\sigma^2/\lambda$ for all frequencies in the spectrum, meaning $\sigma \propto 1/\sqrt{\omega}$. This case lies in between the previous two cases. For a few-cycle laser pulse with a moderately broad spectrum the difference to these cases should not be too big.

Since it leads to great simplifications in the analytical representation, the third option is employed here. Therefore, we reformulate Eq. (2.9) in terms of the Rayleigh length z_{Rl}.

Further recall that, unlike in the long-pulse limit, the spectrum of the short pulse varies in space. Thus the frequency dependence of the pulse needs to be introduced at a certain, fixed point in space. The preferred point of a focused laser pulse is clearly the centre of the focal spot, without loss of generality we locate it at $\mathbf{r} = 0$. For even numbered m and n, the function $\hat{\Psi}_{mn}$ does not vanish there, and we simply let $\psi(t)$ be the pulse time dependence at $\mathbf{r} = 0$ and $\tilde{\psi}(\omega)$ its Fourier transform. However, if either m, n or both of them are odd numbers, $\hat{\Psi}_{mn}$ vanishes on the optical axis. In this case we choose $\tilde{\psi}(\omega)$ to be the spectrum in the *immediate surrounding* of $\mathbf{r} = 0$, corresponding to the lowest order of the occurring polynomials in x and y. Taking all this into account we obtain:

$$\hat{\Psi}_{mn}(\mathbf{r},\omega) = \tilde{\psi}(\omega)\,\left(\frac{z_{Rl}}{q}\right)^{1+\frac{m+n}{2}}\,\frac{\mathrm{H}_m\left(\sqrt{\frac{i\omega}{2cq}}x\right)}{\sqrt{i\omega}^{m \bmod 2}}\,\frac{\mathrm{H}_n\left(\sqrt{\frac{i\omega}{2cq}}y\right)}{\sqrt{i\omega}^{n \bmod 2}}\,\exp\left[-i\omega\left(\frac{r_\perp^2}{2cq}+\frac{z}{c}\right)\right], \tag{2.10}$$

where $\mathrm{H}_n(\xi) = (-1)^n \exp(\xi^2)\frac{d^n}{d\xi^n}\exp(-\xi^2)$ are the Hermite polynomials and $q \equiv z + iz_{Rl}$ is the complex confocal parameter.

Now, we can carry out the inverse Fourier transformation in time. Note that, for any choice of m and n, Eq. (2.10) contains exclusively integer powers of ω. In the time domain, these factors translate into derivatives. The exponential factor of the form $\exp(-i\omega a)$ simply leads to an, albeit complex, shift in the argument of $\psi(t)$.

We write down the final 3D solution for an arbitrary transverse Hermite-Gaussian mode in the space-time domain with a completely general temporal profile:

$$\Psi_{mn}(\mathbf{r},t) = \left(\frac{z_{Rl}}{q}\right)^{1+\frac{m+n}{2}}\,\frac{\mathrm{H}_m\left(\sqrt{\frac{\partial_t}{2cq}}x\right)}{\sqrt{\partial_t}^{m \bmod 2}}\,\frac{\mathrm{H}_n\left(\sqrt{\frac{\partial_t}{2cq}}y\right)}{\sqrt{\partial_t}^{n \bmod 2}}\,\psi\left(t-\frac{z}{c}-\frac{r_\perp^2}{2cq}\right). \tag{2.11}$$

The roots of ∂_t in the denominator may seem awkward at first glance, but the interpretation is straightforward. After inserting the Hermite polynomials and reducing the fractions, only integer powers of ∂_t remain. The resulting linear differential operators are then applied to the complex function ψ.

In complete analogy we can derive the 2D solutions, with the field $\boldsymbol{\Psi}$ varying in only one transverse direction x. This may come in handy particularly for numerical simulations:

$$\Psi_m^{\mathrm{2D}}(\mathbf{r},t) = \left(\frac{z_{Rl}}{q}\right)^{\frac{1+m}{2}}\,\frac{\mathrm{H}_m\left(\sqrt{\frac{\partial_t}{2cq}}x\right)}{\sqrt{\partial_t}^{m \bmod 2}}\,\psi\left(t-\frac{z}{c}-\frac{x^2}{2cq}\right). \tag{2.12}$$

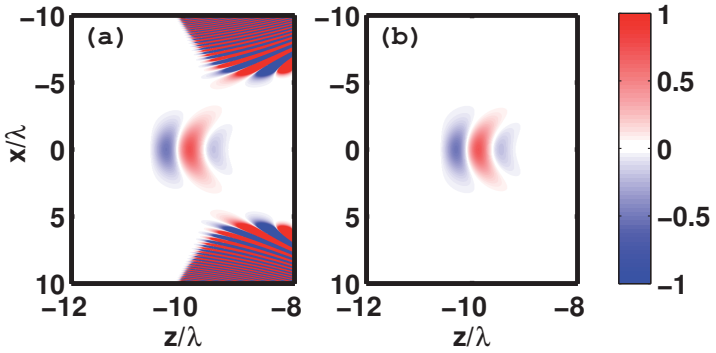

Figure 2.3: Direct comparison of a two dimensional cut through the complete scalar short-pulse solution (2.11) using (a) the "naive" choice $\psi(t') = \exp\left(-t'^2/\tau^2 + i(\omega_0 t' + \phi)\right)$ and (b) the analytic signal Eq. (2.13). Pulse parameters are: $c\tau = 0.5\,\lambda$, $\sigma = 2\,\lambda$, $ct = -10\,\lambda$ (before focus) and $m = n = 0$ (Gaussian mode).

Another, seemingly simpler way to obtain valid, Hermite-Gaussian-like short-pulse paraxial solutions is to start from the plain Gaussian $m = n = 0$ mode and simply apply spatial derivatives ∂_x and ∂_y to it. However, for these solutions the temporal profile at (respectively around) $\mathbf{r} = 0$ is not given by $\psi(t)$ anymore.

One last obstacle has to be overcome before the solutions (2.12) and (2.11) can be put in use: The temporal pulse profile $\psi(t)$ has to be consistently extended to complex arguments $t' = t - z/c - x^2/2cq$. Some care has to be taken here. Let us consider a Gaussian temporal profile for example. Naively choosing $\psi(t') = \exp\left(-t'^2/\tau^2 + i(\omega_0 t' + \phi)\right)$ yields a solution diverging for big $r_\perp$ as $\mathcal{O}(\exp(r_\perp^4))$.

To see how the extension of $\psi(t)$ to complex arguments can be done properly, we reconsider the representation in the frequency domain Eq. (2.10). Having a closer look at the real part of the argument of the exponential function, we notice that it behaves as $-C\omega r_\perp^2$, with $C > 0$. It is now evident, that negative frequencies cause $\mathbf{\Psi}$ to diverge for $r_\perp \to \infty$ and we cannot allow for finite values of $\tilde{\psi}(\omega)$ at any $\omega < 0$. This is actually a consequence of the paraxial approximation, which obviously fails to handle negative frequency components.

Anyway, as shown in Ref. [27], there is an elegant way around this seeming problem. For each real function $u(t)$ it is possible to find exactly one complex representation $\psi(t)$ with $\mathrm{Re}(\psi(t)) = u(t)$ and $\tilde{\psi}(\omega) = 0$ for $\omega < 0$. This complex representation is known as the *analytic signal* (see Appendix A.2).

For a Gaussian pulse $u(t) = \exp(-t^2/\tau^2)\cos(\omega_0 t + \phi)$ it is possible to calculate a closed analytic expression for the analytic signal:

$$\psi\left(t'\right) = \psi_0 \frac{e^{-\overline{\tau}^2}}{2}\left(e^{i\phi} w\left(\frac{t'}{\tau} - i\overline{\tau}\right) + e^{-i\phi} w\left(\frac{t'}{\tau} + i\overline{\tau}\right)\right), \tag{2.13}$$

wherein $\overline{\tau} = \omega_0\tau/2$ and $w\left(z\right) = \exp(-z^2)\mathrm{erfc}(-iz)$ is the complex error (or Faddeeva) function [28]. The analytic signal of the Gaussian pulse was also calculated in Ref. [27], but Eq. (27) from Ref. [27] disagrees with (2.13) for $\mathrm{Im}(t') \neq 0$. Analytical and numerical tests show, that (2.13) is the correct solution. Please note also, that the form of representation chosen in Eq. (2.13) is very convenient for numerical applications since both summands vanish independently for $\mathrm{Im}(t') \to +\infty$. Thus there is no trouble with subtracting two large numbers. If we do not require the temporal profile to be *exactly* Gaussian, it is even possible to drop the generally much smaller second summand. Further, besides the exactly Gaussian real part of Eq. (2.13), the near-Gaussian imaginary part may also be used. This insight is particularly useful for representing circularly and elliptically polarized light.
Figure 2.3 serves to illustrate the meaning of (2.13) and its difference to the naive choice $\psi(t') = \exp\left(-t'^2/\tau^2 + i(\omega_0 t' + \phi)\right)$. In the region near the optical axis, $\mathrm{Im}(t')$ is small and the solutions agree almost completely. However, for bigger $r_\perp$ the naive solution [Fig. 2.3(a)] diverges, while the one using the analytic signal [Fig. 2.3(b)] shows a proper beam-like behaviour and vanishes.

Finally we consider some important special cases of Eqs. (2.11) and (2.12) more explicitly. Besides the very common linearly polarized Gaussian mode TEM_{00}, the radially polarized mode TM_{01} is of high interest, compare chapter 4. For those two cases, the focal spot profile in terms of the second potential $\mathbf{\Psi}$ can be written down as:

$$\hat{\mathbf{e}}_z \times \tilde{\mathbf{\Psi}}\Big|_{z=0} = \tilde{\psi}(\omega)\, \exp\left[-\left(\frac{r_\perp}{\sigma}\right)^2\right] \begin{cases} \mathbf{r}_\perp & \mathrm{TM}_{01} \\ \hat{\mathbf{e}}_x & \mathrm{TEM}_{00} \end{cases}. \tag{2.14}$$

This corresponds to the $m = n = 0$ mode in Eq. (2.11), respectively to a superposition of an $m = 1$ and $n = 0$ mode in Ψ_x and an $m = 0$ and $n = 1$ in Ψ_y. Renormalizing the solutions from Eqs. (2.11) and (2.12) for convenience, we obtain:

$$\hat{\mathbf{e}}_z \times \mathbf{\Psi}\left(\mathbf{r}, t\right) = \mathrm{Re}\left[\left(\frac{z_{Rl}}{q}\right)^g \psi\left(t - \frac{z}{c} - \frac{r_\perp^2}{2cq}\right)\right] \begin{cases} \mathbf{r}_\perp & \mathrm{TM}_{01} \\ \hat{\mathbf{e}}_x & \mathrm{TEM}_{00} \end{cases}. \tag{2.15}$$

Here $g = 1$ for a linear ($g = 0.5$ in 2D) and $g = 2$ for a RP ($g = 1.5$ in 2D) laser and $q = z + iz_{Rl}$ is the confocal parameter again. Further interesting special cases are easily derived from Eq. (2.11). Circularly polarized Gaussian pulses can e.g. be constructed by assigning $\Psi_x = \mathrm{Re}\left(\Psi_{00}\right)$ and

$\Psi_y = \mathrm{Im}\,(\Psi_{00})$. An azimuthally polarized TE_{01} mode is created by the use of the longitudinal second potential: $\Psi_z = \mathrm{Re}\,(\Psi_{00})$, $\Psi_x = \Psi_y = 0$.

The short-pulse paraxial wave solutions Eqs. (2.11),(2.12) together with the analytic signal (2.13) and the second potential (2.3) are a powerful and universal tool for the representation of ultrashort, focused electromagnetic pulses down to the few- and even single-cycle regime.

2.3 Numerical Tests

One important application of the new pulse representation given by Eqs. (2.3), (2.11) and (2.13) is the use in numerical simulations. Therefore, it seems just natural to use a numerical solver to practically test them. In this section we demonstrate the validity of the new representation and further prove its superiority to more conventional approaches, utilizing a self-consistent numerical Maxwell solver.

We use the particle in cell (PIC) code VLPL [29]. To begin with, the fields are initialized inside the VLPL simulation grid. Then they are propagated using a standard algorithm on the Yee-mesh. Finally, it is verified if the numerically propagated pulse still agrees with the analytical term, overall or in some key parameters, and furthermore, if unphysical static fields remain at the place, where the pulse was initialized.

2.3.1 Checking the short pulse paraxial wave solution

First we check the correctness of Eqs. (2.11) and (2.13), proving their superiority to a conventional representation often used for numerical simulations. The "conventional", or separable form is a simple product of a monochromatic, transversely Gaussian beam with a Gaussian temporal profile $\Psi_{\mathrm{sep}} = \exp\left(-i\omega_0(t-x) - (t-x)^2/\tau^2 - r_\perp^2/\sigma^2\right)$. Circularly polarized pulses are used, so that the shape can well be seen in the intensity plots, with a duration of $c\tau = \lambda$ and a focal spot width of $\sigma = 2\lambda$. The pulses are focused over a distance of 50λ inside the simulation. In Fig. 2.4, the initial condition and the numerically propagated solution at the focal spot are shown. The product approximation shows strong asymmetric deformation in the focus and the focal field does not reach its analytically specified intensity I_0. In contrast, the proper short pulse solution is nearly perfectly symmetric in the focus and reaches the desired maximum. The presented solution Eqs. (2.11) and (2.13) is clearly superior to the simple product approach.

Depending on the required accuracy, our approach can be used down to focal spot sizes of $\sigma \sim \lambda$. Below that, the paraxial approximation fails. However, focusing a λ^3-pulse ($\sigma = c\tau = \lambda$) over a distance of 50λ with the PIC electromagnetic solver still leads to acceptable results. After the propagation, we obtain a focal intensity of 82% (or 90%, when also using the TSP representation) of the analytically specified value, still with a perfectly

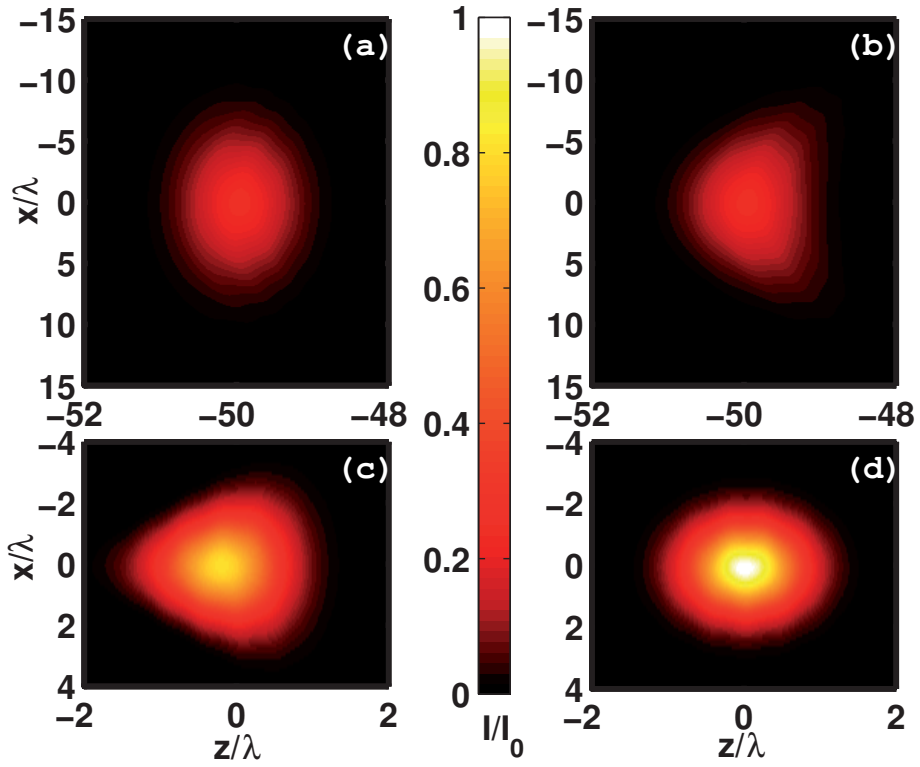

Figure 2.4: Focusing properties of different approximations of the wave equation, evaluated in a 2D version of the PIC code VLPL. (a) and (b) show the intensity distribution as it is initialized inside the code and (c) and (d) show the propagated solution at the focal spot. (a) and (c) use the CW paraxial solution multiplied with a temporal profile, (b) and (d) the correct short pulse solution. The circularly polarized laser pulses are Gaussian both in space and time with duration $c\tau = \lambda$ and width $\sigma = 2\lambda$.

symmetrical spot shape. For comparison: using the product approach in the same kind of simulation, the numerical intensity reaches only 42% of the specified value.

2.3.2 Checking the second potential representation

Now we come to the second potential representation. The alternative to its use is to assign arbitrary wave equation solutions to the transverse components of the vector potential and then make some kind of approximation for the longitudinal part. The simplest possibility is to fully neglect the longitudinal field component, but for strongly focused pulses a somewhat more reasonable approximation can be reached by choosing $A_z = (c/i\omega_0)\nabla_\perp \cdot \mathbf{A}_\perp$. We will call this the "quasi-monochromatic approximation", because it relies on $\partial_z \sim -i\omega_0/c$. This approximation should be preferred to an exact calculation of the longitudinal vector potential component to given transverse potential components, because it at least yields pulse structures with finite energy. Due to the energy conserving property of the field propagator algorithm, the pulse will be forced to self-organize into a consistent structure of finite extension. While this happens, unphysical static fields arise, which tend to make the concerned regions in the simulation domain unusable for further computations. We can describe these fields as being generated by so-called virtual charges. The virtual charge distribution can be estimated analytically in the case of a linearly polarized Gaussian laser pulse. To do this, we calculate the divergence of the vector potential in the quasi-monochromatic approximation. We base our estimate on $A_x \approx A_0 \exp(-i\omega_0 z - (z/c\tau)^2 - (r_\perp/\sigma)^2)$ and apply $A_z = (c/i\omega_0)\partial_x A_x$. The virtual charge distribution is then found to be $\rho_{\mathrm{virt}} = (4\pi)^{-1}\partial_t(\nabla \cdot \mathbf{A}) \approx zxA_x/(c\pi\tau^2\sigma^2)$. Certainly these unphysical charges increase for very short, focused laser pulses. Let us see, if the problem can be cured by the use of the second potential representation.

When employing the second potential representation for an ultrashort pulse, the additional derivative will slightly alter the pulse shape. As shown before, this is inevitable, since a perfectly Gaussian shaped linearly polarized vector potential can exist as an independent structure in vacuum only if it is sine-phased. To make the TSP represented pulse comparable to the conventional one, it is necessary to take care for the frequency shift caused by the z-derivative, which can be estimated as $\omega_{\mathrm{eff}} = \omega_0 + \sqrt{2}/\tau$.

Fig. 2.5 shows the pulses after a short propagation distance in the PIC simulation box. Firstly one observes that, despite of the very short duration, the moving pulse structures (right half of the images) appear very similar in the conventional and the TSP version. Secondly one notices, that the conventional pulse leaves behind a significant amount of virtual charge fields in the initialization region (left half of the images), having both a longitudinal and a transverse component. This undesired phenomenon can neatly be suppressed by the use of the second potential, as seen in panels (b) and (d)

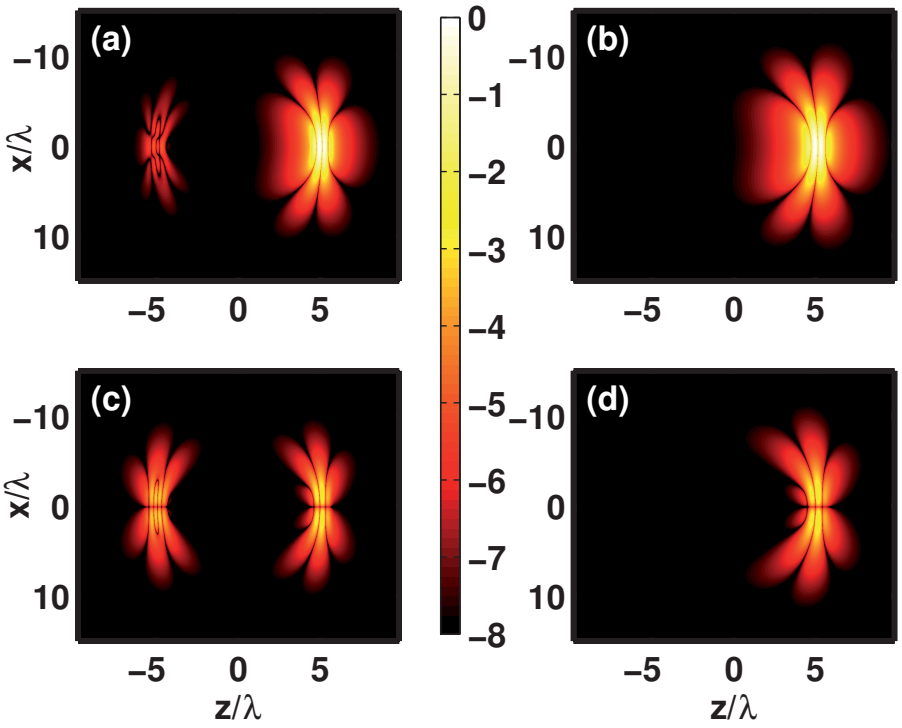

Figure 2.5: Logarithm of the transverse [(a) and (b)] and longitudinal [(c) and (d)] square electric field $\log_{10}\left((E_i/E_0)^2\right)$, $i \in \{x, z\}$ after a propagation time $ct = 10\,\lambda$. The pulses shown in (a) and (c) are Gaussian in the vector potential, the ones in (b) and (d) are Gaussian in the TSP (transverse component of the second potential). Pulse parameters are $c\tau = 0.3\,\lambda$ and $z_{Rl} = 4\pi^2\,\lambda$. For the second potential, a corrected frequency $\omega_0' = \omega_0 - \sqrt{2}/\tau$ was used to take account for the frequency shift caused by the additional derivative.

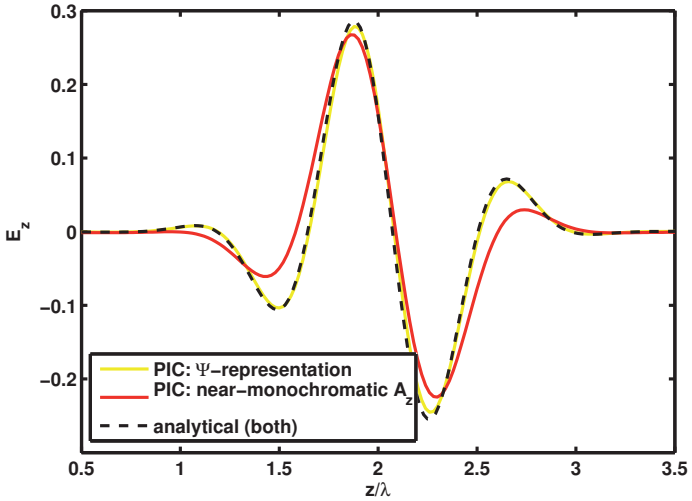

Figure 2.6: The longitudinal pulse field in PIC at the time $c(t-t_0) = 4\lambda$ after initialization, compared to the analytic solution. Once the TSP was used for initialization (yellow or light grey line) and once the near-monochromatic approximation for A_z (red or dark grey line). The differences in the analytical representations are too small to be seen in the diagram, so that both are represented by one curve (dashed black line). Pulse parameters are: $c\tau = 0.5\lambda$, $\sigma = 2\lambda$,

of the figure.

2.3.3 Hermite-Gaussian transverse modes

The next test we want to present concerns the longitudinal field component on the optical axis of a radially polarized pulse, which is of particular interest for vacuum electron acceleration [19, 20]. The pulse length used was $c\tau = 0.5\lambda$, and the focal spot size $\sigma = 2\lambda$. Again, the conventional approach corresponds to a near-monochromatic approximation $A_x = i\nabla_\perp \cdot \mathbf{A}_\perp/\omega$, so as to generate a finite pulse structure from the given transverse field components. The phase ϕ in Eq. (2.13) was chosen as $\phi = 0$ for the second potential representation and as $\phi = \pi/2$ for the conventional representation, so that the pulses are actually comparable. Initially, the longitudinal field nearly agrees for both representations, since the first term of Eq. (2.13), which is the dominating one, is the same in both cases.

In Fig. 2.6 we show the longitudinal field of the pulse after it has left its virtual charges behind. The fields initialized using the conventional representation already differ significantly from the analytical description, whereas the TSP represented fields agree almost perfectly. This will be crucial e.g. when PIC simulations are to be compared with other analytical or semi-

numerical calculations, where the field is inserted analytically and is not self-consistently propagated. Without an exact and reliable pulse representation, such a comparison would hardly be possible.

Finally, we present some pictures of the ultra-short versions of higher order Hermite-Gaussian modes. In Fig. 2.7, 2D Hermite-Gaussian modes derived from Eq. (2.12), up to order $m = 4$ are displayed. Fig. 2.8 shows a collection of views of the 3D TEM_{21} mode. To verify the correctness of the results, we again calculated the pulse fields at a stage before focus analytically and used the electromagnetic solver of the PIC code VLPL to focus the pulse down to a spot size of $\sigma = 2\,\lambda$ over a distance of $10\,\lambda$. If the pulse focuses at the specified location to the specified intensity and further shows the characteristic mode symmetry and profile, we can conclude that our representation has been correct. As can be seen from Figs. 2.7-2.8, all the modes up to $m = 4$ fulfil our expectations.

Conclusion of Chapter 2

We have developed a novel closed form analytical representation of ultrashort, focused laser pulses. It is applicable for durations down to the single-cycle regime and focal spot sizes down to a wavelength. Due to its numerically convenient form and its high accuracy in a wide range of parameters it is ideally suited for use in numerical simulations.

The new representation consists of two parts. First, the laser pulses are represented via the *second potential,* defined by the equation

$$\nabla \times \mathbf{\Psi} \equiv \mathbf{A},$$

which solves the fundamental problem of generating an accurate, actual finite energy solution of the Maxwell equations out of a solution of the three dimensional wave equation. For the practical use in numerical simulations this means, that unphysical "virtual charges" are reduced by orders of magnitude.

The second part of the new representation is a sufficiently accurate solution of the three dimensional scalar wave equation. Therefore, we derived a solution in the short pulse paraxial approximation for arbitrary Hermite-Gaussian modes and arbitrary carrier envelope phase:

$$\Psi_{mn}(\mathbf{r},t) = \left(\frac{z_{Rl}}{q}\right)^{1+\frac{m+n}{2}} \frac{\mathrm{H}_m\left(\sqrt{\frac{\partial_t}{2cq}}x\right)}{\sqrt{\partial_t}^{m \bmod 2}} \frac{\mathrm{H}_n\left(\sqrt{\frac{\partial_t}{2cq}}y\right)}{\sqrt{\partial_t}^{n \bmod 2}} \psi\left(t - \frac{z}{c} - \frac{r_\perp^2}{2cq}\right),$$

where ψ is the analytical signal corresponding to the temporal pulse profile in the centre of the focal spot.

The new representation was tested thoroughly and has been found to be of far superior accuracy compared to conventional product approaches based on the quasi-monochromatic approximation for pulses in the single-cycle regime.

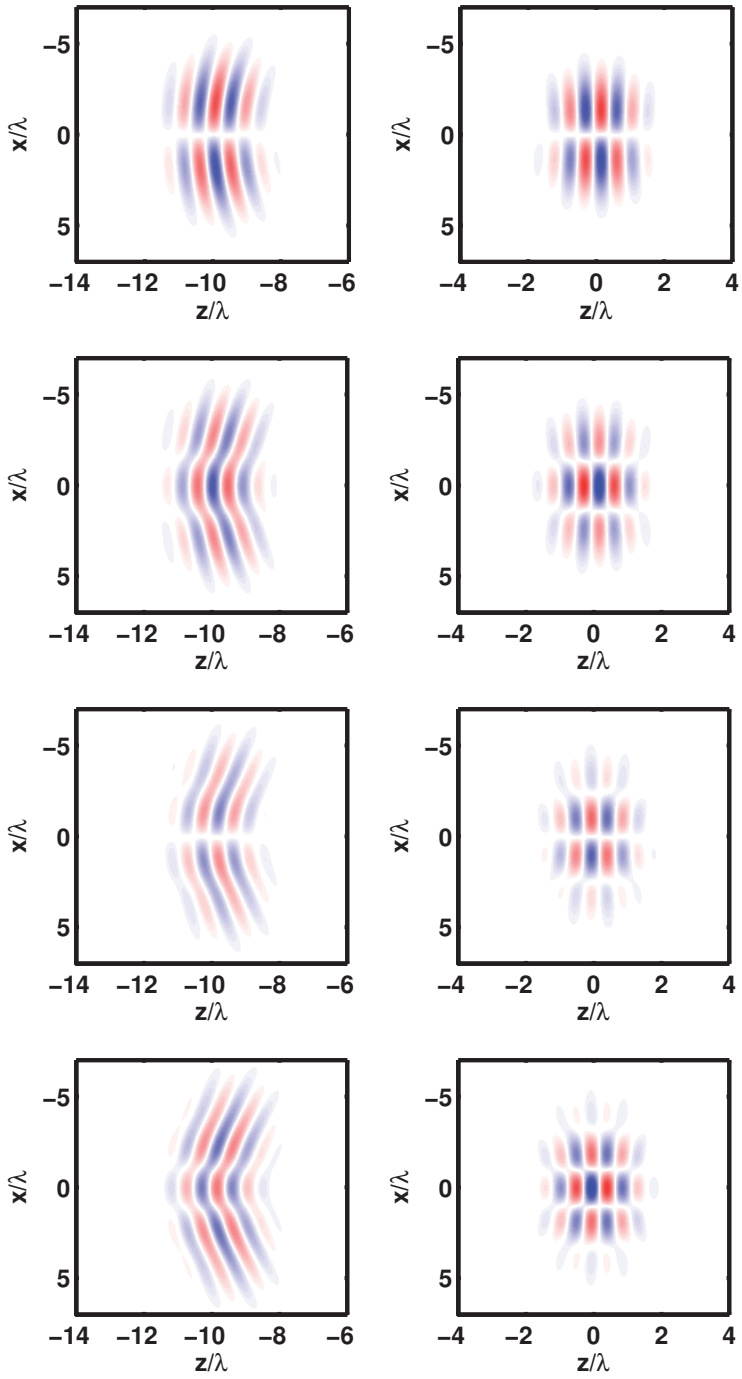

Figure 2.7: 2D Hermite-Gaussian short-pulse modes of order $m \in \{1, 2, 3, 4\}$ (mode number increases from top to bottom), initialized at $z = -10\,\lambda$ before the beam waist employing Eqs. (2.12), (2.13) and (2.3) and then focused by a self-consistent electromagnetic solver. The left column shows the pulses at the initialization stage, the right column after focusing. Pulse parameters are: $c\tau = \lambda$ and $\sigma = 2\,\lambda$.

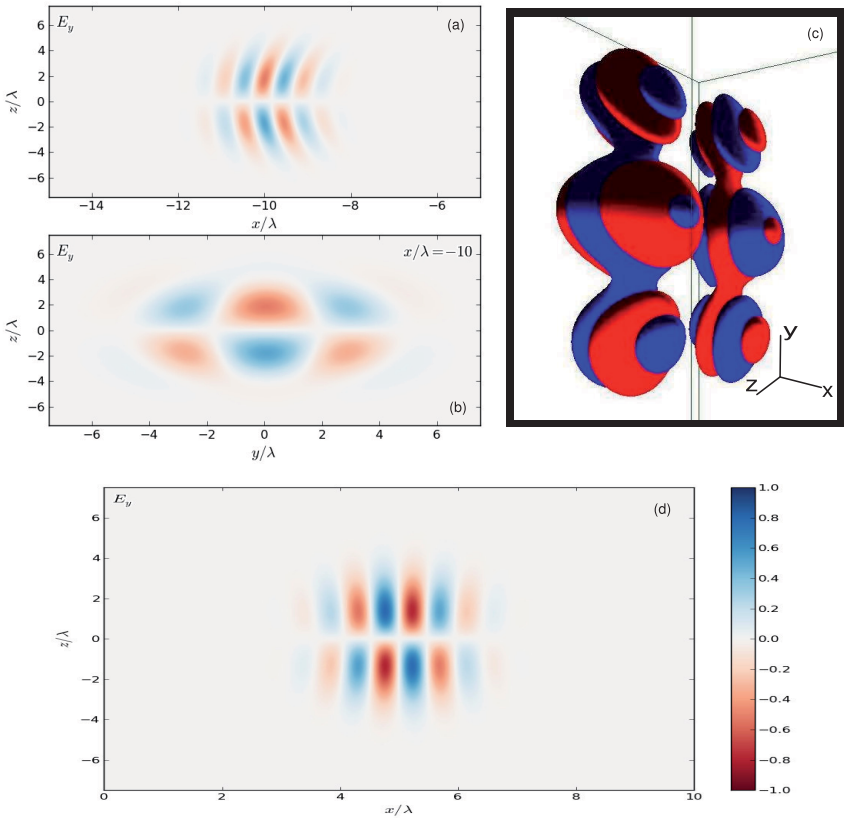

Figure 2.8: Ultrashort 3D Hermite-Gaussian mode TEM_{21}. (a) and (b) are recorded at a time 10 laser periods before the pulse reaches the focal spot, (d) inside the focus and (c) 5 laser periods after the focus. All plots refer to the transverse magnetic field component E_y. The panels (a) and (d) show a cross-section at $y = 0$ (optical axis), (b) displays a cross-section at $x = -10\lambda$. Panel (c) displays surfaces where $E_y = \pm 0.2$ in a 3D perspective view.

Chapter 3

Attosecond Pulses from Relativistic Surface Plasmas

The exciting new possibilities opened up by the advent of femtosecond laser pulses lead us to the question, if it is possible to create even shorter pulses, with durations in the attosecond time range.

One, already well-established way to produce light pulses of attosecond scale duration is the generation of high order harmonics by the non-linear interaction of gas atoms with lasers of intensities slightly above the ionization threshold [30]. This mechanism is however limited to not-too-high laser intensities and low efficiency. Production of coherent attosecond pulses of higher energy could open up the way to entirely new methods of attosecond research such as XUV pump-probe spectroscopy [31]. The currently most promising way towards more intense attosecond pulses is the generation of high order harmonics (HHG) at solid density plasma surfaces.

For a complete understanding of this attosecond pulse generation scheme, it is necessary to study three stages in the laser-plasma interaction process:

Plasma Formation. Before the main laser pulse hits the solid target surface, the pedestal of the pulse already ionizes it and turns it into a plasma. The plasma then thermally expands and at the same time is pushed inside by the laser ponderomotive potential. Depending on the contrast ratio of the laser system and the exact structure of the pre-pulse, this may yield very different surface density profiles. These processes are well understood today and can reliably be simulated by hydro-codes such as Multi-FS [32].

Harmonics Generation. The second stage is the harmonics generation itself. It happens during the interaction of the main laser pulse with the pre-formed plasma density gradient. If the laser pulse duration is in the order of just a few ten femtoseconds or below, the motion of the ions during this period can be neglected, and the interaction takes

place between the laser electromagnetic fields and the plasma electrons.

Diffraction. After the radiation has been emitted from the surface, it will propagate through space. Due to the extremely broad spectrum of the emitted radiation and its coherent phase properties, it is well worth to take a closer look at its diffraction and focusing behaviour.

In section 3.1, we examine the theory of relativistic HHG. Different models are discussed and spectra are analytically derived from the models via asymptotic analysis. The analytical results are substantiated by numerical simulations. We find that the most efficient regime of single pulse HHG is governed by the formation of highly compressed electron nanobunches in front of the surface and results in a slowly decaying spectral power law with an exponent of $6/5$ - instead of $8/3$, as for the previously known relativistic mechanism.

Whereas section 3.1 focuses on the spectral envelope, section 3.2 deals with the fine structure of the high harmonics spectra. This fine structure contains information about the motion of the surface plasma on the femtosecond timescale. Therefore, it provides a useful diagnostic, helping us to gain deeper insight in the relativistic processes involved.

Finally, section 3.3 deals with surface HHG in a realistic 3D geometry. Here, diffraction takes on an important and intriguing role. With carefully designed surfaces or laser pulses we may harness diffraction as a sort of *spatial spectral filter*. With a well designed focusing geometry, it should even be possible to focus the harmonics coherently in both space and time, yielding unprecedented intensities that exceed the intensity of the laser itself by more than a thousand times.

The basic idea for HHG at overdense plasma surfaces has been around for almost thirty years now and endured several generations of high power lasers. In this work, we focus on the most efficient, highly relativistic regime. Before we move on to the actual study, it is worth to have a brief look at the history of the topic.

History

The first observation of high harmonics from plasma surfaces was reported from the Los Alamos Scientific Laboratory [33, 34] in 1981. At that time, huge CO_2 lasers were used at nanosecond pulse duration and the observed radiation was non-coherently emitted into the whole half-space in front of the target. A theoretical explanation for this first observation was given in Ref. [35]. The spectrum extended up to a sharp cutoff, which was found to be the plasma frequency corresponding to the maximum electron density. Therefore, non-linear collective plasma behaviour could be identified as the source of the harmonics. In the strongly inhomogeneous plasma, laser light

was resonantly converted to plasma oscillations, which in turn produced harmonics by sum frequency mixing with the laser light.

For some time then, it became silent around surface HHG, but interest rose again, when the CPA technique, invented in 1985 by Strickland and Mourou [1], revolutionized ultraintense laser science in the 1990's. With the newly possible fs-duration, multi-TW pulses, HHG entered an entirely new regime [36, 37]. Because of the much shorter pulse duration, the plasma surface is not destroyed by the pulse and the harmonics are cleanly emitted around the specular direction along with the reflected fundamental [38].

In the mid-nineties, there were first theoretical reports about a novel HHG mechanism based on a non-linearity of purely relativistic origin, providing a source for harmonics without the limitation of a strict cutoff at the plasma shelf density [39–42]. The mechanism could roughly be described by a simple model, now commonly termed the "relativistically oscillating mirror" (ROM) [40, 41]. However, for the time being, lasers were still not strong enough to unambiguously demonstrate the relativistic effect in distinction to the non-relativistic plasma non-linearities.

In the first decade of the new millennium, theory of surface HHG made further substantial advances. It was found, that for fs-laser systems the harmonics due to the plasma non-linearity were much stronger than could be expected from the old theory. This was attributed to so-called Brunel electrons [43] that trigger the plasma oscillations instead of the evanescent laser field, leading to "coherent wake emission" (CWE) [44]. Also, the ROM model was substantially refined by Baeva *et al.* [45], who managed to calculate a universal spectral envelope ($I \propto \omega^{-8/3}$) for the model by means of asymptotic analysis. The refined version of the ROM model takes fully into account the surface acceleration, leading to a smooth spectral cutoff at a frequency scaling as $\omega_c \propto \gamma^3$, comparable to synchrotron radiation, and not just proportional to γ^2 like the Doppler frequency upshift at a constantly moving mirror. Around the same time, experiments were first able to unambiguously demonstrate the relativistic mechanism and confirmed the spectrum obtained in the refined ROM model, see Ref. [46].

In 2010, an der Brügge and Pukhov [11] discovered another mechanism based on the relativistic non-linearity. They found out, that for certain combinations of parameters, extremely dense and narrow electron bunches may form at the surface. In this exciting regime, not even the basic boundary condition of the ROM model is valid and the frequency upconversion process can be much more efficient than predicted by the model. The radiation is then described as coherent synchrotron emission (CSE) from the electron "nanobunches".

3.1 Theory of Relativistic Surface Harmonics

We discuss the theory of HHG at surface plasmas, with a focus on the highly relativistic regime $a_0 \gg 1$.

In subsection 3.1.1, we start by summarizing the theoretical framework all models of the interaction are based on. Once having the equations written down, it is straightforward to derive some selection rules for the parity and the polarization of the generated harmonics.

In subsection 3.1.2, the ROM model is discussed. We are going to see that this reputedly well-known model still bears some surprises, with respect to both its foundation and the spectra that can be derived from it.

After this, we consider a variation of the ROM boundary condition that was suggested in Ref. [47] in conjunction with a two-pulse-scheme (subsection 3.1.3). We show, that this condition represents a "totally reflecting oscillating mirror" (TROM) with negligible skin depth and rigorously derive a spectral envelope from the model via asymptotic analysis.

Especially for p-polarized oblique incidence, the formation of highly dense and narrow electron nanobunches in front of the surface is often observed. If these bunches carry a considerable amount of charge, they emit intense high frequency radiation that is not described within the ROM model. In this case, we can derive the spectrum by calculating the coherent synchrotron emission (CSE) from these bunches - as presented in subsection 3.1.4.

3.1.1 Starting point of analysis

The foundation of the theory of surface HHG is explained here.

In Sub. 3.1.1.1, we demonstrate the Green function solution of the inhomogeneous wave equation. This solution provides a general starting point of HHG theory. Then (Sub. 3.1.1.2), we have a closer look at the source term to derive general selection rules concerning the parity and polarization of the generated harmonics. In Sub. 3.1.1.3, we briefly deal with surface HHG in the sub-relativistic regime.

3.1.1.1 Solution of the inhomogeneous wave equation

Let us begin with the classical wave equation for the electromagnetic potential. Since the basic structure of the physical mechanism can best be understood in a one dimensional slab geometry, we let $\mathbf{A}$ depend on only one spatial coordinate x and the time t. By this we do not generally exclude oblique incidence, because it can be treated in a Lorentz boosted frame wherein the laser is normally incident (see App. B.2). In this geometry, the wave equation in Coulomb gauge ($\nabla \cdot \mathbf{A} = 0$) can be written as:

$$\frac{1}{c^2}\partial_t^2 \mathbf{A}(t,x) - \partial_x^2 \mathbf{A}(t,x) = \frac{4\pi}{c}\mathbf{j}_\perp(t,x). \tag{3.1}$$

Equation (3.1) can generally be solved with the help of a Green function. We formally write down the solution as

$$\mathbf{A}(t,x) = 4\pi \iint \mathbf{j}_\perp(t',x')\, G(t,x,t',x')\, dt'dx'. \tag{3.2}$$

By the choice of G, the asymptotic behaviour of $\mathbf{A}$ can be controlled. We choose the Green function G in order to solve Eq. (3.1) and additionally fulfil the boundary condition $|\mathbf{A}(t,x)| \to 0$ for $x \to +\infty$, i.e. there is no light coming from the right and all radiation coming from the left is fully reflected. We obtain:

$$G(t,x,t',x') = \frac{1}{2}\left[\theta\left(t - t' - \frac{|x-x'|}{c}\right) - \theta\left(t - t' - \frac{x-x'}{c}\right)\right], \tag{3.3}$$

where θ denotes the Heaviside step function.

It proves convenient to continue working with the transverse electric field $\mathbf{E}_\perp = -c^{-1}\partial_t \mathbf{A}$ instead of the vector potential here. Thus Eq. (3.2) becomes:

$$\mathbf{E}_\perp(t,x) = \frac{2\pi}{c}\int_x^\infty \left[\mathbf{j}_\perp\left(t - \frac{x-x'}{c},\, x'\right) - \mathbf{j}_\perp\left(t + \frac{x-x'}{c},\, x'\right)\right] dx'. \tag{3.4}$$

Let us define $x_v \equiv \sup\{x : j(t,x') = 0,\, \forall t,\, \forall x' < x\}$: the leftmost point which is reached by any charge during the laser-plasma interaction process. It can be seen that for all $x < x_v$ to the left of the plasma, the first term in Eq. (3.4) represents the incoming radiation, while the second term represents the reflected one. To the right of the plasma both terms cancel, as our choice of the Green function requested.

Due to the assumption of one-dimensionality, the radiation does not change while propagating in vacuum[1], and the incoming and outgoing fields $\mathbf{E}_i$ and $\mathbf{E}_r$ are each function of only one variable $t \pm x/c$. We may therefore drop the argument x and identify

$$\mathbf{E}_i(t) \equiv \frac{2\pi}{c}\int_{-\infty}^{+\infty} \mathbf{j}_\perp\left(t + \frac{x'}{c},\, x'\right) dx' \tag{3.5}$$

$$\mathbf{E}_r(t) \equiv -\frac{2\pi}{c}\int_{-\infty}^{+\infty} \mathbf{j}_\perp\left(t - \frac{x'}{c},\, x'\right) dx', \tag{3.6}$$

so that $\mathbf{E}_\perp(t,\, x) = \mathbf{E}_i(t - x/c) + \mathbf{E}_r(t + x/c)$ for $x < x_v$.

Eqs. (3.5) and (3.6) provide a powerful and general starting point for the theory of harmonics generation. Whereas Eq. (3.6) tells us how to obtain the reflected field $\mathbf{E}_r$ from a given current distribution, Eq. (3.5) provides a condition on the current for a given incident field $\mathbf{E}_i$. Note that this equation stems from our choice of the Green function and physically represents the

[1] In a real experimental setting however, diffraction will play an important role; it is discussed in Sec. 3.3 of this thesis.

condition of total reflection. If instead we had chosen the Green function in a way that all fields vanish for $t \to -\infty$, then there would be no $\mathbf{E}_i$, but the generated field to the left of the plasma would be the same as $\mathbf{E}_r$ in Eq. (3.6). Equation (3.5) is of course not sufficient to explicitly calculate $\mathbf{j}_\perp$, but it can be harnessed to obtain $\mathbf{j}_\perp$ and consequently $\mathbf{E}_r$ in conjunction with some additional assumption. This is a possible approach to derive boundary conditions for the ROM and TROM models (subsections 3.1.2 and 3.1.3).

3.1.1.2 Selection Rules

Before we move on to present these models, let us collect some general facts about the source term $\mathbf{j}_\perp$, stemming from the plasma response to the laser. Therefore, we consider the fluid equations for a cold relativistic plasma. These equations do not account for kinetic effects like trajectory crossing, but they are adequate to derive some general properties of the physical process[2]. For a relatively short laser pulse, we can neglect the ion response, so the current is given by:

$$\mathbf{j} = -e\left(n\mathbf{v} - n_0\mathbf{v}_0\right), \tag{3.7}$$

where e is the elementary charge, n is the electron density and $\mathbf{v}$ is the electron fluid velocity. Note that we consider all magnitudes in the inertial frame in which the laser is normally incident. In this frame, the electrons and ions possess some initial velocity $\mathbf{v}_0$ parallel to the surface, and the initial density n_0 is not necessarily identical to the initial density in the laboratory frame. The velocity $\mathbf{v}$ is related to the relativistic momentum $\mathbf{p}$ like $\mathbf{v} = \mathbf{p}/\gamma m_e$, where $\gamma \equiv \sqrt{1 + (\mathbf{p}/m_e c)^2}$. Due to the conservation of the canonical momentum[3], the transverse component can directly be connected to $\mathbf{A}$ in the presumed 1D geometry:

$$\mathbf{p}_\perp = \mathbf{p}_0 + e\mathbf{A}. \tag{3.8}$$

The set of equations is completed by the equation of motion for the longitudinal momentum component p_x, the continuity equation and the Poisson equation for the electrostatic potential due to charge separation:

$$\frac{dp_x}{dt} = e\left(\partial_x\Phi - \frac{\mathbf{v}_\perp}{c}\cdot\mathbf{A}\right), \tag{3.9}$$

$$\partial_t n = -\partial_x\left(nv_x\right), \tag{3.10}$$

$$\partial_x^2\Phi = 4\pi e\left(n - n_0\right), \tag{3.11}$$

wherein $d/dt = \partial_t + v_x\partial_x$ denotes the absolute time derivative.

Having a closer look at these equations, it is possible to derive some "selection rules" with respect to parity (even or odd harmonic numbers) and polarization (see also Ref. [40]).

[2] A more complete description of the plasma, practically equivalent to the Vlasov equation, is given by the PIC simulations.

incident light	odd harmonics	even harmonics
normal (linear)	same as incident	-
oblique (s)	s	p
oblique (p)	p	p

Table 3.1: Selection rules for polarization (s, p) and parity (even, odd) of harmonics at plasma surfaces depending on the polarization and the angle of the incident laser.

1. Assuming normal incidence of linearly polarized light, we take $\mathbf{p}_0 = 0$, $\mathbf{A} = A\mathbf{e}_y$. It is obvious then, that $j_z = 0$, and the polarization of the incident light is conserved. For the y-component of the source term, we obtain $j_y \propto nA/\gamma$. About the longitudinal momentum p_x, which enters both n [through v_x in Eq. (3.10)] and γ, we know that $\dot{p}_x = e\left(\partial_x \Phi + eA^2/\gamma\right)$. Thus, the longitudinal momentum is driven by the square of the laser field A^2 and therefore has the same periodicity as A^2. Consequently, it possesses only even harmonics of the laser frequency. The same holds true for n and γ, as can be seen from Eq. (3.10) and $\gamma = \sqrt{1 + eA^2 + p_x^2}$. Finally, j_y is a product of $A \sim \cos\omega_0 t$ (in zeroth order) with quantities that possess only even harmonics of the fundamental laser frequency. We conclude, that j_y and therefore A purely consist of odd harmonics of the fundamental.

2. For s-polarized oblique incidence, we may assume $\mathbf{p}_0 = p_0\mathbf{e}_z$ and initially $\mathbf{A} = A\mathbf{e}_y$. In this case, $j_y \propto nA/\gamma$ as in the normal incidence case, but additionally there is a source term in z-direction: $j_z \propto np_0/\gamma - n_0 p_0/\gamma_0$. Again, p_x, n and γ contain only even harmonics of the laser frequency. Consequently, j_y and A_y contain only odd harmonics and j_z and A_z contain only even harmonics of the fundamental.

3. For p-polarized oblique incidence, we can take $\mathbf{p}_0 = p_0\mathbf{e}_y$ and $\mathbf{A} = A\mathbf{e}_y$. We immediately see, that there is no source term in z-direction ($j_z = 0$), and $j_y \propto p_0\left(n/\gamma - n_0/\gamma_0\right) + enA/\gamma$ obviously contains both even and odd harmonics. Another interesting fact is that p_x is now also driven by a term that is linear in A. This implies, that harmonics can be observed here at lower intensities compared to s-polarized and normal incidence.

In table 3.1, the rules just derived are summarized for reference.

3.1.1.3 Sub-relativistic plasma non-linearity

This work deals with generation of harmonics due to relativistic mechanisms. These have to be distinguished from harmonics generated by sub-relativistic

plasma non-linearity. Here, we explain the sub-relativistic mechanism in brief.

It is found that for p-polarized oblique laser incidence, the threshold for harmonics generation is much lower than for s-polarized or normal incidence. This is due to plasma non-linearities, which are not of relativistic origin and only occur for p-polarized incidence. Under this condition, two effects may lead to the excitation of plasma oscillations inside the inhomogeneous plasma-gradient:

1. Resonant absorption of the laser field, see e.g. the book by Kruer [3].
2. Electron bunches that are separated from the main plasma and then re-enter, see the famous work by Brunel [43].

Due to the strong inhomogeneity of the plasma, these oscillations couple back to electromagnetic modes via sum frequency generation, leading to the emission of high harmonics. When the excitation happens by means of Brunel electrons, the mechanism is commonly referred to as "coherent wake emission" (CWE) [44]. CWE is the prevalent sub-relativistic generation process for femtosecond-scale laser pulses.

According to their generation mechanism, the sub-relativistic harmonics have a strict frequency limit, given by the plasma frequency ω_p corresponding to the maximum density [33, 35, 44]. The subsequently discussed relativistic harmonics are not subject to this limitation and can therefore easily be distinguished from the ones generated by the non-relativistic mechanism. The transition between both regimes for moderately relativistic laser pulses was discussed by Tarasevitch *et al.* in Ref. [48].

3.1.2 The relativistically oscillating mirror (ROM) model

Due to its descriptive nature, the term "relativistically oscillating mirror" (ROM) is in common use. However, its usage varies among authors and there has been no accurate and generally accepted definition so far. In the frame of this work, we define the ROM model as the model based on the boundary condition[3]

$$E_i\left(t - \frac{x_{\mathrm{ARP}}(t)}{c}\right) + E_r\left(t + \frac{x_{\mathrm{ARP}}(t)}{c}\right) = 0, \tag{3.12}$$

wherein x_{ARP} denotes the coordinate of the "apparent reflection point" (ARP). In Ref. [40], where the term "oscillating mirror" was first used in the context of relativistic laser-plasma interaction, it was applied to a model based on an oscillating step-like plasma boundary. We are going to see soon that the above boundary condition is closely related to that model. Further, the ARP

[3] This means, we refer to the same model that the work of Baeva *et al.* [45] is based on, called "refined ROM model" in the introductory part of this chapter.

is intuitively understood as a sort of *mirror*, which *oscillates* at *relativistic* velocities.

This subsection consists of three parts. At first (Sub. 3.1.2.1), we investigate the foundation of Eq. (3.12), trying to clarify, under which conditions it is applicable. Then (Sub. 3.1.2.2), we demonstrate a simple way to check the validity of the model within a simulation. Finally (Sub. 3.1.2.3), we derive some very general properties of the spectrum that follows from Eq. (3.12).

3.1.2.1 Foundation of the ARP boundary condition

Here, the applicability of the boundary condition Eq. (3.12) is analyzed. To do this, we consider two possible ways to arrive at the condition. At first, we discuss the popular approach introduced by Gordienko *et al.* [49] in 2004. However, we will see, that their derivation is based on assumptions, which are hardly ever fulfilled in a realistic setup. Then, we suggest an alternative approach[4]. This new approach connects the ARP boundary condition to the assumption of a moving step-like electron density profile. The correlation between the shape of the electron density profile and the resulting radiation can nicely be confirmed within PIC simulations.

We begin with the old approach from Ref. [45, 49]. It is based on the Taylor expansion of the current distribution with respect to time: $\mathbf{j}_\perp(t_0 + h,\, x) \approx \mathbf{j}_\perp(t_0,\, x) + h\,\partial_t\mathbf{j}_\perp(t_0,\, x) + \mathcal{O}(h^2)$. This is inserted into Eq. (3.4), expanding around $t_0 = t - t'$, using $h = (x - x')/c$. Then, the zeroth order term vanishes immediately and, neglecting the second and higher orders, what remains is:

$$\mathbf{E}_\perp \approx \frac{4\pi}{c}\int_x^\infty \frac{x - x'}{c}\partial_t\mathbf{j}_\perp(t - t',\, x')\,dx'. \tag{3.13}$$

Now, the time derivative $\partial_t\mathbf{j}_\perp$ is estimated by the current divided by the "skin layer evolution time" $\tau \equiv \min\left(\mathbf{j}_\perp/\partial_t\mathbf{j}_\perp\right)$. In this way, for $x = x_{\mathrm{surf}}$ at the plasma surface, $\mathbf{E}_\perp$ can be estimated as:

$$\mathbf{E}_\perp(x = x_{\mathrm{surf}}) \sim \frac{4\pi\delta}{c\tau}\mathbf{J}_\perp, \tag{3.14}$$

where δ refers to the skin length and $\mathbf{J}_\perp$to the instantaneous net current.

The idea of Gordienko *et al.* was now to neglect the field at the moving surface and conclude the applicability of Eq. (3.12). We see that the field at the surface becomes small compared to the incident field, when the characteristic time τ is long compared to the skin length δ, $c\tau \gg \delta$. There is however no reason to assume that this is generally the case under relativistic conditions.

[4] In Ref. [50], another way to prove a supposedly "relativistic invariant" generalization of the discussed boundary condition is argued. The proof is however not based on sound physical reasoning, and it actually only shows the trivial fact that any function can be obtained by modulating phase- *and* amplitude of any other non-vanishing function.

For a conservative estimate, assume that τ is in the order of the time it takes for the longitudinally moving electrons to traverse the skin layer. Since the electrons are moving at velocities close to the speed of light, it is immediately seen that $c\tau/\delta \sim 1$. Moreover, considering a step-like or even δ-like moving electron density profile, as it is routinely observed in PIC simulations of the interaction (consider e.g. Fig. 3.3), even the above Taylor expansion may be rendered worthless due to singularities in $\mathbf{j}_\perp$ or $\partial_t \mathbf{j}_\perp$.

Therefore, let us now consider an alternative derivation of the boundary condition (3.12), based on the model of an oscillating, step-like boundary. Our starting point is an arbitrary component of the wave equation (3.1). We adapt it to the aforementioned density profile and normal incidence. Further, we make use of the conservation of the canonical momentum (3.8) and switch to relativistically normalized units ($ct \to t$, ...) for convenience:

$$\left(\partial_x^2 - \partial_t^2\right) A = \theta\left(x - x_{\mathrm{surf}}(t)\right) \frac{\omega_p^2}{\gamma} A, \tag{3.15}$$

where ω_p is the electron plasma frequency and γ is the electron γ-factor. We make the complex ansatz:

$$A(t,x) = \begin{cases} A_i(t-x) + A_r(t+x) & (x < x_{\mathrm{surf}}(t)) \\ A_s(t + i\kappa x) & (x > x_{\mathrm{surf}}(t)) \end{cases}, \tag{3.16}$$

wherein $\kappa = \sqrt{\omega_p^2/\left(\gamma\omega_0^2\right) - 1}$ is a real number, as the plasma is overdense. To take account for the relativistic non-linearities, we allow for general functions instead of strictly assuming $A_r, A_s \propto \exp\left(i\omega_0 t\right)$. Note, that the vacuum part ($x < x_{\mathrm{surf}}$) of Eq. (3.16) is an exact solution of Eq. (3.15). The skin layer part is an exact solution for the fundamental mode, $A_s \propto \exp\left(i\omega_0 t\right)$. Considering that in many cases ($\omega^{-8/3}$ - spectrum) the biggest share of energy is still contained in the laser fundamental mode, we consider this reasonable enough within our simple model.

Now the function A as well as its first partial spatial derivative must be continuous in the point $x_{\mathrm{surf}}(t)$ at every time t. Defining $a_i(t) \equiv A_i(t - x_{\mathrm{surf}}(t))$, $a_r(t) \equiv A_r(t + x_{\mathrm{surf}}(t))$, $a_s(t) \equiv A_s(t + i\kappa x_{\mathrm{surf}}(t))$, we get:

$$a_i + a_r = a_s \tag{3.17}$$

$$\frac{1}{\dot{x}_{\mathrm{surf}} - 1}\dot{a}_i + \frac{1}{\dot{x}_{\mathrm{surf}} + 1}\dot{a}_r = \frac{1}{\dot{x}_{\mathrm{surf}} - i/\kappa}\dot{a}_s. \tag{3.18}$$

Solving for $\dot{a}_s$ yields

$$\dot{a}_s = 2\frac{\dot{x}_{\mathrm{surf}} - i/\kappa}{1 + i/\kappa} E_i(t - x_{\mathrm{surf}}(t)), \tag{3.19}$$

where $\dot{a}_i = (\dot{x}_{\mathrm{surf}} - 1)\, E_i$ was used. Inserting this back into Eq. (3.18), we obtain

$$E_r(t + x_{\mathrm{surf}}(t)) + \frac{\kappa - i}{\kappa + i} E_i(t - x_{\mathrm{surf}}(t)) = 0. \tag{3.20}$$

Since $|(\kappa - i)/(\kappa + i)| = 1$ for $\kappa \in \mathbb{R}$, it is now seen that Eq. (3.20) agrees with Eq. (3.12) except for a phase term. This phase can be included in the function $x_{\mathrm{ARP}}(t)$.

We have shown here that the ARP boundary condition (3.12) is valid under three main assumptions: a step-like electron density profile, normal incidence and the interaction is dominated by the laser fundamental. In this case, the ansatz (3.16) is reasonable. If the density inside the plasma is not exactly constant, but there is a sharp rising edge behind which comparatively weak fluctuations follow, the ansatz (3.16) might still be useful, as the precise behaviour of the field deep inside the skin layer has no strong influence on the reflection. The new calculation equips us with a rough idea of when Eq. (3.12) can be expected to be useful.

3.1.2.2 Verifying the ARP boundary condition

Equation (3.12) has a simple interpretation that allows us to verify within simulation data, whether it is fulfilled or not. For Eq. (3.12) to have any useful physical meaning, it is required that $|\dot{x}_{\mathrm{ARP}}(t)| < c$ at all time[5]. It is obvious then, that the reflected field E_r is nothing but a phase modulation of the negative of the incident one ($-E_i$). In a PIC simulation, we can easily check this by looking at the fields in the time domain. If and only if Eq. (3.12) is fulfilled, then both functions possess the same sequence of extrema and monotonic intervals.

Fig. 3.1 shows one example, where Eq. (3.12) is approximately fulfilled and another, where it is distinctly violated. The example in Fig. 3.1(a) that obeys Eq. (3.12) is obtained by normal incidence on a sharply defined plasma, therefore confirming the rough calculations presented above. The other example [Fig. 3.1(c)] was obtained under p-polarized oblique incidence. Here, extremely narrow and dense electron bunches have formed in front of the surface. We are going to discuss this case in more detail in subsection 3.1.4. Now, we continue with the case, where the ROM model works.

3.1.2.3 Analytical derivation of the spectrum

Given the validity Eq. (3.12), it is possible to calculate the general form of the spectral envelope with only a few straightforward assumptions.

[5]Otherwise, the fields are un- or overdetermined, leading to contradictions or useless tautologies. The condition $|\dot{x}_{\mathrm{ARP}}(t)| < c$ is also exploited in the subsequent calculation of the spectral envelope.

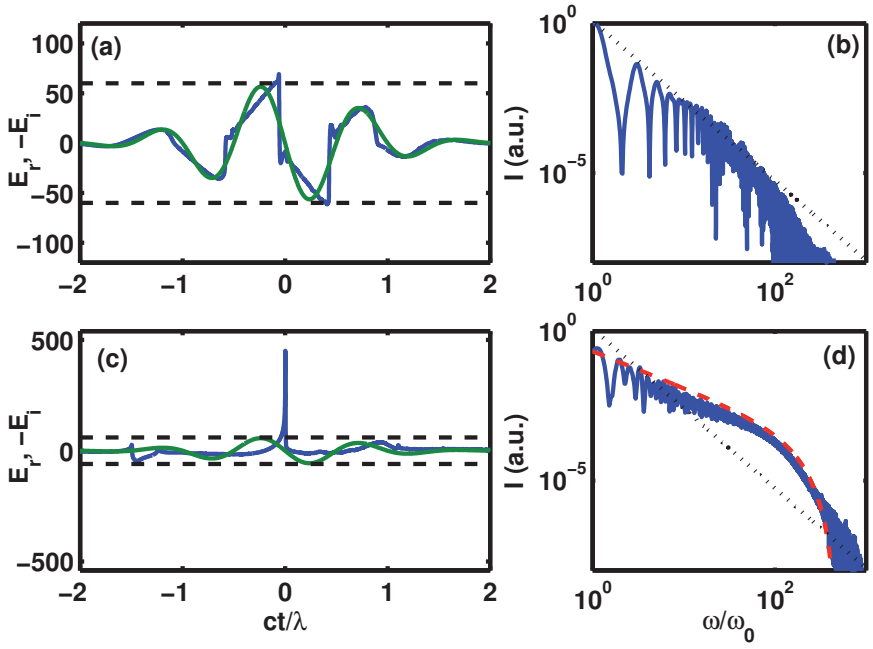

Figure 3.1: Radiation in time [(a) and (c)] and spectral [(b) and (d)] domain for two simulations. (a) and (b) correspond to a case, where Eq. (3.12) is valid. Simulation parameters are: normal incidence, plasma density $N_e = 250\,N_c$, sharp edged profile. (c) and (d) correspond to a case, where Eq. (3.12) is severely violated: plasma density ramp $\propto \exp(x/(0.33\,\lambda))$ up to a maximum density of $N_e = 95\,N_c$ (lab frame), oblique incidence at 63° angle (p-polarized). Laser field amplitude is $a_0 = 60$ in both cases. In all frames, the reflected field is represented by a blue line. In (a) and (c), the green line represents the field of the incident laser and the black dashed lines mark the maximum field of it. In (b) and (d), the dotted black line represents an 8/3 power law, the red dashed line corresponds to the "nanobunch" CSE spectrum given by Eqs. (3.35) and (3.36), with $\omega_{rs} = 800\,\omega_0$ and $\omega_{rf} = 225\,\omega_0$.

We start by writing down the Fourier transform of $E_r(t)$ from Eq. (3.12), taking into account the retarded time:

$$E_r(\omega) = -\int E_i\left(t - \frac{x_{\mathrm{ARP}}}{c}\right) e^{i\omega(t+x/c)} \left(1 + \frac{\dot{x}_{\mathrm{ARP}}}{c}\right) dt. \tag{3.21}$$

The incoming laser pulse is described by an envelope approximation $E_i(t) = g(t)\left[\exp\left(i\omega_0 t\right) + \exp\left(-i\omega_0 t\right)\right]/2$, where $g(t)$ is a slowly varying function. We arrive at

$$\begin{aligned} E_r(\omega) &= E_+ + E_- \\ E_\pm &= -\int g\left(t - \frac{x_{\mathrm{ARP}}}{c}\right) \exp\left[i\left(\omega\left(t + \frac{x_{\mathrm{ARP}}}{c}\right) \pm \omega_0\left(t - \frac{x_{\mathrm{ARP}}}{c}\right)\right)\right] \\ &\quad \times \left(1 + \frac{\dot{x}_{\mathrm{ARP}}}{c}\right) dt. \end{aligned} \tag{3.22}$$

Now note that for high ω, the exponential term leads to a rapid oscillation of the integrand during most of the time. Because of this oscillation, most contributions cancel, except for those where the phase of the integrand stands still. This means that the integral can be handled by the method of stationary phase. The somewhat more technical details of this calculation are shifted to appendix A.1, but before presenting the final result here, we would like to remark two interesting points:

1. The stationary phase points correspond to the instants when the ARP moves towards the observer with maximum velocity. These moments are crucial for the generation of high order harmonics. The corresponding ARP gamma factor $\gamma_{\mathrm{ARP}} = \left(1 - \dot{x}^2_{\mathrm{ARP}}/c^2\right)^{-1/2}$ possesses a sharp spike at these instants, which is the reason why we also call them γ-*spikes* [45].

2. The spectrum depends on the exact behaviour of the ARP in the neighbourhood of these points. In Ref. [45] it was presumed, that the derivative of the ARP acceleration is different from zero at the γ-spike. Other cases are imaginable however, and it is intriguing to see, what difference they make. Let us consider the most general case, in which $\ddot{x}_{\mathrm{ARP}}$ has a zero of order $2n-1$ at the γ-spike, meaning that $d^k x_{\mathrm{ARP}}/dt^k = 0$ for all $2 \leq k \leq 2n$. We will subsequently refer to n as the *order of the γ-spike*.

After the calculations in appendix A.1, the spectrum can now be written as:

$$I_n(\omega) \propto \omega^{-\frac{4n+4}{2n+1}} \left[\sum_{\sigma\in\{-1,1\}} \sigma\, \mathrm{gAi}_n\left(\frac{\omega\gamma^{-2} - \sigma 4\omega_0}{2\left(\alpha\omega\right)^{1/(2n+1)}}\right)\right]^2, \tag{3.23}$$

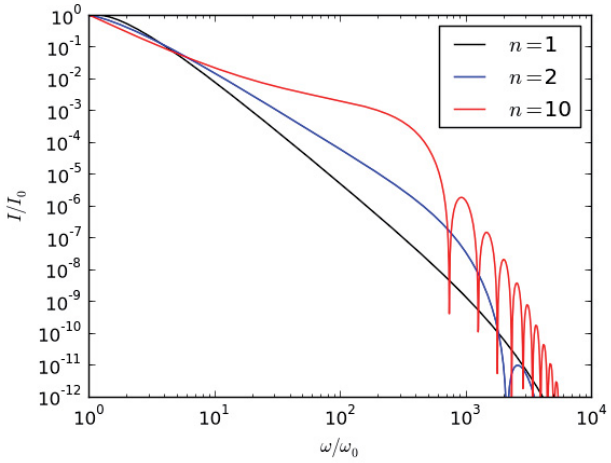

Figure 3.2: Logarithmic plot of the spectra Eq. (3.23) following from the ARP boundary condition, for orders $n = 1$, 2, 10 of the γ-spike. All spectra have been normalized to $I_0 = I(\omega_0)$, and $\alpha = 1$, $\gamma = 8$ was used throughout.

wherein γ refers to the peak value of $\gamma_{\mathrm{ARP}}(t)$. gAi_n is a generalized Airy-function in the sense $\mathrm{gAi}_n(x) \equiv (2\pi)^{-1} \int_{-\infty}^{\infty} \exp\left[i\left(xt + t^{2n+1}/(2n+1)\right)\right] dt$. These functions are not commonly available in general purpose numerical function libraries. With a small trick, they are however not hard to compute. The details of the numerical calculation of the integral are explained in appendix B.3.
Fig. 3.2 shows the spectra Eq. (3.23) for different orders n of the γ-spike. Let us regard the cases $n = 1$ and $n > 1$.
The case $n = 1$ has been investigated before by Baeva, Gordienko and Pukhov (BGP) in Ref. [45]. Here, we can apply another very good approximation to obtain the handy form:

$$I(\omega) \propto \frac{1}{\omega^{8/3}} \left[\mathrm{Ai}\left(\left(\frac{\omega}{\omega_r} \right)^{2/3} \right) \right]^2 , \tag{3.24}$$

where $\mathrm{Ai}(x)$ is the well known Airy-function, and $\omega_r/\omega_0 \sim \gamma^3$. The roll-off frequency ω_r marks the point, where the initial power law decay of the spectral envelope merges into a more rapid exponential decay. In the case $\omega \ll \omega_r$, the Airy function is $O(1)$ and one obtains the 8/3-power law spectrum. For $\omega \gg \omega_r$, the Airy function dominates and the decay becomes exponential. Note the scaling of ω_r with γ^3, which stands in contrast to the Doppler shift from the reflection at a constantly moving mirror, which produces a frequency upshift by a factor of only $4\gamma^2$. An example for this sort of spectrum from a PIC simulation can be seen in Fig. 3.1(b).

To the best of our knowledge, the case $n > 1$ has not been investigated before. We note the following differences to the BGP case ($n = 1$):

1. The power law part of the spectra decays slightly slower with increasing n. In addition, the non-power law part gains influence for increasing n at low frequencies already and leads to even slower decaying spectra. This is possibly favourable for the efficient production of attosecond pulses.

2. Because of the oscillatory behaviour of the generalized Airy functions $\mathrm{gAi}_n(x)$ at positive x and for $n > 1$, the spectra become strongly modulated at frequencies $\omega > \omega_r$, compare Fig. 3.2. This might possibly explain spectral modulations observed in numerical and real experiments before, see e.g. Ref. [51].

3. The roll-off frequency, which scales as γ^3 in the BGP case, approaches a γ^2 scaling in the limit $n \to \infty$, reminiscent of the Doppler effect from a mirror moving with constant velocity. This seems reasonable, since for higher order γ-spikes, the acceleration is very small in the neighbourhood of the stationary phase point. Therefore, its influence on the spectrum decreases with n.

To sum up this subsection, we have reviewed the popular "relativistically oscillating mirror" (ROM) model for the relativistic generation of harmonics at overdense plasma surfaces, based on Eq. (3.12). We have found, that it is applicable for normal incidence and step-like electron plasma boundaries. Because of its simplicity - it reduces the whole complex interaction physics to one simple function $x_{\mathrm{ARP}}(t)$ - the model helps us to gain insight into the basic mechanism that leads to the generation of high harmonics. Further, we have analytically calculated the possible spectra in the relativistic limit with the help of asymptotic analysis. Here we noticed, that even within the model, spectra that deviate considerably from the well known BGP 8/3-power law are in principle possible.

3.1.3 Totally reflecting oscillating mirror (TROM) and $\omega^{-2/3}$ spectrum

As we see e.g. from Fig. 3.1, the ROM model based on Eq. (3.12) as it was used in Ref. [45], is not universally valid in the highly relativistic regime - not even as an approximation. It is thus worth looking for alternatives.

This subsection is about another model that one might intuitively associate with the name "relativistically oscillating mirror", we call it the "totally reflecting oscillating mirror" (TROM). The model is rigorously based on the assumption of total reflection from a perfectly localized current layer.

First (Sub. 3.1.3.1), we derive the corresponding boundary condition. Then (Sub. 3.1.3.2), we demonstrate the spectral properties that follow from

this boundary condition, utilizing asymptotic analysis once again. Finally (Sub. 3.1.3.3) we give some remarks about the possible physical realization of the model.

3.1.3.1 Foundation of the TROM boundary condition

The TROM model is particularly interesting because of its mathematical lucidity. It can be rigorously derived from only two straightforward assumptions. These assumptions are:

1. There is total reflection, no light passes through the mirror. Therefore, we can relate the plasma current to the incident radiation via Eq. (3.5).
2. The skin layer of the reflecting plasma is infinitely thin. Therefore, the current can completely be described by $j(t,x) = \bar{j}(t)\delta(x - x_{\mathrm{TROM}}(t))$.

Inserting the current profile into Eqs. (3.5) and (3.6), we obtain:

$$E_i(t) = -2\pi \frac{\bar{j}(t - x_{\mathrm{TROM}}(t)/c)}{c + \dot{x}_{\mathrm{TROM}}(t - x_{\mathrm{TROM}}(t)/c)} \tag{3.25}$$

$$E_r(t) = 2\pi \frac{\bar{j}(t + x_{\mathrm{TROM}}(t)/c)}{c - \dot{x}_{\mathrm{TROM}}(t + x_{\mathrm{TROM}}(t)/c)}. \tag{3.26}$$

Now, the assumption of total reflection is exploited by using Eq. (3.4). We eliminate $\bar{j}$ and arrive at the boundary condition:

$$E_r\left(t + \frac{x_{\mathrm{TROM}}(t)}{c}\right) + \frac{1 - \dot{x}_{\mathrm{TROM}}/c}{1 + \dot{x}_{\mathrm{TROM}}/c} E_i\left(t - \frac{x_{\mathrm{TROM}}(t)}{c}\right) = 0. \tag{3.27}$$

Compare this to Eq. (3.12), which represents the ROM model. The difference lies in the pre-factor of E_i, which amplifies the reflected field at times, when the mirror moves towards the observer. Since these are the regions which are responsible for high frequency radiation, we expect a flatter spectrum here compared to the ROM model.

Further note, that Eq. (3.27) is always the correct boundary condition for a totally reflecting mirror in the limit of constant velocity. In this case, Eq. (3.27) could simply be derived by a Lorentz transformation to the system, where the mirror is at rest. For a strongly accelerated mirror however, we need the additional assumption of a perfectly localized skin layer to obtain Eq. (3.27).

3.1.3.2 Analytical derivation of the TROM spectrum

We now derive the spectrum corresponding to Eq. (3.27). The beginning of the calculation is analogue to the calculation in subsection 3.1.2.3, and we arrive at

$$E_{\pm} = -\int g\left(t - \frac{x_{\mathrm{TROM}}}{c}\right) \exp\left[i\left(\omega\left(t + \frac{x_{\mathrm{TROM}}}{c}\right) \pm \omega_0\left(t - \frac{x_{\mathrm{TROM}}}{c}\right)\right)\right] \times \left(1 - \frac{\dot{x}_{\mathrm{TROM}}}{c}\right) dt. \quad (3.28)$$

Compare this to Eq. (3.22). The difference lies in the last factor: Whereas in Eq. (3.22) it is $1 - \dot{x}_{\mathrm{ARP}}/c$, we have $1 + \dot{x}_{\mathrm{TROM}}/c$ here. This difference is crucial, since at the stationary phase points, where $\dot{x}_{\mathrm{TROM/ARP}} \approx -c$, the term in Eq. (3.22) becomes very small, whereas the term in Eq. (3.28) even has a maximum.

Again, we can analytically calculate the corresponding spectrum, as shown in App. A.1. In general, for a γ-spike of the order n we obtain:

$$I^n_{\mathrm{TROM}}(\omega) \propto \omega^{-\frac{2}{2n+1}} \left[\sum_{\sigma\in\{-1,1\}} \sigma\, \mathrm{gAi}_n\left(\frac{\omega\gamma^{-2} - \sigma 4\omega_0}{2\,(\alpha\omega)^{1/(2n+1)}}\right)\right]^2. \quad (3.29)$$

This is the same as the ROM spectrum Eq. 3.23, except for the different exponent in the power law. The TROM spectrum is much flatter. For high order γ-spikes, the power law part even tends to ω^0, so that the spectrum is merely determined by the generalized Airy functions.

In the more likely case $n = 1$, Eq. (3.29) can to a good approximation be simplified:

$$I^1_{\mathrm{TROM}}(\omega) \propto \frac{1}{\omega^{2/3}} \left[\mathrm{Ai}\left(\left(\frac{\omega}{\omega_r}\right)^{2/3}\right)\right]^2. \quad (3.30)$$

Compared to the $\omega^{-8/3}$ decay predicted for the ROM model [Eq. (3.24)], we obtain a slowly decaying $\omega^{-2/3}$ power law here.

3.1.3.3 Physical Feasibility of the TROM model

As we have seen, the TROM model yields a distinctly flatter spectrum than the ROM one. Therefore, if there were a physical system that behaves according to the TROM model, it could be much more efficient in the production of attosecond pulses. Let us try to answer (a) why this is difficult and (b) how it might still be possible.

The difficulty can readily be seen from Eq. (3.25). We notice that the current $\bar{j}$ does not necessarily vanish at the instant when the surface moves at maximum velocity. This is in contrast to the normal behaviour of an ultra-relativistic plasma. The transverse current is the product of the transverse fluid velocity component v_y and the charge density ρ. Since the transverse

velocity component becomes very small at the instant of maximum longitudinal velocity, a finite $\bar{j}$ implies a huge plasma density. But very dense plasmas are hard to drive to relativistic motion.

For single pulse schemes, the realization is probably impossible. The behaviour of ultra-relativistic plasmas is governed by the S-parameter $S \equiv N_e/a_0 N_c$. If the S-parameter is too low, it leads to an extended skin layer in contradiction to the assumption of a perfectly localized current layer. If the S-parameter is too high, the plasma is not driven to relativistic motion at all.

In Ref. [47], Tarasevitch *et al.* propose the realization of the boundary condition (3.27) via a two pulse scheme. In the scheme, the first, relativistically strong pulse drives the plasma surface to oscillation. The second pulse is much weaker and has a polarization orthogonal to the first one. It is used as a probe and the spectrum in the direction of its polarization is recorded. Indeed, for a certain set of parameters it was possible to observe the generation of harmonics according to Eq. (3.27). Thereby, they heuristically also find a 2/3-power law spectrum, confirming the above calculations.

In this case, the probe pulse "harvests" the harmonics generated by the much stronger driver pulse. Thus, the scheme is not appropriate to increase the overall efficiency of frequency conversion or attosecond pulse production. In the following section, we will look at a physical mechanism, where the overall efficiency is indeed increased considerably in comparison to the ROM case.

3.1.4 Coherent synchrotron emission (CSE) from electron nanobunches

Cases where the ARP boundary condition (3.12) does not apply are studied here. We find, that the radiation can be described as coherent synchrotron emission (CSE) from extremely compressed electron "nanobunches" that form in front of the surface.

At first (Sub. 3.1.4.1), the generation process is investigated by close examination of PIC data. Then, the spectrum is calculated analytically (Sub. 3.1.4.2) and some intriguing properties of the radiation are derived (Sub. 3.1.4.3). Finally, we analyze the sensitivity of the process to changes in the laser-plasma parameters (Sub. 3.1.4.4).

3.1.4.1 Electron nanobunching process

Let us now have a fresh look at Fig. 3.1(c). It is evident, that the maximum of the reflected field reaches out about an order of magnitude higher than the amplitude of the incident laser. The reflected radiation can clearly *not* be obtained from the incident one by phase modulation and the ARP boundary condition Eq. (3.12) fails.

Consequently, the spectrum deviates from the 8/3-power law, compare Fig. 3.1(d). Indeed, the efficiency of harmonics generation is much higher than estimated by the calculations in Ref. [45]: about two orders of magnitude at the hundredth harmonic. Also, we can securely exclude coherent wake emission (CWE) as the responsible mechanism, since this would request a cut-off around $\omega = 10\omega_0$. The radiation has to be attributed to a new sort of mechanism.

To get a picture of the physics behind, let us have a look at the motion of the plasma electrons that generate the radiation. Figure 3.3 shows the evolution of the electron density corresponding to both sample cases from Fig. 3.1. In addition to the density, contour lines of the spectrally filtered reflected radiation are plotted. These lines illustrate where the main part of the high frequency radiation emerges.

We observe that in both cases the main part of the harmonics is generated at the point, when the electrons move towards the observer. This shows again that in both cases the radiation does not stem from CWE. For CWE harmonics, the radiation is generated inside the plasma, at the instant when the Brunel electrons re-enter the plasma [44].

Apart from that mutuality, the two presented cases are very different. Figure 3.3(a) corresponds to the ROM case. It can be seen that the density profile remains roughly step-like during the whole interaction process and the plasma skin layer radiates as a whole. This explains why the ROM model works well here, as we have seen before in Fig. 3.1(a) and (b).

Figure 3.3(b) looks clearly different. The density distribution at the moment of harmonics generation is far from being step-like, but possesses a highly dense (up to $\sim 10000\, N_c$ density) and very narrow δ-like peak, with a width of only a few nanometres. This electron "nanobunch" emits synchrotron radiation coherently.

The high frequency radiation is emitted by a highly compressed electron bunch moving *away* from the plasma. However, the electrons first become compressed by the relativistic ponderomotive force of the laser that is directed into the plasma, compare the blue lines in Fig. 3.4. During that phase, the longitudinal electric field component grows until the electrostatic force turns around the bunch, compare the green lines in Fig. 3.4. Normally, the bunch will loose its compression in that instant, but in some cases, as in the one considered here, the fields and the bunch current match in a way that the bunch maintains or even increases its compression. The final stage is depicted by the red lines in Fig. 3.4.

We emphasize, that such extreme nanobunching does not occur in every case of p-polarized oblique incidence of a highly relativistic laser on an overdense plasma surface. On the contrary, it turns out that the process is highly sensitive to changes in the plasma density profile, laser pulse amplitude, pulse duration, angle of incidence and even the carrier envelope phase of the laser. For a longer pulse, we may even observe the case, that nanobunching is

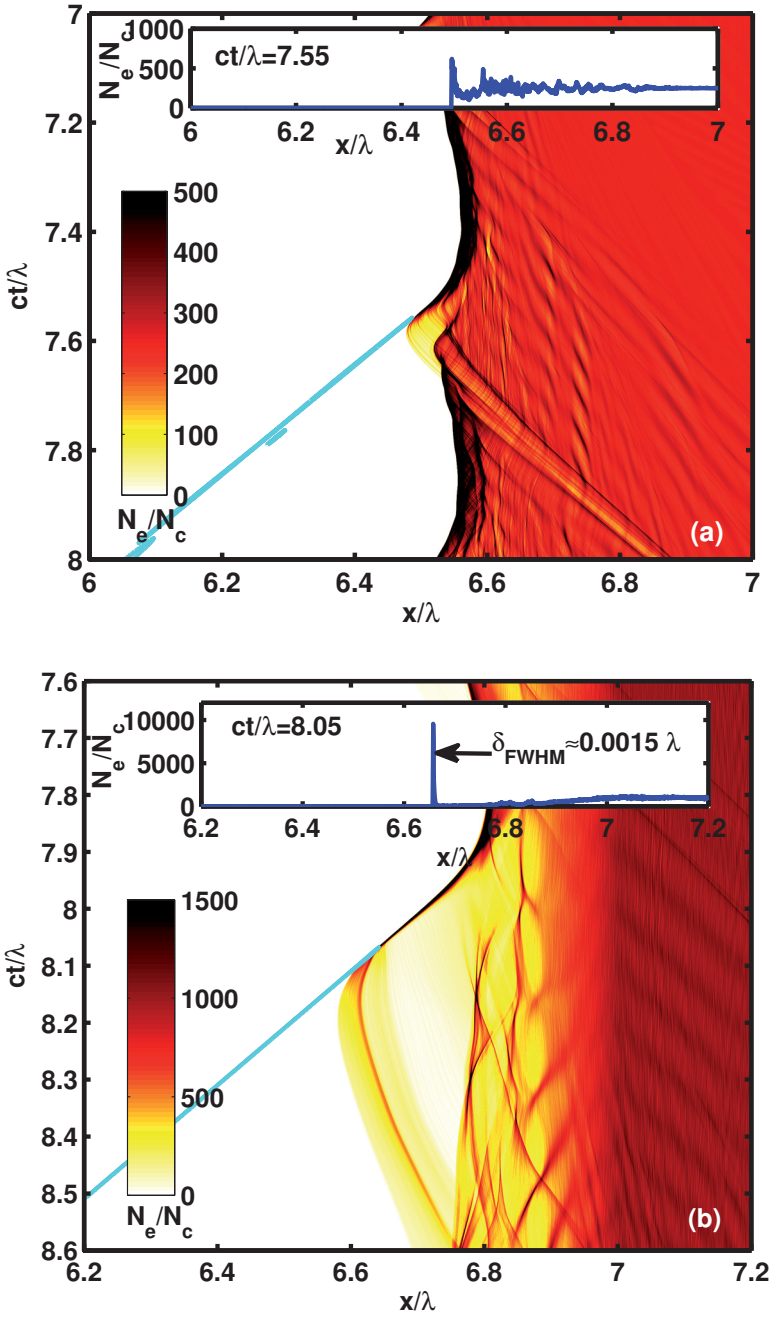

Figure 3.3: The electron density and contour lines (cyan) of the emitted harmonics radiation for $\omega/\omega_0 > 4.5$, in (a) the ROM and (b) the nanobunching regime. The small windows inside the main figures show the detailed density profile at the instant of harmonic generation. All magnitudes are taken in the simulation frame. The simulation parameters are the same as in Fig. 3.1, where (a) here corresponds to Fig. 3.1(a)-(b) and (b) to Fig. 3.1(c)-(d).

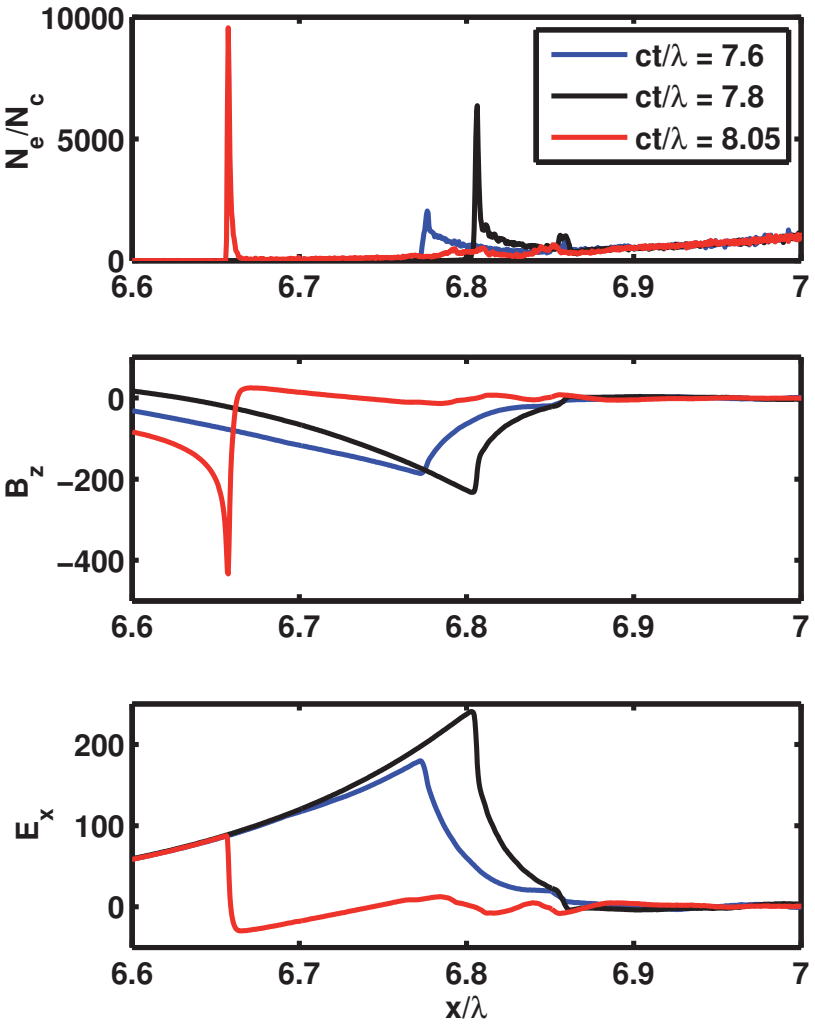

Figure 3.4: Formation of the nanobunch in the simulation corresponding to Figs. 3.1(c)-(d) and 3.3(b). We depict the electron density N_e in units of the critical density N_c, the transverse magnetic field component B_z and the longitudinal electric field component E_x in relativistically normalized units.

present in some optical cycles but not in others. The parameters in the example were selected in a way to demonstrate the new effect unambiguously, i.e. the nanobunch is well formed and emits a spectrum that clearly differs from the BGP one. The dependence of the effect on some parameters is discussed in subsection 3.1.4.4.

Because of the one dimensional slab geometry, the spectrum is not the same as the well known synchrotron spectrum [52] of a point particle. We now calculate the spectrum analytically.

3.1.4.2 Analytical derivation of the nanobunch 1D CSE spectrum

The calculation of the spectrum is based on two assumptions:

1. As in the TROM model, the radiation is generated by a narrow bunch of electrons. Optimal coherency for high frequencies will certainly be achieved, if the current layer is infinitely narrow: $j(t,x) = j(t)\delta(x - x_{el}(t))$. To include more realistic cases, we allow in our calculations for a narrow, but finite electron distribution:

$$j(t,x) = j(t)f(x - x_{el}(t)) \tag{3.31}$$

   with variable current $j(t)$ and position $x_{el}(t)$, but fixed shape $f(x)$.

2. In contrast to the TROM model, we give up on calculating $j(t)$ directly from the incident radiation by the assumption of total reflection. This means, that although we know that the bunch itself is not capable of totally reflecting the incoming radiation and consequently there are some additional currents inside the plasma, we do not care for them as their contribution to the high frequency spectrum are small compared to the contribution by the highly compressed bunch.
   However, to get some kind of result, an assumption about the functions $j(t)$ is required. Since we are dealing with the ultrarelativistic regime $a_0 \gg 1$, it is reasonable to assume that changes in the velocity components are governed by changes in the direction of motion rather than by changes in the absolute velocity, which is constantly very close to the speed of light c. We are going to see, that this assumption is enough to obtain the spectrum.

Following Eq. (3.6), the radiation field is expressed as $E_{\mathrm{CSE}}(t,x) = 2\pi c^{-1} \times \int j\left(t + (x - x')/c,\, x'\right) dx'$. We take the Fourier transform, thereby considering the retarded time, and arrive at the integral

$$\tilde{E}_{\mathrm{CSE}}(\omega) = \frac{2\pi}{c}\,\tilde{f}(\omega) \int_{-\infty}^{+\infty} j(t)\, \exp\left[-i\omega\left(t + \frac{x_{el}(t)}{c}\right)\right] dt, \tag{3.32}$$

wherein $\tilde{f}(\omega)$ denotes the Fourier transform of the shape function.

In analogy to the standard synchrotron radiation by a point particle, the integral can be solved with the method of stationary phase. Therefore, we Taylor expand the current $j(t)$ and the electron bunch coordinate $x_{el}(t)$ around the instant, where $\dot{x}_{el}$ is closest to $-c$. Due to the ultrarelativistic behaviour, the current vanishes at these instants and we write: $j(t) = \alpha_0 t^n$. After the calculations shown in appendix A.1, the result can be expressed as

$$\tilde{E}_{\mathrm{CSE}}(\omega) = \tilde{f}(\omega)\, \frac{-4\pi^2 \alpha_0 i^n}{c(\alpha_1 \omega)^{n+1/2n+1}}\, \frac{d^n \mathrm{gAi}_n(\xi)}{d\xi^n}, \tag{3.33}$$

where $\mathrm{gAi}_n(\xi)$ refers to a generalized Airy function, defined in Eq. (B.4) and $\xi = \omega^{2n/2n+1}\delta/\alpha_1^{1/(2n+1)}$.
Anyway, note that high order γ-spikes ($n \gg 1$) imply, that the nanobunch remains for a comparatively long time at low transverse currents. This appears to be unlikely here, as a static nanobunch would not stay together for long time without magnetic fields that can counteract the Coulomb explosion. Therefore, we go on to discuss only the two most likely special cases $n = 1$ and $n = 2$:

1. The current changes sign at the stationary phase point and we can Taylor expand $j(t) = \alpha_0\, t$. Consequently, $x_{el}(t) = -v_0 t + \alpha_1 t^3/3$. The spectral envelope can now be written as:

$$I(\omega) \propto |\tilde{f}(\omega)|^2\, \omega^{-4/3} \left[\mathrm{Ai}' \left(\left(\frac{\omega}{\omega_{rs}} \right)^{2/3} \right) \right]^2, \tag{3.34}$$

   where Ai′ is the Airy function derivative, $\omega_{rs} \approx 2^{3/2}\sqrt{\alpha_1}\gamma_0^3$, and $\gamma_0 = (1 - v_0^2)^{-1/2}$ is the relativistic γ-factor of the electron bunch at the instant when the bunch moves towards the observer. As in the ROM models, the spectral envelope (3.34) does not depend on all details of the electron bunch motion x_{el}, but only on its behaviour close to the stationary points, i.e. the γ-spikes.

2. In the case, when the current does not change sign at the stationary phase point, we Taylor expand $j(t) = \alpha_0 t^2$ and $x_{el}(t) = -v_0 t + \alpha_1 t^5/5$. This yields to the spectral envelope

$$I(\omega) \propto |\tilde{f}(\omega)|^2\, \omega^{-6/5} \left[\mathrm{S}'' \left(\left(\frac{\omega}{\omega_{rs}} \right)^{4/5} \right) \right]^2, \tag{3.35}$$

   with S″ being the second derivative of $\mathrm{S}(x) \equiv \mathrm{gAi}_2(x) = (2\pi)^{-1}$ $\times \int \exp\left[i\left(xt + t^5/5\right)\right] dt$, a special case of the canonical swallowtail integral [53]. For the characteristic frequency ω_{rs} we now obtain $\omega_{rs} \approx 2^{5/4}\sqrt[4]{\alpha_1}\gamma_0^{2.5}$. Because now even the derivative of $\ddot{x}_{el}$ is zero at the stationary phase point, the influence of acceleration on the spectrum decreases and the characteristic frequency scaling is closer to the γ^2-scaling for a mirror moving with constant velocity.

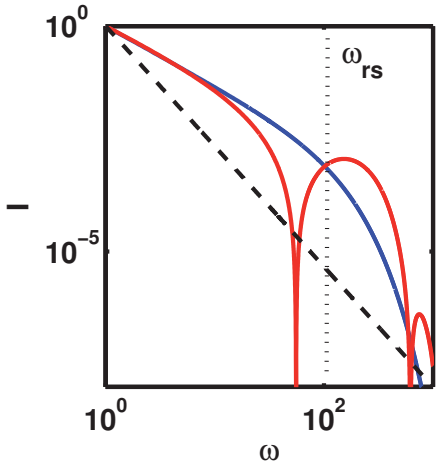

Figure 3.5: Coherent 1D synchrotron spectra for an infinitely thin electron layer $\tilde{f}(\omega) \equiv 1$ and $\omega_{rs} = 100$. The blue line corresponds to Eq. (3.34) and the red line to Eq. (3.35). For comparison, the dashed black line denotes the BGP 8/3-power law.

In Fig. 3.5 the CSE spectra of the synchrotron radiation from the electron sheets are depicted. Comparing them to the 8/3-power law from the BGP-case, we notice that, because of the smaller exponents of their power law part, the CSE spectra are much flatter. E.g., around the 100th harmonic we win more than two orders of magnitude. Note that, as in the case of higher order γ-spikes in the ROM model, side maxima are found in the spectrum (3.35). This might provide an explanation for modulations that are occasionally observed in harmonics spectra, compare Ref. [51, 54].

To compare the analytically obtained spectrum with the PIC result, the finite size of the electron bunch must be taken into account. We assume a Gaussian density profile which leads us to

$$|\tilde{f}(\omega)|^2 = \exp\left[-\left(\frac{\omega}{\omega_{rf}}\right)^2\right]. \tag{3.36}$$

Thus the spectral cut-off is determined either by ω_{rs}, corresponding to the relativistic γ-factor of the electrons, or by ω_{rf} corresponding to the bunch width. A look at the motion of the electron nanobunch in the PIC simulation (Fig. 3.6) tells us that there is no change in sign of the transverse velocity at the stationary phase point, consequently we use Eq. (3.35). We choose $\omega_{rf} = 225\,\omega_0$ and $\omega_{rs} = 800\,\omega_0$ to fit the PIC spectrum, corresponding to a Gaussian electron bunch $f(x) = \exp\left[-(x/\delta)^2\right]$ with a width of $\delta = 10^{-3}\lambda$ and an energy of $\gamma \sim 10$. This matches well with the measured electron bunch width $\delta_{\mathrm{FWHM}} = 0.0015\,\lambda$ [see Fig. 3.3(b)] and the laser amplitude

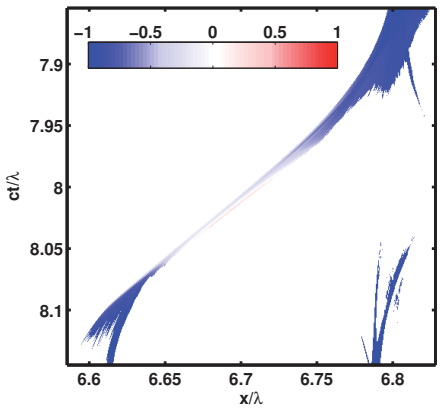

Figure 3.6: Normalized transverse fluid velocity v_y/c of the electron nanobunch. Parts of the plasma with a density below $500\,N_c$ are filtered out.

$a_0 = 60$, since we expect γ to be smaller but in the same order of magnitude as a_0. In this case $\omega_{rf} < \omega_{rs}$, so the cut-off is dominated by the finite bunch width. Still, both values are in the same order of magnitude, so that the factor coming from the Swallowtail-function cannot be neglected and actually contributes to the shape of the cut-off. The modulations that appear in Fig. 3.5 for frequencies around ω_{rs} and above cannot be seen in the spectra, because it is suppressed by the Gauss-function Eq. (3.36). The analytical synchrotron spectrum agrees excellently with the PIC result, as the reader may verify in Fig. 3.1(d).

3.1.4.3 CSE Radiation Properties

As we see in Fig. 3.1(c), the CSE radiation is emitted in the form of a single attosecond pulse whose amplitude is significantly higher than that of the incident pulse. This pulse has a FWHM duration of 0.003 laser periods, i.e. 9 as for a laser wavelength of 800 nm. This is very different from emission of the ROM harmonics, which need to undergo diffraction (see also Sec. 3.3) or spectral filtering [45] before they take on the shape of attosecond pulses.

When we apply a spectral filter in a frequency range $(\omega_{\mathrm{low}}, \omega_{\mathrm{high}})$ to a power-law harmonic spectrum with an exponent q, so that $I(\omega) = I_0(\omega_0/\omega)^q$, the energy efficiency of the resulting attosecond pulse generation process is

$$\begin{aligned} \eta_{\mathrm{atto}} &= \int_{\omega_{\mathrm{low}}}^{\omega_{\mathrm{high}}} I(\omega)\, d\omega \\ &= \frac{I_0\omega_0}{q-1}\left[\left(\frac{\omega_0}{\omega_{\mathrm{low}}}\right)^{q-1} - \left(\frac{\omega_0}{\omega_{\mathrm{high}}}\right)^{q-1}\right] \end{aligned} \tag{3.37}$$

The scaling (3.37) gives $\eta_{\rm atto}^{\rm ROM} \sim (\omega_0/\omega_{\rm low})^{5/3}$ for the BGP spectrum with $q = 8/3$. For unfiltered CSE harmonics with the spectrum $q = 4/3$ the efficiency is close to $\eta_{\rm atto}^{\rm CSE} = 1$. This means that almost the whole energy of the original optical cycle is concentrated in the attosecond pulse. Note that absorption is very small in the PIC simulations shown; it amounts to 5% in the run corresponding to Fig. 3.1(c)-(d) and is even less in the run corresponding to Fig. 3.1(a)-(b).

The ROM harmonics can be considered as a perturbation in the reflected signal as most of the pulse energy remains in the fundamental. On the contrary, the CSE harmonics consume most of the laser pulse energy. This is nicely seen in the spectral intensity of the reflected fundamental for the both cases [compare Fig. 3.1(b) and (d)]. As the absorption is negligible, the energy losses at the fundamental frequency can be explained solely by the energy transfer to high harmonics. We can roughly estimate this effect by $I_0^{BGP}/I_0^{CSE} \approx \int_1^\infty \omega^{-8/3}\,d\omega / \int_1^\infty \omega^{-4/3}\,d\omega = 5$. This value is quite close to the one from the PIC simulations: $I_0^{(\text{Fig. 1b})}/I_0^{(\text{Fig. 1d})} = 3.7$.

Further, we can estimate amplitude of the CSE attosecond pulse analytically from the spectrum. Since the harmonic phases are locked, for an arbitrary power law spectrum $I(\omega) \propto \omega^{-q}$ and a spectral filter $(\omega_{\rm low}, \omega_{\rm high})$ we integrate the amplitude spectrum and obtain:

$$E_{\rm atto} \approx \frac{2\sqrt{I|_{\omega=\omega_1}}}{q-2}\left[\left(\frac{\omega_0}{\omega_{\rm low}}\right)^{\frac{q}{2}-1} - \left(\frac{\omega_0}{\omega_{\rm high}}\right)^{\frac{q}{2}-1}\right] \tag{3.38}$$

Apparently, when the harmonic spectrum is steep, i.e. $q > 2$, the radiation is dominated by the lower harmonics $\omega_{\rm low}$. This is the case of the BGP spectrum $q = 8/3$. That is why one needs a spectral filter to extract the attosecond pulses here. The situation changes drastically for slowly decaying spectra with $q < 2$ like the CSE spectrum with $q = 4/3$. In this case, the radiation is dominated by the high harmonics $\omega_{\rm high}$. Even without any spectral filtering the radiation takes on the shape of an attosecond pulse. As a rule of thumb formula for the attosecond peak field of the unfiltered CSE radiation we can write:

$$E_{\rm atto}^{\rm CSE} \approx \sqrt{3}\left(m_c^{1/3} - 1\right) E_0 \tag{3.39}$$

Using $m_c = \omega_c/\omega_0 = 225$, the lower of the two cut-off harmonic numbers used for comparison with the PIC spectrum in Fig. 3.1d, we obtain $E_{\rm peak} = 8.8\,E_0$. This is in nice agreement with Fig. 3.1c.

3.1.4.4 Sensitivity of the nanobunching process to parametric changes

Now, we have a look at the dependence of the harmonics radiation in and close to the nanobunching regime on the laser and plasma parameters. Ex-

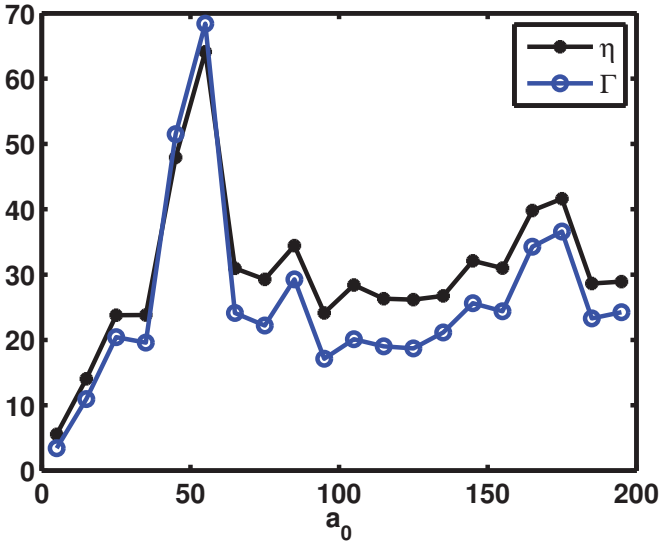

Figure 3.7: Dependence of the intensity boost $\eta = \max(E_r^2)/\max(E_i^2)$ and the pulse compression $\Gamma = (\omega_0\tau)^{-1}$, where τ is the FWHM width of the attosecond intensity peak in the reflected radiation, on a_0. The laser amplitude a_0 is varied between 5 and 195 in steps of 10. Other parameters are the same as in Fig. 3.3b.

emplary, the laser intensity and the pre-plasma scale length are varied here. The pulse duration however will be left constantly short, so that we can simply focus our interest on the main optical cycle. For longer pulses, the extent of nanobunching may vary from one optical cycle to another, which makes a parametric study more difficult. We are going to examine two dimensionless key quantities: the intensity boost $\eta \equiv \max(E_r^2)/\max(E_i^2)$ and the pulse compression $\Gamma \equiv (\omega_0\tau)^{-1}$. It is straightforward to extract both magnitudes from the PIC data, and both are quite telling. The intensity boost η is a sign of the mechanism of harmonics generation. If the ARP boundary condition Eq. (3.12) is approximately valid, we must of course have $\eta \approx 1$. Then again, if the radiation is generated by nanobunches, we expect to see strongly pronounced attosecond peaks [see Eq. (3.39)] in the reflected radiation and therefore $\eta \gg 1$. The pulse compression Γ is defined as the inverse of the attosecond pulse duration. In the nanobunching regime, we expect it to be roughly proportional to η, as the total efficiency of the attosecond pulse generation remains $\eta_{\text{atto}} \lesssim 1$, compare Eq. (3.37). In the BGP regime, there are no attosecond pulses observed without spectral filtering. So the FWHM of the intensity peak is on the order of a quarter laser period, and we expect $\Gamma \sim 1$.

In figure 3.7 the two parameters η and Γ are shown in dependence of

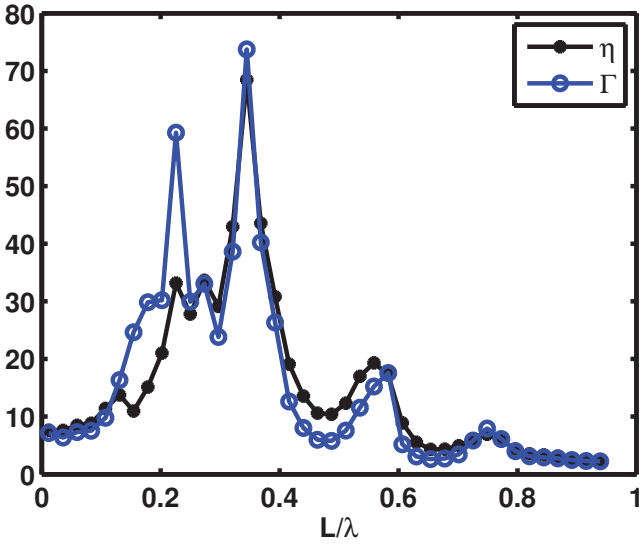

Figure 3.8: Dependence of the intensity boost $\eta = \max(E_r^2)/\max(E_i^2)$ and the pulse compression $\Gamma = (\omega_0\tau)^{-1}$, on the plasma scale length in units of the laser wavelength L/λ in the lab frame. Except for the plasma scale length, parameters are the same as in Fig. 3.3b. The plasma ramp is again an exponential one $\propto \exp(x/L)$.

a_0. Except for the variation of a_0, the parameters chosen are the same as in Figs. 3.1(c)-(d), 3.3(b) and 3.6.

First of all we notice, that for all simulations in this series with $a_0 \gg 1$, we find $\eta \gg 1$. Thus, Eq. (3.12) is violated in all cases. Since we also notice $\Gamma \gg 1$ and $\Gamma \sim \eta$, we know, that the radiation is emitted in the shape of attosecond peaks with an efficiency of the order 1. This indicates, that we can describe the radiation as CSE. The perhaps most intriguing feature of Fig. 3.7 is the strongly pronounced peak of both curves around $a_0 = 55$. We think that because of some very special phase matching between the turning point of the electron bunch and of the electromagnetic wave, the electron bunch experiences an unusually high compression at this parameter settings. This is the case that was introduced in subsection 3.1.4.1.

Figure 3.8 shows the two parameters η and Γ as functions of the plasma gradient scale length L. It is seen that both functions possess several local maxima. Further, η and Γ behave similar apart from one runaway value at $L = 0.225\lambda$, where the FWHM peak duration is extremely short, but the intensity boost is not as high. A look at the actual field data tells us that in this case the pedestal of the attosecond peak is broader, consuming most of the energy. This deviation might e.g. be caused by a different, non-Gaussian shape of the electron nanobunch.

The maximum of both functions lies around $L = 0.33\lambda$, the parameter setting analyzed in detail before. In the limit of extremely small scale lengths $L \lesssim 0.1\lambda$, η and Γ become smaller, but they remain clearly bigger than one. Thus the reflection in this parameter range can still not very well be described by the ARP boundary condition. For longer scale lengths $L > 0.8\lambda$, both key values approach 1, so the ARP boundary condition can be applied here. This is a possible explanation for why the BGP spectrum (3.24) could experimentally measured at oblique incidence [46].

3.2 Fine Structure in Relativistic Harmonics Spectra

In section 3.1, theoretical models of surface HHG were discussed. From these models we were able to compute the envelope of the harmonic spectrum, but they do not tell anything about the fine structure of the individual harmonic lines. The fine structure provides additional details about the laser-plasma interaction on the femtosecond timescale and thus may serve as a useful diagnostic. However, to utilize it, a thorough understanding is needed at first. This section aims to provide this understanding.

In subsection 3.2.1, we briefly discuss the fine structure occurring in the moderately relativistic regime. In the highly relativistic regime, the spectral fine structure is closely related to the phase of individual attosecond pulses inside the generated pulse train. Therefore, we examine the dependence of this phase on laser amplitude and plasma density in subsection 3.2.2. Next, we relate this to the chirp of the relativistic harmonics (Sub. 3.2.3) and calculate its footprint in the spectral fine structure (Sub. 3.2.4), which is well accessible in experiments. Such experiments have been conducted at the ARCTURUS facility in Düsseldorf. In subsection 3.2.5, we report about how they substantiate the presented theory.

3.2.1 Spectral fine structure in the moderately relativistic regime

At moderate intensities, modulations in the spectral fine structure such as half integer harmonics are mainly caused by parametric instabilities in the underdense part of the pre-plasma.

Parametric instabilities, such as stimulated Raman scattering and the two plasmon decay in the underdense pre-plasma lead to creation of plasmons at about half the laser frequency [3]. These plasmons can then recombine with the laser or harmonics photons via sum frequency mixing, leading to side bands or spectral lines at half-integer multiples of the fundamental [55, 56]. This mechanism is prevalent for moderate intensities $a_0 \sim 1$, longer pulse durations $c\tau \gg \lambda$ and extended pre-plasmas.

Moderate broadening of the harmonic lines may also be caused by the inherent chirp of the CWE process, see Ref. [57]. This chirp arises due to the dependence of the excursion times of the Brunel electrons. For higher intensities, the excursion times are longer, thus the attosecond pulses are emitted with a longer delay. Assuming a bell shaped temporal profile of the laser pulse, this leads to a negative (blue to red) chirp.

At higher intensities $a_0 \gg 1$, the relativistic ponderomotive force of the laser sweeps away all electrons from the underdense plasma regions. Therefore, parametric instabilities play no important role anymore. Also, the CWE mechanism looses importance as the relativistic effects take over. However, for these pulses, there is again a mechanism that leads to a variation of the phase of the attosecond pulses depending on the temporal variation of the laser intensity. This can lead to heavy broadening and modulation of the harmonic lines, particularly for extremely short pulses $c\tau \gtrsim \lambda$. Let us now go on to discuss this mechanism in detail. We begin by numerically computing the dependence of the phase of the attosecond peaks on the laser intensity and other parameters.

3.2.2 Attosecond peak phase in the highly relativistic regime

This subsection is divided into the investigation of normal incidence and the investigation of s- and p-polarized oblique incidence.

3.2.2.1 Universal phase relation in normal incidence

We start by examining the case of normal incidence on a perfectly steep plasma boundary. To begin with, a suitable definition of the "phase of the attosecond pulse" is needed.

Having another look at Fig. 3.1(a), showing a quite typical case of the reflected electric field in normal incidence HHG, tells us what to do. Due to the discontinuities in the function $E_r(t)$, the time derivative possesses clearly pronounced peaks. Therefore, we define the "attosecond phase" ϕ as the position of the maximum of the time derivative of the reflected electric field $\partial_t E_r$. Later on (Sec. 3.3) we will see, that $\partial_t E_r$ also happens to play an important role in the computation of the far field. ϕ is normalized in a way, that $\phi = 0$ if there is only the Guoy phase shift in the case of simple non-relativistic reflection from an infinitely dense surface. With this definition, we measured ϕ for a huge range of densities $N = 20 \ldots 450\, N_c$ and laser amplitudes $a_0 = 0 \ldots 450$. The result is displayed in Fig. 3.9.

Very short pulses ($\tau = 2\pi/\omega$) were used, so that the surface remained intact during the interaction even for high intensities. The phase of the incoming laser pulse is chosen in a way so that $E_i = 0$ at the maximum of the envelope, thus the attosecond peak is located close to the maximum of the envelope. The attosecond phase ϕ is plotted against the inverse S-

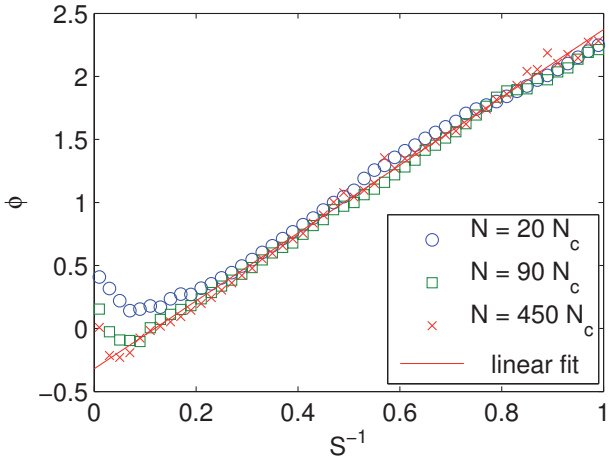

Figure 3.9: Phase dependence of the attosecond peak on the inverse S-parameter, $S^{-1} = a_0 N_c/N$, under normal incidence.

parameter (see Ref. [49]) $S^{-1} = a_0 N_c/N$. For all simulations in the highly relativistic regime $a_0 \gg 1$, we find an excellent agreement with the fit

$$\phi = 2.7\, S^{-1} - 0.32, \tag{3.40}$$

while in the low intensity limit $S^{-1} \to 0$ the phase shift tends to the value $\phi = \mathrm{acot}((N/N_c - 2)/(2\sqrt{N/N_c - 2}))$, which is expected from non-relativistic optics, approving the correctness of the PIC calculations once again.

Physically, the phase shift ϕ can be understood as a consequence of the electron surface being pushed inside the plasma by the laser. If the electron surface is pushed in to a depth of Δ, we expect the phase to experience an additional shift $\propto \Delta$. Let us devise a rough model in order to understand the linear scaling of ϕ with S^{-1}. Therefore we assume that there is a pressure balance between the ponderomotive force $f_{pond} \propto a_0^2$ of the laser and the electrostatic restoring force $f_{stat} = qE \propto N^2\Delta^2$ of the plasma. Equalizing both terms yields $\Delta \sim a_0/N$ and consequently, a linear dependence of ϕ on S^{-1}.

Note further, that in the ultrarelativistic regime the function ϕ is indeed completely independent of the absolute plasma density. This is the clearest footprint of the S-similarity [49] in laser-overdense plasma interaction observed so far.

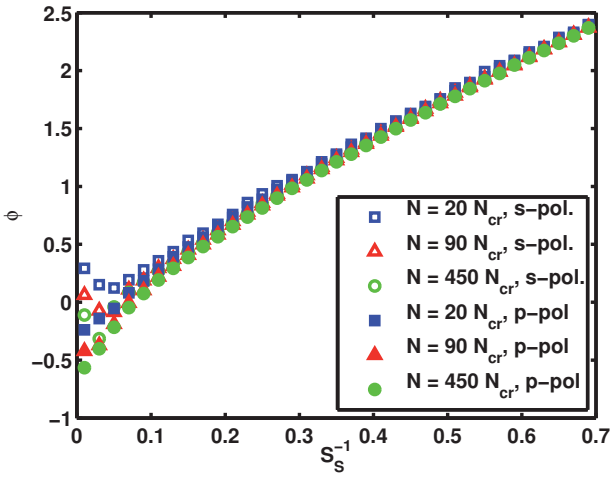

Figure 3.10: Phase dependence of the attosecond peak on the inverse S-parameter in the simulation frame, $S_S^{-1} = a_0 N_c^{(S)}/N^{(S)}$, under s-polarized oblique incidence; density N and laser amplitude a_0 are varied. In relation to the laboratory frame S-parameter, S_S scales as $S_S = S_L/\cos^3\theta$. Both the phase of s-polarized and p-polarized generated harmonics is displayed. The angle of incidence is $\theta = 45°$

3.2.2.2 Phase behaviour at oblique incidence[6]

When considering oblique incidence, the polarization is crucial. For s-polarized oblique incidence, we retain a behaviour similar to the one observed under normal incidence. For p-polarized incidence, the behaviour changes in many ways. We analyze both cases using 1D PIC simulations in a Lorentz transformed frame (see App. B.2).

Consider Fig. 3.10. As in the case of normal incidence, we confirm the dependence on the S-parameter with high accuracy in the ultrarelativistic regime. If the density is varied, but the ratio $S^{-1} = a_0 N_c/N$ is kept constant, there is no change in the attosecond phase. We also see that there is virtually no difference between the phase of the p-polarized and the s-polarized generated harmonics. This is evidence that they both are generated due to the same physical mechanism. They are not generated at separate phases as are CWE and ROM pulses in the weakly relativistic regime [44].

Further, as in the normal incidence case, an approximately linear dependence on S^{-1} is found. This can be understood, as the mechanism leading to the indention of the electron plasma surface is basically the same as for normal incidence: There is a pressure balance between the ponderomotive

[6] The results presented in this section have been obtained in cooperation with Sebastian Münster.

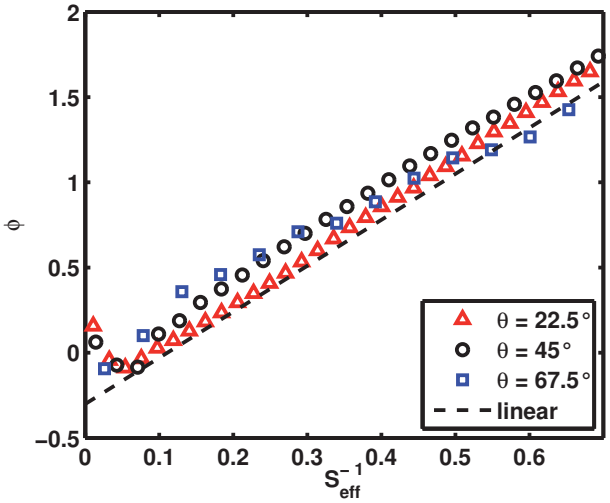

Figure 3.11: Phase dependence of the attosecond peak on the inverse effective S-parameter under s-polarized incidence, angle of incidence θ and laser amplitude a_0 varied. The effective S-parameter is defined as $S_{\text{eff}} \equiv S_L/\cos^2\theta = S_S/\gamma$ to bring out the consistent linear dependence. Here, only the phase of the s-polarized generated harmonics is displayed since the one for the p-polarized harmonics almost agrees (see Fig. 3.10).

light pressure and the electrostatic force.

In the laboratory frame however, the ponderomotive light pressure is expected to be weaker compared to normal incidence, since the laser does not hit the surface head on, but under an angle θ. Seen in the simulation frame, the ions and the electrons possess currents in opposite directions. This generates a magnetic repulsion, counteracting the electrostatic restoring force. Effectively, it leads to a mitigation of the electrostatic force by a factor of $1/\gamma$. Therefore we expect, that the scaling in s-polarized oblique incidence should remain independent of the angle θ if we consider it a function of $S_{\text{eff}} \equiv S_S/\gamma = S_L/\cos^2\theta$.

This can well be confirmed by the numerical results depicted in Fig. 3.11. We conclude, that for s-polarized incidence, the phase of both the s-polarized and the p-polarized fraction of the generated harmonics is determined *only* by the effective S-parameter $S_{\text{eff}} = a_0 N_c/(N\cos^2\theta)$ and does *not* depend on a_0, N and θ separately.

For p-polarized incidence, matters are more complex. In addition to the ponderomotive force, the surface is also pushed in and pulled out directly by the longitudinal electric field component of the laser. Numerical results are shown in Fig. 3.12.

Despite of the highly complex interaction, the attosecond phase ϕ again

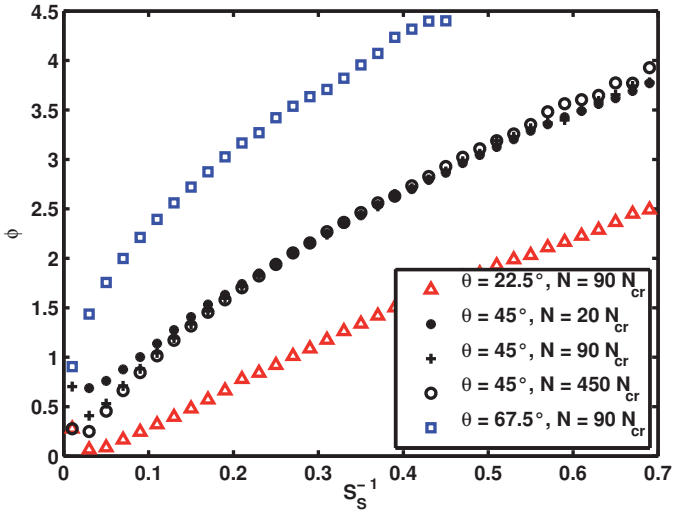

Figure 3.12: Phase dependence of the attosecond peak on the inverse S-parameter in the simulation frame under p-polarized incidence, angle of incidence θ, density N and laser amplitude a_0 are varied.

depends only on the S-parameter, not on a_0 and N separately. The slope is however not linear anymore. As we can see from Fig. 3.12, the non-linearity increases with the angle of incidence θ.

Note further that in the case of p-polarized incidence, the duration of the pulse may also play an important role. Oblique p-polarized incidence can lead to the generation of very strong quasi-static magnetic fields close to the surface. Therefore, memory effects are present and ϕ is not just a function of the instantaneous intensity but a functional of the whole history of the incident field. In section 3.2.5, we will show an example of this highly interesting effect.

3.2.3 Evidence of harmonic chirp in PIC simulation

As we have just seen, the phase of the attosecond pulses generated from overdense plasmas depends on the S-parameter of the interaction. Because of the relativistic radiation pressure of the laser pulse, the electrons are pushed inside the plasma during the rising edge of the laser pulse, causing an initial red shift of the reflected light. Later, the electron fluid will return to its original position and therefore cause a blue shift. This shifting of frequencies is called *harmonic chirp*[7].

[7]In addition to the Doppler shift due to the physical displacement of the electron surface, for an extended density gradient there is also a "virtual" Doppler shift due to the motion of the reflecting surface because of the variation in relativistic transparency, compare Ref. [56]. However, we do not intend to further distinguish these phenomena

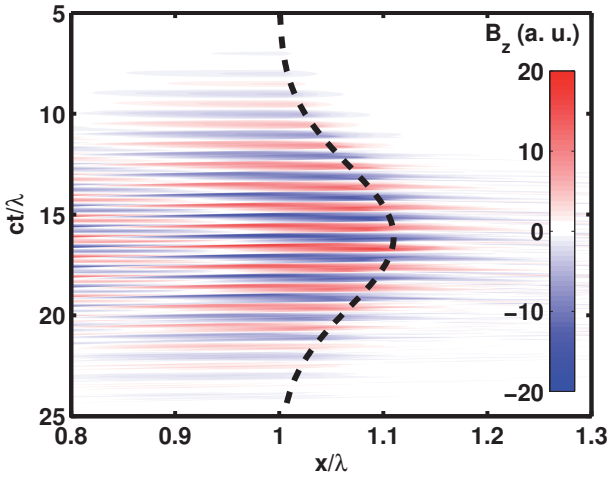

Figure 3.13: Transverse magnetic field component B_z of a laser reflecting and generating harmonics at an overdense plasma surface at normal incidence. The dashed line highlights the motion of the reflecting surface, fitted by a Gaussian function, corresponding to Eq. (3.46) with $\alpha = 1.35$. Parameters are: laser amplitude $a_0 = 10$, duration $c\tau = 5\lambda$; sharp edged plasma with density $n_e = 20\, n_c$ starting at $x = 1\,\lambda$, fixed ions.

The motion of the reflecting surface can be followed in an x-t-colourscale image of the transverse magnetic field component. Figure 3.13 shows such an image for a PIC simulation of normal laser incidence on a perfectly sharp plasma boundary. Realistic cases with oblique, p-polarized incidence on a plasma with a finite density gradient will be discussed in subsection 3.2.5. In our simple case we see that the motion of the surface is well described by a Gaussian function, i.e. the surface displacement is proportional to the instantaneous laser amplitude. This agrees with the observations made in subsection 3.2.2 with even shorter laser pulses.

As a result, the reflected radiation contains a positive chirp. This chirp can be made visible in a time-frequency image (or spectrogram). To compute the spectrogram, the time-series data from the PIC simulation is multiplied with a bell-shaped window function that is gradually moved over the data. Then, spectra of the products are calculated, yielding the spectrogram.

In Fig. 3.14 such a spectrogram is shown. The data stems from the same simulation as the previous figure. The chirp from red to blue is clearly visible in the fundamental and all harmonics shown. The higher the harmonic number, the more pronounced is the chirp. This is due to the nature of the Doppler effect. Because the relative Doppler frequency shift $\Delta\omega/\omega$ is constant, the absolute shift $\Delta\omega$ is proportional to the frequency. Further

here, since their effect on the reflected radiation is essentially the same.

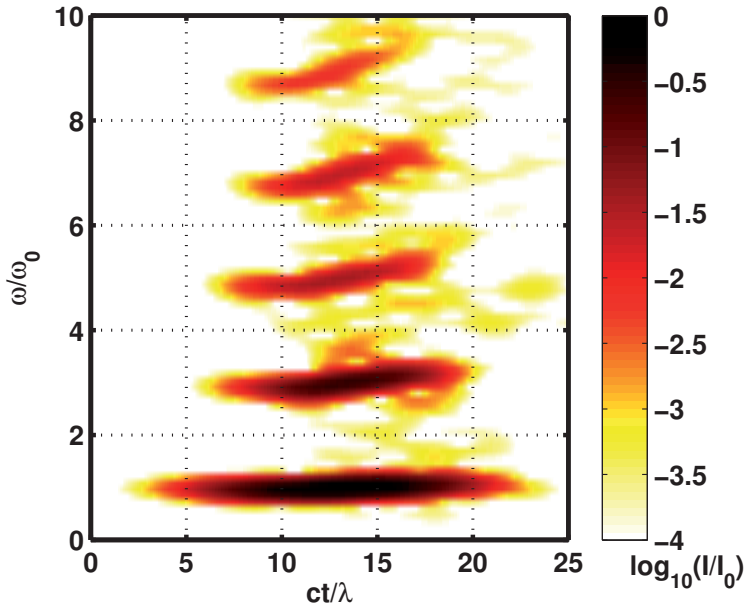

Figure 3.14: Spectrogram with logarithmic colourscale of the reflected radiation. Simulation parameters are the same as in figure 3.13. For the computation of the spectrogram, a Blackman-Harris window with a width of about eight laser periods was used.

note that the *positive* chirp (from red to blue) observed here distinguishes this relativistic regime from the CWE regime, where a *negative* chirp (from blue to red) is observed [57].

3.2.4 Spectral footprint of harmonic chirp

In the time integrated spectrum the chirp is visible in the line structure. Due to the dependence of the Doppler shift on ω, we also expect the line structure to vary according to the spectral region.

To describe this structure analytically, assume the radiation is given as a sequence of attosecond pulses emitted at the times t_k with identical shape $f(t)$ but possibly different amplitudes E_k, corresponding to the laser envelope:

$$E(t) = \sum_k E_k \, f(t - t_k). \tag{3.41}$$

Now we Fourier transform Eq. (3.41) and take the absolute square to arrive at the spectrum:

$$I(\omega) = |\tilde{f}(\omega)|^2 \underbrace{\left| \sum_k E_k e^{-i\omega t_k} \right|^2}_{J(\omega)}, \tag{3.42}$$

where $\tilde{f}(\omega)$ denotes the Fourier transformation of the attosecond pulse shape function $f(t)$. Its absolute square $|\tilde{f}(\omega)|^2$ corresponds to the spectral envelope that has been discussed in Sec. 3.1. Here, we concentrate on the second factor $J(\omega)$ that represents the spectral fine structure.

In the trivial case of equidistant pulses with constant intensities, i.e. $E_k \equiv 1$ and $t_k = kT_0 = 2\pi k/\omega_0$, the result is a sequence of sharp harmonic lines at multiples of the fundamental frequency ω_0. Such a spectrum occurs for harmonics generated by comparatively long laser pulses (picosecond range) with moderate intensities[8]. Early experiments on surface harmonics generation worked with such pulses and obtained spectra close to this prediction, compare e.g. Ref. [34].

The spectrum changes as pulses become shorter and more intense. As described above, the harmonics move from a red-shifted to a blue-shifted phase due to the Doppler effect of the averaged surface motion. To get a first impression of the effect on the spectra, let us consider two trains of pulses with a slightly different periodicity T_1 and T_2. Both pulse trains will produce a train of harmonic lines corresponding to their repetition frequencies $\omega_i = 2\pi/T_i$ ($i \in \{1, 2\}$). The harmonic lines will then interfere with each other.

[8] Note though, that in this regime the line structure may be affected by other effects, such as parametric instabilities in the underdense pre-plasma, as was explained in subsection 3.2.1.

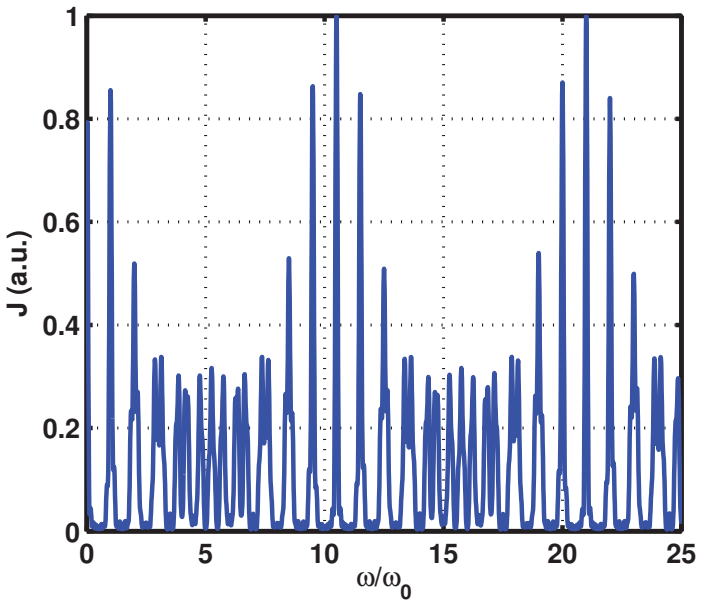

Figure 3.15: Spectral fine structure of as-pulse train with two different frequencies $\omega_1 = 0.95\,\omega_0$ and $\omega_2 = 1.05\,\omega_0$. The pulse train contains 9 pulses.

Provided they possess a finite linewidth $\delta\omega$ and the difference between the two interfering frequencies is small in the sense $\Delta \equiv \omega_2 - \omega_1 \ll \delta\omega$, we can calculate the frequency period Ω of the occurring interference pattern by setting $\Omega = n\omega_2 = (n{+}1)\omega_1$ and therefore $\Omega \approx \omega_0^2/\Delta$, where $\omega_0 = (\omega_1{+}\omega_2)/2$ is the centre frequency.

Fig. 3.15 shows the actual spectrum $J(\omega)$. The figure confirms the analytically evaluated modulation frequency of $\Omega = 10\,\omega_0$. The first few lines clearly pronounce multiples of the fundamental frequencies, then the lines become broader and at around $5\,\omega_0$, we observe two lines per harmonic. Around $10\,\omega_0$, we observe one peak per harmonic again, but this time at half integer frequencies. After that, the structure repeats, shifting back to integer harmonics around $20\,\omega_0$.

Certainly, in reality the period of the as-pulses does not change abruptly, but continuously. Let us therefore consider a linearly chirped train of attosecond pulses:

$$t_k \;=\; \frac{2\pi}{\omega_0}\left(k - \frac{\beta}{m}k^2\right), \tag{3.43}$$

where $k = -m \ldots m$. Note that the parameter β represents the maximum cycle averaged velocity acquired by the reflecting surface. Inserting (3.43)

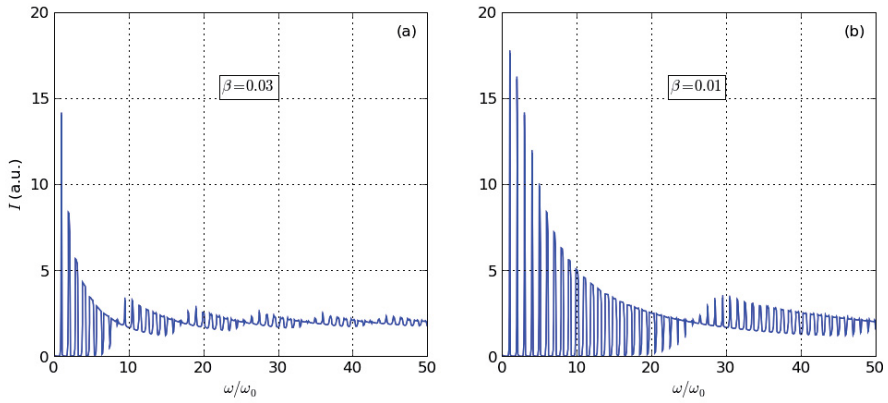

Figure 3.16: The model from Eqs. (3.42) and (3.43), using $|\tilde{f}(\omega)| \equiv 1$ and $m = 64$ throughout. Spectra are smoothed by convolution with a Gaussian function of FWHM $\Delta\omega = 0.1\,\omega_0$.

into (3.42) we arrive at

$$\sum_k E_k \exp(-i\omega t_k) = 1 + 2\sum_{k=1}^{m} \cos\left(\frac{2\pi k\omega}{\omega_0}\right) \exp\left(i\frac{2\pi k^2\omega\beta}{m\omega_0}\right). \tag{3.44}$$

The resulting spectra are depicted in Fig. 3.16. Again, we see a periodic modulation of the spectrum. Because of the continuously changing period lines also broaden, especially in the high frequency range. This leads to a decay of the modulation amplitude. Further, a quasi-continuum is observed at the spectral regions where two harmonics per period were observed with the discrete frequency model. The modulation period corresponds to the frequency difference Δ between the extreme ends of the linear chirp and therefore is proportional to the maximum surface velocity. Thus, it is possible to extract physical information from the line structure. If the reflecting surface attains a velocity of β (in units of c), we can expect large scale modulations in the line structure with a period Ω given by

$$\Omega \approx \frac{\omega_0}{4\beta}. \tag{3.45}$$

Let us now reconsider the example from the previous subsection 3.2.3. From Sec. 3.2.2 and also Fig. 3.13 of this section, we learn that the phase of the reflected radiation depends roughly linear on the laser field. Therefore, we can directly relate E_k and t_k to the envelope $g(t)$ of the laser. At normal incidence we further expect two attosecond pulses per period with alternating sign. This leads us to the model:

$$\begin{aligned} t_k &\approx \pi k/\omega_0 + \alpha\, g(\pi k/\omega_0) \\ E_k &\approx (-1)^k\, g(\pi k/\omega_0). \end{aligned} \tag{3.46}$$

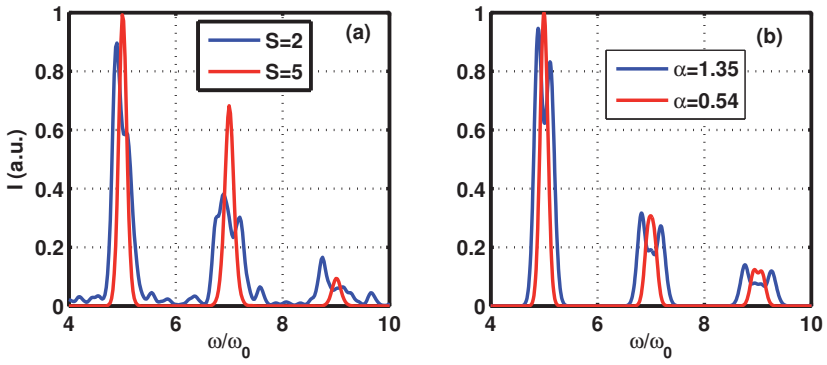

Figure 3.17: Comparison of the line structure from the fifth to the ninth harmonic (a) from PIC data and (b) due to Eqs. (3.42) and (3.46). Simulation parameters corresponding to the blue line in (a) are the same as in Figs. 3.13 and 3.14, the red line in (a) corresponds to the same set of parameters except for $n_e = 50\, n_c$.

Inserting Eqs. (3.46) into Eq. (3.42) yields the fine structure of the spectral lines. For $S \equiv n_e/a_0 n_c \gtrsim 1$, the model parameter α can be determined from the linear slope in Fig. 3.9 (or Eq. (3.40)). Therefore, $\alpha = 1.35$ corresponds to $S = 2$ and $\alpha = 0.54$ to $S = 5$.

Now we can compare the simple model to spectra obtained from PIC data. As shown in Fig. 3.17, this comparison shows good qualitative agreement. Remaining differences can arguably be attributed to the non-linear dependence of the attosecond phase and the harmonics intensity in the only moderately relativistic interaction at the edges of the pulse, which are not included in the simple model.

We conclude, that the line broadening observed in relativistic harmonics spectra can to a large extent be explained by the chirp due to unequal spacing of the attosecond pulses. It does *not* imply a loss in coherency of the individual attosecond pulses.

3.2.5 Experimental confirmation of harmonic chirp[9]

Let us now have a look at a set of parameters derived from real experiments carried out at the Düsseldorf ARCTURUS laser facility. The laser is obliquely incident under an angle of 45° and the light is p-polarized with an estimated peak amplitude of about $a_0 = 8$. Two different kinds of plasma mirrors were used to improve the laser contrast ratio: the AR[10] mirror leading to a high contrast and an extremely steep density gradient and the pol-

[9] The results presented in this section have been obtained in cooperation with colleagues from the ILPP in Düsseldorf and the IOQ at the Friedrich-Schiller University in Jena.

[10] anti-reflex coated, 0.1% reflectivity

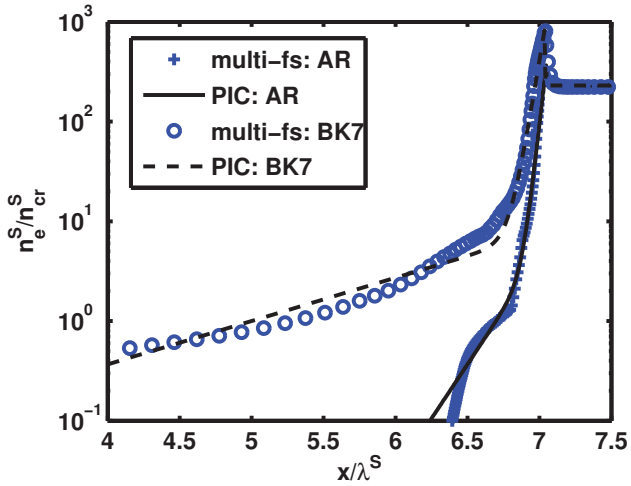

Figure 3.18: Plasma density profiles corresponding to experiments at the Arcturus laser facility using AR and BK7 type plasma mirrors. The blue crosses (AR) and circles (BK7) represent the results of the Multi-FS hydrocode calculations performed by Jens Osterholz, the black solid (AR) and dashed (BK7) lines represent the approximations by double exponential functions used in the PIC simulations. All magnitudes are shown in the Lorentz transformed simulation frame (see App. B.2).

ished BK7 glass[11] yielding a medium contrast and a little less steep density gradient. The profiles created by the laser pre-pulses were computed using the Multi-FS[32] hydrocode, the results are visualized as blue markers in Fig. 3.18. For use in PIC simulation, the hydrocode results were approximated by double exponential density profiles of the type

$$n_e(x) = \begin{cases} \exp\left[a(x-x_0)\right] + \exp\left[b(x-x_1)\right] & (x < x_2) \\ n_0 & (x > x_2) \end{cases}, \tag{3.47}$$

as indicated by the black lines in Fig. 3.18.

Figure 3.19 shows the transverse magnetic field from the interaction. Compare this to Fig. 3.13. The strong temporal asymmetry is conspicuous: Instead of instantly returning to its initial position as in the normal incidence case (Fig. 3.13), the electron surface remains indented. The static magnetic field, created by the current of the Brunel electrons, holds the electrons inside.

Because of this temporal asymmetry and the non-linear dependence of the phase on the amplitude, Eq. (3.46) ceases to apply here. To reproduce the exact spectral shape in our model would therefore require to exactly

[11] $\sim 4\%$ reflectivity

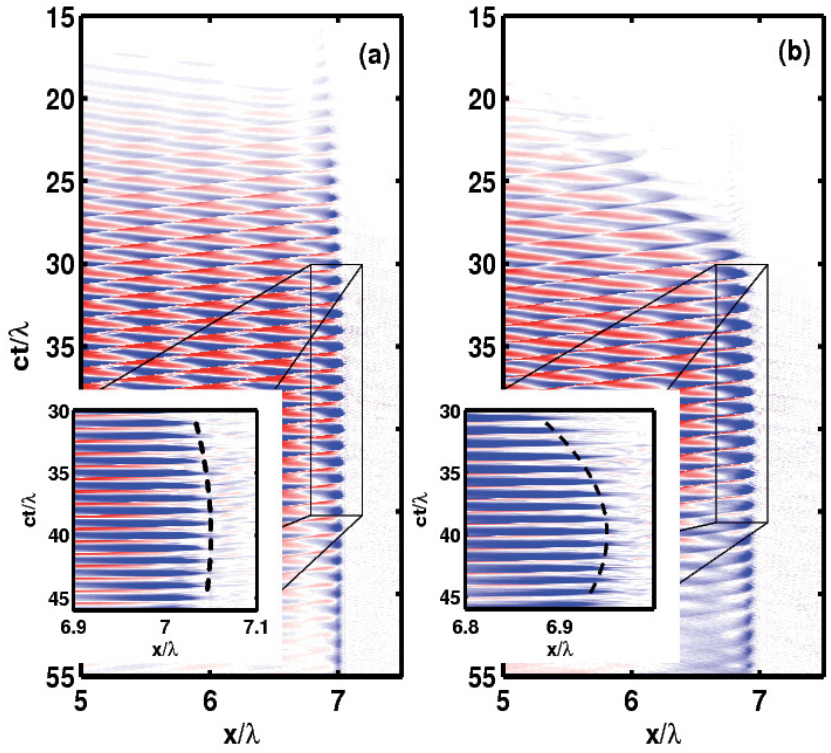

Figure 3.19: Colourscale image of the transverse magnetic field component B_z as a function of time t and space x, overview and detail. The dashed lines in the detail graphs denote the part of the surface motion used to model the spectral chirp. The data stems from simulations with a realistic set of parameters: The incident laser has a Gaussian temporal profile $a = a_0 \exp(-t^2/\tau^2)$ with amplitude $a_0 = 8.1$ and pulse duration $\tau = 10\,\lambda/c$ for both subfigures. The density profiles used are displayed in Fig. 3.18, here (a) corresponds to the AR and (b) to the BK7 plasma mirror.

trace the surface motion with a non-elementary function. The purpose of our simple model is however not to exactly reproduce the spectrum, but to extract some crucial features. Our aim is to provide clear evidence that the modulations in the experimental and PIC spectra are caused by the unequal spacing between the attosecond peaks and to show, which information can be gained from the spectra. We therefore design the model as plain as possible, leaving only two free parameters β and m. We concentrate on the main phase of harmonic generation $t = 30 \ldots 45\,\lambda/c$ and approximate the surface motion during this phase by a parabola, corresponding to a linear chirp. Also, the temporal asymmetry is ignored, taking the sum in Eq. (3.44) always from $-m$ to m.

Considering the complexity of the actual, highly non-linear process and the simplicity of the model, we observe an excellent agreement between the experimental spectra, the PIC spectra and the analytically calculated ones, compare Fig. 3.20. From the conjunction between the plasma motion in Fig. 3.19 and the model spectra from Fig. 3.20, it becomes clear that the modulations in the spectrum are caused by the unequal spacing between the attosecond pulses within the generated pulse train.

Another interesting detail is the slight redshift to be observed in experimental [Fig. 3.20(b)] and PIC [Fig. 3.20(d)] data, in particular between the 15th and the 25th harmonic. This overall redshift is a footprint of the aforementioned temporal asymmetry in the femtosecond plasma dynamic. Therefore, it witnesses the self-generated static magnetic field.

Let us now estimate the surface velocity from the experimental spectra, employing Eq. (3.45). In the "medium contrast" case, we observe a transition from integer harmonics in the region up to the 25th order to half-integer harmonics in the region beyond the 30th order. In between, the lines merge into a quasi-continuum. Thus, the modulation cycle is about $\Omega \sim 27\omega_0$, and the cycle averaged surface velocity is in the order of $0.01\,c$.

We conclude that the harmonic spectrum is rich in information about the plasma dynamics on the femtosecond timescale. In the presented experiment, the influence of the laser contrast on the pre-plasma scale is clearly reflected in the harmonics chirp and thus, in the spectral fine structure. From modulations in the spectrum, we can estimate the cycle averaged velocity of the electron plasma surface during its interaction with the main pulse.

3.3 Relativistic Harmonics in 3D Geometry

Up to now, we studied the theory of surface HHG in a simplified 1D geometry. This chapter is dedicated to the investigation of harmonics spectra and the attosecond pulses in realistic 3D geometry. There are two new groups of phenomena to be considered:

1. Due to the extremely broad spectrum of the generated radiation, dif-

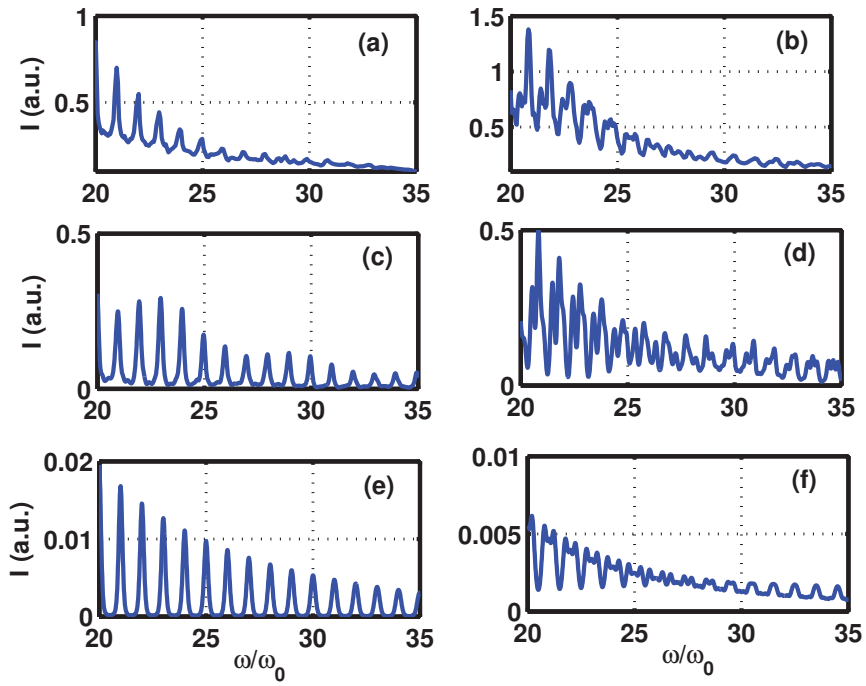

Figure 3.20: Comparison of (a)-(b) experimental, (c)-(d) PIC and (e)-(f) model spectra according to Eqs. (3.42) and (3.43). The left column represents the experiment conducted with the AR plasma mirror (high contrast, very short pre-plasma) and the corresponding simulations, the right column represents an experiment conducted with the BK7 plasma mirror (medium contrast, slightly longer pre-plasma) and the corresponding simulations. Parameters in (c) and (d) are the same as in Fig. 3.19. Parameters chosen in model: (e) $\beta = 0.0028$, (f) $\beta = 0.011$, $|\tilde{f}(\omega)| = \omega^{-8/3}$ and $m = 7$ for both. PIC and model spectra were smoothed by convolution with a Gaussian function of FWHM $\Delta\omega = 0.15\,\omega_0$ for the sake of better comparability with the spectrometer data. Intensity units within one row are comparable, but non in between the rows.

fraction will exert a major influence on the spectrum in the far field. Although the photon flux through a surface surrounding the whole solid angle of 2π in front of the plasma remains constant for each frequency, we expect the radiation field to be inhomogeneous so that the spectrum changes as a function of position. Firstly, because of the different diffraction lengths of the harmonics, and secondly, because the harmonics field distribution at the plasma surface may differ in intensity and phase from that of the driving laser. It is our main concern to investigate these phenomena since they may lead to very useful applications.

2. For very tightly focused laser pulses ($\sigma \sim \lambda$), 3D effects may play a role in the physics of the harmonics generation itself, so that 1D theory is not applicable anymore. We discuss the transition to this regime in section 3.3.4.

Two works [22, 58] precede the study of this section, which is based on the author's own work Ref. [12, 59]. The letter [58] by Gordienko *et al.* studies the coherent focusing of the surface harmonics radiation under strongly idealized conditions, and Naumova *et al.* [22] concentrate on extremely tightly focused ("λ^3-regime") pulses. Here, we present a broader overview of 3D phenomena that play a role in HHG experiments.

We begin with some analytical estimations about how the harmonics spectrum changes due to diffraction in vacuum (subsection 3.3.1). Then (subsection 3.3.2), we verify the assumption of "locally independent" HHG, to see down to which focal spot sizes 1D theory is still applicable for the generation process itself. We propose to exploit diffraction effects as "spatial spectral filters" (subsection 3.3.3) - an alternative or supplement to spectral transmission filtering to unveil the attosecond pulses in the harmonics radiation. The coherent focusing of harmonics (CHF), as proposed in Ref. [58], is a promising pathway towards extremely strong fields, perhaps reaching up to intensities that should allow us to observe exotic effects such as non-linear vacuum polarization [6, 60], predicted by quantum electrodynamics (QED). In subsection 3.3.4, we discuss it, thereby considering a more realistic setup compared to the original proposition in Ref. [58].

3.3.1 Harmonics spectrum changes due to vacuum propagation

Vacuum propagation exerts an intriguing influence on high harmonics radiation generated from solid surfaces. We start with simple analytical estimations in order to illustrate this. Further, we aim to give an idea of how these effects might be harnessed to work in our favour.

We begin by considering a linearly polarized Gaussian laser pulse normally incident onto a planar and sharp-edged overdense plasma surface. The

generated harmonic spectrum can be approximated by a power law everywhere close to the surface, so that $I_{\mathrm{near}}(r,\,\omega) \approx I_0(r)\,(\omega/\omega_0)^{-p}$ for $\omega \gg \omega_0$, where the exponent p depends on the exact HHG mechanism, e.g. $p = 8/3$ in the BGP case (see section 3.1.2.3). If we neglect the intensity dependence of absorption, $I_0(r)$ is proportional to the intensity of the incoming beam, and therefore Gaussian.

Let us at first regard the idealized case that the phase of the generated harmonics does *not* depend on r. Since the frequency ω is of course very different for distinct harmonic orders but the focal spot size σ is the same for all of them, we easily find that the beam divergence $\theta = \theta_0\omega_0/\omega$ is inversely proportional to the harmonic order. The high orders are emitted into a much smaller cone than the lower orders. On the optical axis, the spectrum in the far-field is therefore expected to show a much stronger pronunciation of high harmonic orders compared to the spectra obtained within 1D models.

Let us therefore evaluate the development of the spectrum on the optical axis. We are also interested in including the intensity-dependent frequency cut-off in our estimate, so we start with:

$$I_{\mathrm{near}}(r,\omega) = I_0(r)\,\left(\frac{\omega}{\omega_0}\right)^{-p}\,\theta\left([a(r)]^q\,\omega_c - \omega\right). \tag{3.48}$$

Here, the cut-off frequency is assumed to have a power law dependence on the vector potential amplitude $a(r)$ at a given point of the surface.

The general starting point for our computations of the far-field is the Kirchhoff formula:

$$\psi(\vec{r}') = \frac{1}{4\pi}\oint d\vec{A}\cdot\left(G(\vec{r},\vec{r}')\nabla\psi(\vec{r}') - \psi(\vec{r})\nabla G(\vec{r},\vec{r}')\right), \tag{3.49}$$

with $G(\vec{r},\vec{r}') = \exp(i\omega|\vec{r}-\vec{r}'|)/|\vec{r}-\vec{r}'|$. Specialized to the geometry of a beam focused onto a planar surface, assuming cylindrical symmetry and using $F_- = 0.5(E_y - B_z)$ this becomes

$$F_-(x,t)|_{r=0} = \frac{1}{x}\int_0^{R_{mx}} r\,dr\,\partial_t F_-\left(x=0, r, t - \frac{\sqrt{x^2+r^2}}{c}\right), \tag{3.50}$$

where $|x| \gg R_{mx} \sim \sigma$ is assumed. Equation (3.50) is specialized to planar surfaces, but the results of the following calculations may easily be reinterpreted for curved surfaces, as we are going to see in section 3.3.4.
Applying (3.50) to the harmonics generated by a Gaussian laser pulse as given by Eq. (3.48) and no phase dependence on r included, we find the far

field spectrum to be

$$I(x,\omega) = I_0 \frac{\left(\frac{\omega}{\omega_0}\right)^{-p+2}}{\left(\frac{x}{x_{Rl}}\right)^2 + \left(\frac{\omega}{\omega_0}\right)^2} \left(1 - \frac{1}{a_0}\sqrt[q]{\frac{\omega}{\omega_c}}\right)^2$$
$$\underset{x,\, a_0 \to \infty}{\approx} \frac{I_0 x_{Rl}^2}{x^2} \left(\frac{\omega}{\omega_0}\right)^{-p+2}, \tag{3.51}$$

wherein $x_{Rl} = \pi\sigma^2/\lambda$ is the Rayleigh length of the fundamental.
Eq. (3.51) shows explicitly how vacuum propagation influences the harmonics spectrum on-axis. Just by picking the right point in space in front of the harmonics-generating surface, we can find a spectrum decaying two powers slower than the spectrum predicted by 1D theory, i.e. (using the BGP exponent $p = 8/3$) $I \propto \omega^{-2/3}$. Physically, the reason for this is the much stronger collimation of the higher harmonic orders.

Another interesting detail is that the sharp spectral cut-off in the near-field yields a soft roll-off in the far-field. Provided the far field spectrum can be measured accurately, conclusions on the constants q and ω_c, which determine the general intensity dependence of the harmonics cut-off (see Eq. (3.48)) in the near-field are possible in principle.

However, the above calculation presumed that there is no phase dependence on the distance from the optical axis r in the near field. In section 3.2.2, we have seen that the attosecond phase ϕ depends on the S-parameter of the interaction. Therefore, to produce the effect explained above, it is necessary to keep the local S-parameter constant along the surface. In section 3.3.3, we discuss methods to achieve this, employing PIC simulation to substantiate our proposal.

Now let us estimate the consequences of the variation of the local S-parameter along the surface in the case of a Gaussian laser pulse, normally[12] incident on a surface with steep density gradient up to a constant density. Due to the curved phase surface, we expect the harmonics pulse to self-focus. Applying Eq. (3.40), we can calculate the curvature of the generated phase surface and consequently, the self-focusing distance x_{sf}:

$$x_{sf} = \frac{S_0}{2.7} x_{Rl}. \tag{3.52}$$

Due to this self-focusing, the divergence angle of the individual harmonics is not simply proportional to the harmonic wavelength anymore. Equation (3.40) allows us to derive an expression for the divergence angle:

$$\theta_\lambda = \theta_0 \sqrt{\left(\frac{\lambda}{\lambda_0}\right)^2 + \left(\frac{2.7}{S_0}\right)^2}, \tag{3.53}$$

[12] For s-polarized oblique incidence, the results remain valid when replacing S_0 by the effective S-parameter $S_{\text{eff}} = S_0/\cos^2\theta$.

wherein θ_0 is the solid angle, from which the laser itself is focused.

3.3.2 Checking the assumption of locally independent generation

In the above calculations we have assumed, that the generation process itself can be described by the 1D models discussed in section 3.1. Only to investigate the diffraction of the emerging radiation, we consider the real 3D geometry. In other words, we presumed that the harmonics are generated *locally independently* at each point of the surface. This means that the radial field gradient has no influence on the harmonics spectrum and phase at a certain point. There is no transverse energy transfer. Mathematically this condition can be expressed as

$$F_-(y,z,t) = F_-[F_+|_{y'=y,\,z'=z,\,t'\leq t}] \tag{3.54}$$

where F_- stands for the reflected field and F_+ for the field of the incoming radiation.

Note that this assumption also allows us to perform 1D instead of 3D PIC simulations, even if we are interested in the far-field of a realistic 3D geometry. Assuming the validity of Eq. (3.54), we can merge the results of a series of 1D simulations, utilizing Eq. (3.50) to obtain the far-field. 1D simulations are computationally much cheaper and so they can be performed with a higher resolution in the same amount of time on the same computer.

Let us now check in which parameter region the condition (3.54) is satisfied. The reflected field is of course generated by plasma electrons. The electrons are driven by the electromagnetic field of the laser pulse. In the ultra-relativistic case, the size of the electron orbits is on the order of λ. The scale length, on which the radiation intensity at the surface changes in radial direction is the beam waist σ. Therefore, if $\sigma \sim \lambda$, the electrons might mediate between regions of different intensities, endangering the validity of Eq. (3.54). If $\sigma \gg \lambda$, the electrons are not able to travel this distance and one expects that (3.54) is fulfilled.

We now compare results of 1D and 3D PIC simulations to verify this. 3D simulations were performed using the spot sizes $\sigma = 5,\, 2,\, 1,\, 0.5\,\lambda$, all with the dimensionless laser amplitude $a_0 = 30$ and the plasma density $n_e = 90\,n_c$, where $n_c = \omega_0^2 m/4\pi e^2$ is the critical density. The laser pulse is linearly polarized in y-direction. The reflected field in the 3-dimensional PIC simulations was always recorded at a distance of 1λ to the originally sharp-edged plasma surface. This field is directly compared to the result of 1D PIC simulations with the same parameters ($\delta_{1D,3D}$). Anyway, for the most tightly focused pulses the field recording distance is in the order of the fundamental Rayleigh length so that a direct comparison with 1D PIC is pointless. Instead of this, it can be compared to the far field calculated with equation (3.50) from 1D results. For $\sigma = 1\,\lambda$, the distance is already too big

Table 3.2: Deviations from the assumption of locally independent harmonic generation according to the measure (3.55).

σ/λ	$\delta_{1D,3D}$	$\delta^{\text{far}}_{1D,3D}$	$\delta_{y,z}$
5.0	0.011	0.018	0.016
2.0	0.011	0.019	0.036
1.0	-	0.036	0.115
0.5	0.196	0.092	0.240

to compare directly but yet too small to use (3.50), so the value is missing here.

Yet two more comparisons were performed. The absolute far field ($x \to \infty$) calculated by Eq. (3.50) from 1D and 3D PIC data is compared ($\delta^{\text{far}}_{1D,3D}$). This method verifies the accuracy of our quasi-1D calculations of the far-field directly.

The third comparison ($\delta_{y,z}$) concerns the radial symmetry of the reflected pulse. In the 3D geometry, it can in principle be broken because of the linear polarization of the incoming laser pulse, but it obviously cannot be broken as long as (3.54) holds. Thus this symmetry check provides another indirect criterion for verifying (3.54). The fields compared are $F_-(x = 1\lambda,\, y = \sigma\sqrt{\ln 2},\, z = 0,\, t)$ and $F_-(x = 1\lambda,\, y = 0,\, z = \sigma\sqrt{\ln 2},\, t)$, both obtained from the 3D PIC simulations.

The results of all these comparisons are collected in Tab. 3.2. The relative deviations are measured using

$$\delta_{1,2} = \frac{\int dt\, |f_1(t) - f_2(t)|^2}{\int dt\, |f_1(t)|^2 + |f_2(t)|^2} \tag{3.55}$$

This measure is 0 if $f_1$and f_2 are identical functions and 1 if they are completely uncorrelated.

It can be seen that deviations are very small for not too tiny focal spots such as $\sigma = 5\lambda$. Thus, models based on Eq. (3.54) may be used for the vast majority of today's HHG experiments. Even in the case $\sigma = \lambda$, Eq. (3.54) still holds as a rough approximation. Our studies of even tinier focal spots have shown, that the deviations from Eq. (3.54) are generally not favourable for the generation of attosecond pulses.

We now go on to discuss diffraction effects, assuming the validity of Eq. (3.54), which is correct for not too small focal spots in the sense explained above.

3.3.3 Self-focusing and spatial spectral filtering using Super-Gaussian pulses or Constant-S surfaces

In this subsection we would like to present the results of some numerical experiments. These experiments were carried out with the 1D version of the

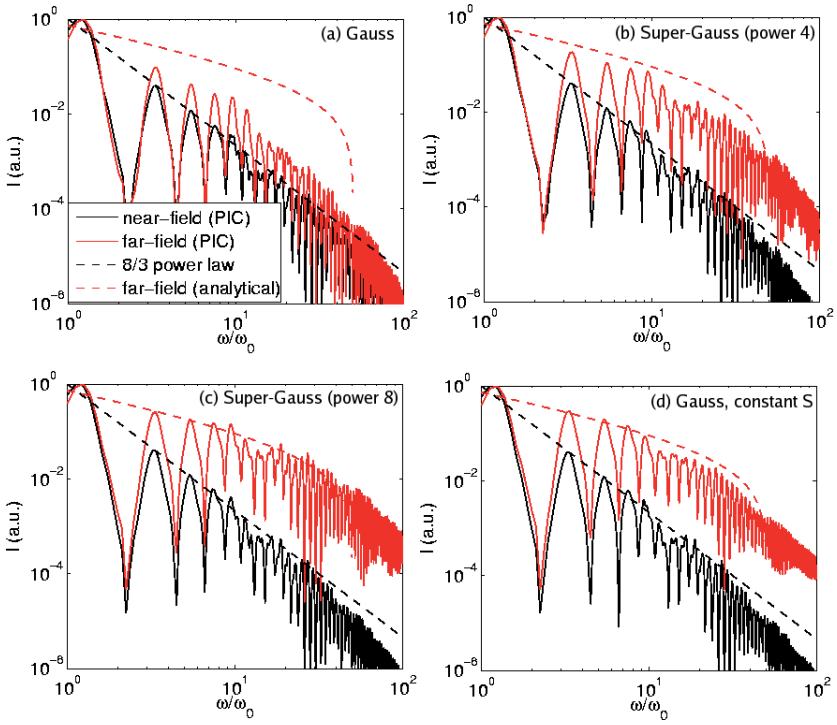

Figure 3.21: Spectra, near- and far-field ($x = \infty$) for different types of laser pulses, normalized to the intensity of the fundamental. ($a_0 = 20$)

VLPL PIC code (App. B.1) in combination with a 3D cylindrical geometry numerical propagator based on Eq. (3.50) to obtain the far-field on the optical axis from each series of 1D simulations. The simulations were made with HHG at a planar surface in mind, but in subsection 3.3.4 we are going to see that all results can easily be re-interpreted to suit HHG at a curved surface in confocal geometry. This is crucial in regard of the exciting possibilities opened up by coherent focusing of the harmonics radiation.

We start with a simulation of a Gaussian laser pulse, given by $a(x,r,t) = a_0\,\mathrm{Re}\left[\exp\left(i\,\omega_0(x/c-t)-(t/\tau)^2-(r/\sigma)^2\right)\right]$, normally incident onto a surface with a steep and constant density profile. The laser parameters are: $a_0 = 20$, $\sigma = 5\lambda$, $\tau = 2\pi/\omega_0$. The surface density is $n_e = 90\,n_c$, so that the ultra-relativistic similarity parameter [49] $S_0 = n_e/(a_0 n_c) = 4.5$ at the maximum of the laser pulse.

The resulting spectra for the near and the far-field on the optical axis in comparison to the analytical estimate (3.51) disregarding the phase variation are shown in Fig. 3.21(a). It is seen, that there is still a big difference in the slope of the spectrum compared to Eq. (3.51). Although the spectrum in the far field decays slightly slower than the spectrum close to the surface,

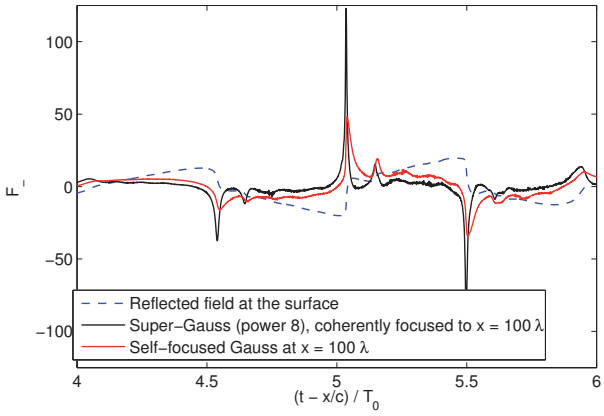

Figure 3.22: Self-focusing of a Gaussian pulse ($a_0 = 20$, $\sigma = 5\lambda$) in front of a planar surface compared to focusing of a Super-Gaussian pulse (same amplitude and power) to the same distance using a curved surface. The time unit $T_0 = 2\pi/\omega_0$ is just the laser period.

the improvement is far behind from what we could expect if the attosecond phase remained constant along the surface.

In Fig. 3.22 we see what happens at an intermediate distance from the surface. According to Eq. (3.52), the pulse should be self-focused at a distance of around $x_{sf} \approx 130\,\lambda$. Indeed, we observe that the pulse is self-focused, and the self-focusing length is in reasonable agreement with the analytical estimate. The achieved intensity is about four times the laser intensity, and it is reached at a distance of about 100λ from the surface. Even attosecond peaks can be seen, yet the contrast ratio is quite poor.

In order to improve the quality of these pulses, we should aim to keep the attosecond phase ϕ - and thus the relativistic S-parameter - constant alongside the surface. Basically, there are two possibilities to achieve this:

1. The use of laser pulses with sufficiently flat intensity distributions across the focal spot, e.g. Super-Gaussian. This causes the part of the laser pulse that contributes considerably to the HHG to be at a nearly constant intensity level.

2. Varying the surface density in a way, so that $S(r) = n_e(r)/(a(r)\,n_c) = \text{const}$.

For testing these ideas, we perform additional simulation runs: some of them using Super-Gaussian laser pulses $I \propto \exp\left[-(r/\sigma)^4\right]$ or $I \propto \exp\left[-(r/\sigma)^8\right]$ and some of them using a conventional Gaussian laser pulse, but a surface with radially varied density so that the local similarity parameter remains constant $S(r) = 4.5$. In the simulations with the Super-Gaussian laser pro-

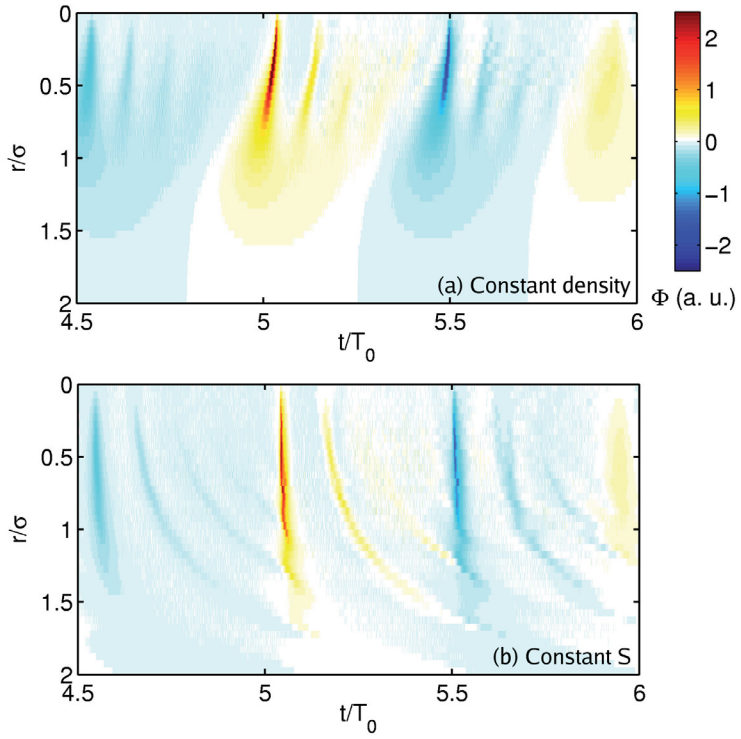

Figure 3.23: The integrand $\Phi(r,t) = r\,\partial_t F_-(x=0,r,t)$ from Eq. (3.50). The colour scale is the same for both plots. Gaussian laser pulses with $a_0 = 20$ are used.

file, σ was chosen in a way so that the laser power and amplitude are the same as in the corresponding simulations with the Gaussian pulse.

The spectra obtained from these simulations are depicted in Fig. 3.21(b)-(d). We see a great improvement compared to the unoptimized case Fig. 3.21(a). Evidently, the spectra decay much slower in the far-field, reaching close to the ideal $I \propto \omega^{-2/3}$ line that was expected from the analytical estimate in subsection 3.3.1. The lower frequencies are filtered out by diffraction in space. Therefore we may refer to these schemes as "spatial spectral filters".

The advantage of the constant-S surface can nicely be seen in Fig. 3.23, showing the integrand from which the far-field is calculated. The integration to obtain the far-field is carried out along the path $t' = t - \sqrt{x^2+r^2}/c$. Thus for the very far field in front of a planar surface, the integration path becomes a straight line. The intensity of the integral becomes maximal if the integrand is big over the whole integration path. Therefore we see, that self-focused or defocused attosecond pulses are represented by curved lines in our diagram, whereas non-self-focused attosecond pulses are represented by

straight lines. Further, longer lines lead to higher peak intensities. With this knowledge, the advantage of a constant-S surface can be easily understood from Fig. 3.23. Notice also that for the constant-S surface the side peaks are strongly defocused, yielding a better contrast ratio to the main peaks. For Super-Gaussian pulses the image would look similar to Fig. 3.23(a), except for that the upper part is stretched.

To liven up the picture of how the attosecond pulses emerge, we take a look at the on-axis field at different distances x from the surface. For Fig. 3.24 we choose a simulation with a constant-S surface, because the process of "vacuum" attosecond pulse generation is most pronounced here. While we depart from the surface together with the reflected radiation, we see how the attosecond pulses get rectified and the whole rest of the radiation is simply diffracted away from the optical axis.

Focusing these improved pulses using a confocal setting yields a much better result than the self-focusing of a Gaussian pulse in front of a planar surface as can be seen from Fig. 3.22. Here a Super-Gaussian pulse was chosen, but the use of a constant-S surface leads to a similar effect, as shown further below.

Let us now have a look at a broader range of parameters. In Fig. 3.25 the intensity and duration of the attosecond pulses in the far-field is compared for different laser amplitudes a_0 and all the proposed schemes. As shown in the following subsection 3.3.4, the results can be applied for planar surfaces as well as for focusing geometries. We compare the attosecond pulses in the far-field of a planar surface or at the focal spot in front of a spherically curved surface. We notice once again, that the Super-Gaussian laser pulse focal spots and the constant-S surfaces yield a clear advantage for the attosecond pulse generation.

In earlier works [31, 45], transmission filtering has been suggested as a technique to improve the quality of the attosecond pulses. Let us compare this to our method of spatial spectral filtering via shaping of the laser pulse focal spot.

Applying transmission filters directly to the results of 1D PIC calculations, as it has been done in previous works, yields a somewhat unrealistic picture, since the filters have to be placed inside the far-field in a real experiment. In this work we consider the 3D geometry and apply optical filters to the far-field radiation.

We compare attosecond pulses generated by lasers with a Gaussian and a Super-Gaussian focal spot, see Fig. 3.26. The first thing to notice is that filtering influences the temporal structure of the attosecond pulses. While the attosecond pulses in the unfiltered far-field are pure half-cycle pulses, optical filtering can generate single- or multi-cycle pulses, depending on the filter frequency. Then, unlike transverse pulse shaping (see Fig. 3.25), transmission filtering naturally leads to a decrease of the attosecond peak intensity. To obtain a significantly shortened pulse, one needs to use filters with a very

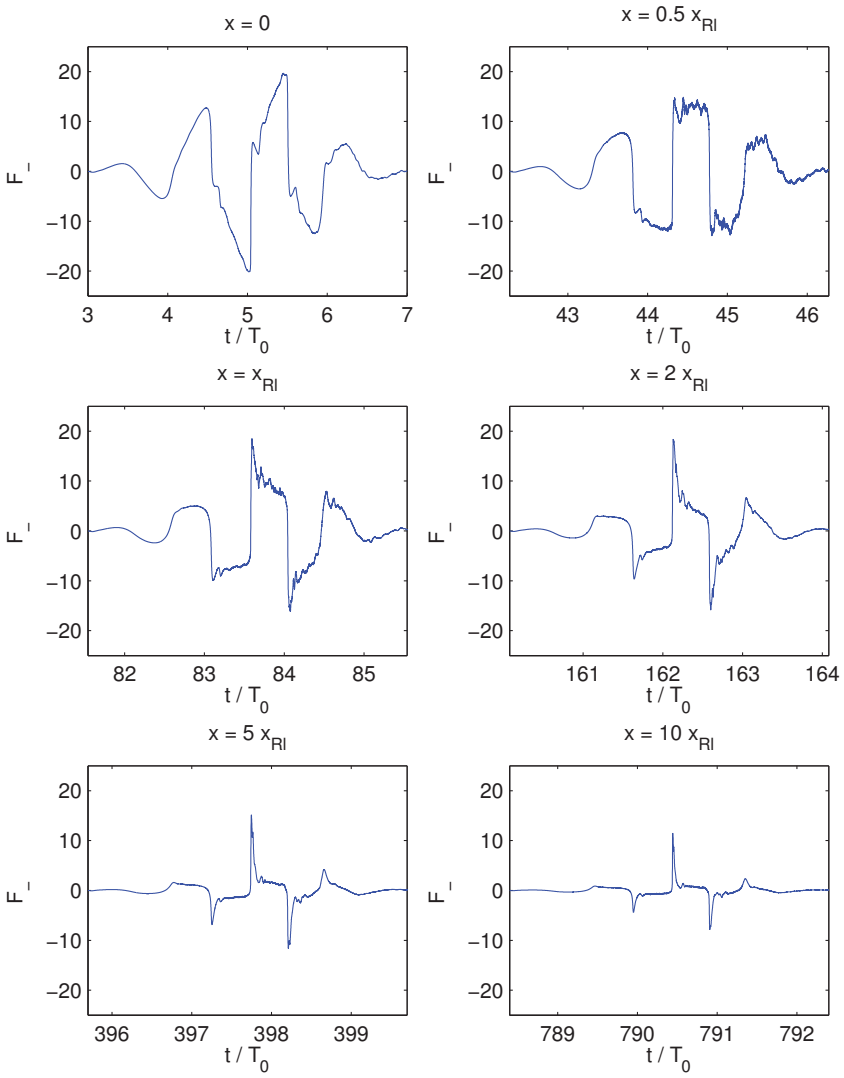

Figure 3.24: The reflected field on the optical axis, observed at different distances x from the surface. Data from PIC simulation using a Gaussian laser pulse with $a_0 = 20$ focused on a planar constant-S surface.

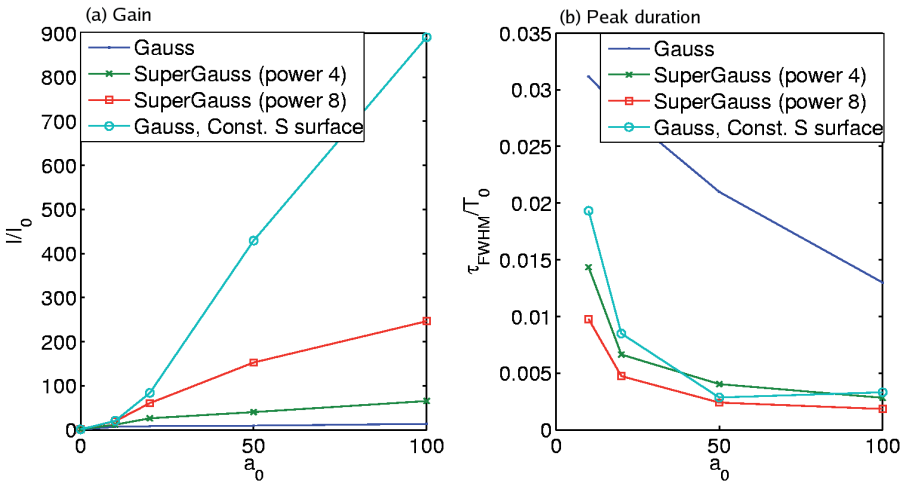

Figure 3.25: Comparison of the intensity and duration (full width half maximum) of the far-field attosecond pulses for different laser intensities, radial laser shapes and plasma surfaces. The intensity unit $I_0 = (a_0 x_{Rl}/x)^2$ is the peak intensity value we would get at the same distance from the surface for a Gaussian laser pulse with the same power and maximum vector amplitude *without* the generation of harmonics. The time unit $T_0 = 2\pi/\omega_0$ is the laser period.

high threshold frequency, eating up most of the pulse energy. Nevertheless, filtering leads to an improvement of the contrast ratio by a factor of about 3 for $\omega_{th} = 100\omega_0$.

To get the shortest possible pulse duration and the best contrast ratio, we recommend to combine transverse pulse shaping with the use of an optical filter. When attosecond pulses with a maximum peak intensity are required, the transverse pulse shaping or constant-S surfaces combined with the proper focusing geometry are the best option.

3.3.4 Optical scalings for harmonics focusing

In this subsection, we examine focusing geometries for the surface harmonics radiation. In Ref. [58] it has been shown, that coherent harmonic focusing (CHF) has the potential to produce unprecedentedly intense electromagnetic fields. The created intensities may be so extreme, that they can be used to explore exotic QED effects such as vacuum polarization or even electron-positron pair creation [6, 60]. However, the conditions under which the phenomenon was examined in Ref. [58] were strongly idealized: A perfect spherical wave, uniformly illuminating a curved plasma surface with a large solid angle of $\Omega = 1$ and a tiny radius of $R = 4\lambda$ was studied - something that is not achievable with a focused Gaussian beam. Therefore, important

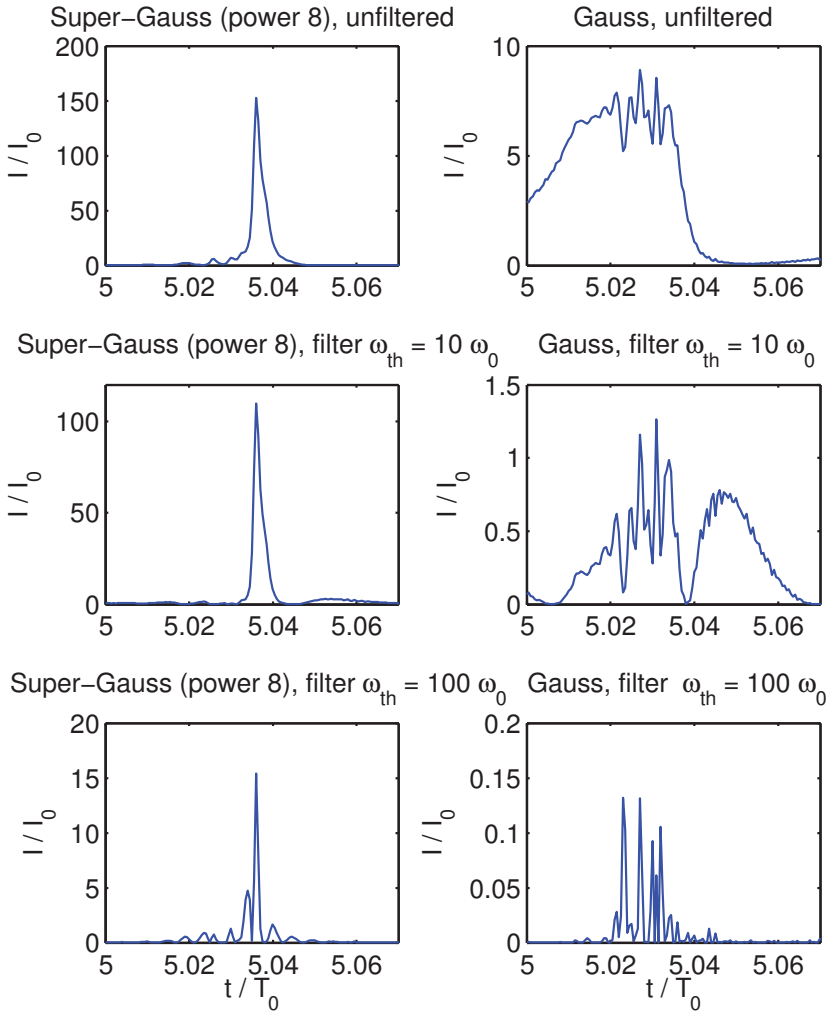

Figure 3.26: The temporal structure of the attosecond pulses in the far-field of a Supergaussian (left column) and a Gaussian (right column) laser-pulse, both with the same power and peak amplitude $a_0 = 50$ in the focus. The intensity is normalized so that the maximum in case of no harmonics and no absorption for the Gaussian Laser would be at $I/I_0 = 1$. In the second and third lines high-pass filters are applied. The filter function is a simple step like function with a linear transition of the width $\delta = \omega_0$, the threshold frequency is ω_{th}.

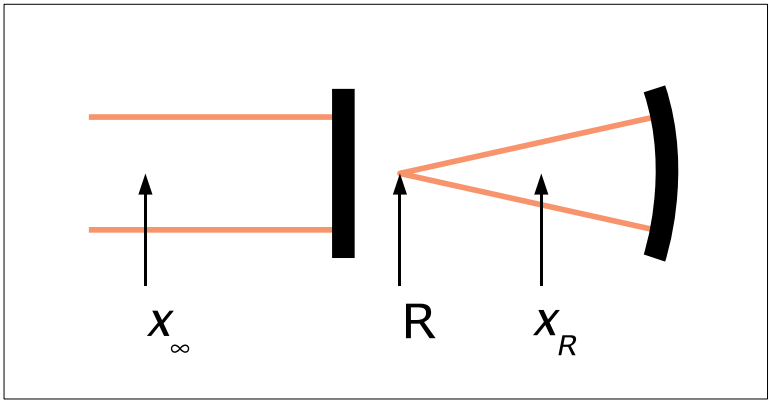

Figure 3.27: Illustration of the geometry underlying Eqs. (3.57), (3.58)

effects such as the variation of the laser intensity on the harmonics generating surface were not taken into account. Here, we discuss CHF under more realistic conditions.

In order to better understand CHF, we start by assembling some optical scaling laws for the broadband harmonics radiation. These laws are immediate consequences of Eq. (3.49). As the geometries and frequency spectra involved in CHF may be unusual, we also make an effort to give conditions of validity for the scaling laws in the cases when they are different from the ones for the fundamental Kirchhoff integral (3.49).

Before we start considering curved surfaces, we have a look at what happens, when the size of the focal spot is changed on a planar surface. So if the laser field is focused onto a planar surface and the focal spot size is varied but the maximum amplitude of the vector potential a_0 is kept constant:

$$F_-^{(1)}(0,\, r,\, t) = F_-^{(\alpha)}(0,\, \alpha r,\, t),$$

wherein α is the dimensionless factor describing the focal spot scaling, the reflected radiation scales as[13]:

$$\Rightarrow F_-^{(1)}(x,\, 0,\, t - x/c) \quad = \quad F_-^{(\alpha)}(\alpha^2 x,\, 0,\, t - \alpha^2 x/c). \tag{3.56}$$

Therefore, as long as Eq. (3.54) holds, a variation in the focal spot size will yield an exactly similar field structure in the far-field, just scaled in size.

Now we are interested in actively focusing the harmonics radiation. The most straightforward way to do so is the use of a curved surface for HHG, since it can do without relying on any optical components suitable for the extremely broadband radiation. We consider a confocal geometry, in the

[13] To obtain the result (3.56), $\pi\sigma^4/(4\lambda x^3) \ll 1$ must be assumed. Thus, for very high frequencies and small distances x Eq. (3.56) may not apply anymore.

sense that the field distribution $F_-^{(R)}$ of the radiation on the curved surface is the same as for the focal spot in the planar geometry $F_-^{(\infty)}$ - in both phase and intensity. This can be written as:

$$F_-^{(R)}(x = \sqrt{R^2 - r^2} - R,\, r,\, t) = F_-^{(\infty)}(0,\, r,\, t),$$

where R is the radius of the curved surface. We find that the field in front of the planar surface at the distance x_∞ is similar to that in front of the curved surface at the distance x_R, where x_∞ and x_R are related according to

$$\frac{1}{x_R} = \frac{1}{x_\infty} + \frac{1}{R} \tag{3.57}$$

In this case, the field relation is

$$\Rightarrow F_-^{(R)}(x_R,\, 0,\, t - x_R/c) \;=\; \frac{x_\infty}{x_R} F_-^{(\infty)}(x_\infty,\, 0,\, t - x_\infty/c). \tag{3.58}$$

This result becomes exact for small focusing solid angles, but also in the most interesting limit $x_R \to R$, which corresponds to the actual focal spot when there is no self-focusing present. The scaling law allows us to simply re-interpret all results obtained for a planar surface in subsection 3.3.3 to such for a spherical[14].

Next, we consider the variation of the focal distance, but keep the field amplitude at the surface and the solid angle constant:

$$\begin{aligned} F_-^{(\alpha)}(\alpha r,\, \theta,\, t) &= F_-^{(1)}(r,\, \theta,\, t) \\ \Rightarrow F_-^{(\alpha)}(0,\, t - \alpha r/c) &= \alpha F_-^{(1)}(0,\, t - r/c). \end{aligned} \tag{3.59}$$

So if the focal distance is varied, the intensity in the focal spot increases proportionally to the input power. Since a higher intensity at the surface generally creates a bigger number of harmonics and therefore leads to more than linear amplification of the radiation in the focal spot, we should aim for a focal distance as small as possible.

If the solid angle of the mirroring surface is varied, but the field amplitude and the focal distance are kept constant, the intensity in the focal spot increases stronger than the input power:

$$\begin{aligned} F_-^{(\alpha)}(R,\, \alpha\theta,\, t) &= F_-^{(1)}(R,\, \theta,\, t) \\ \Rightarrow F_-^{(\alpha)}(0,\, t) &= \alpha^2 F_-^{(1)}(0,\, t). \end{aligned} \tag{3.60}$$

This intensity gain is even stronger than the one achieved by the temporal focusing gain due to HHG. Therefore, to maximize the focal spot intensity

[14] Of course, as long as the condition (3.54) holds.

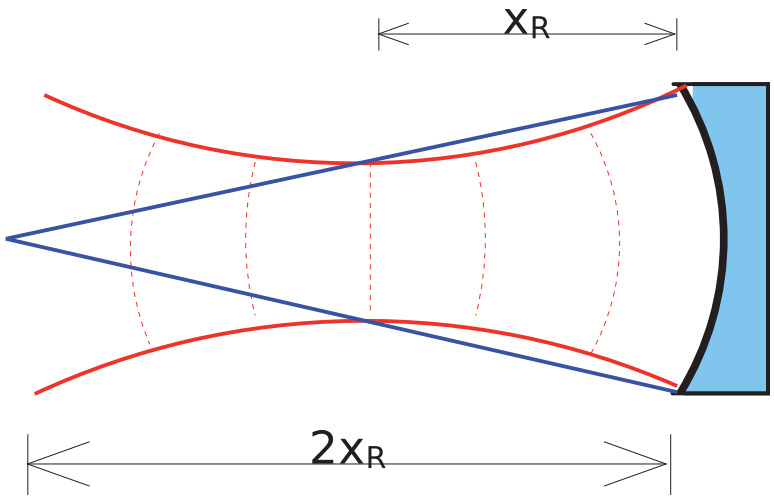

Figure 3.28: Suggested geometry for coherent focusing of the surface harmonics radiation, produced by a Gaussian laser beam. Ideally, the plasma surface should be designed in a way, that the S-parameter does not change with the distance from the optical axis.

with a constant laser power, it is first needed to maximize the solid angle of CHF. Of course, this solid angle is limited by the focusing geometry of the driving laser itself. Second, the CHF distance should be minimized in order to make maximum use of the temporal focusing gain due to surface HHG. As shown in subsection 3.3.3, the use of a constant-S surface would be ideal here, compare Fig. 3.25.

A focusing geometry that fulfils the above criteria is presented in Fig. 3.28. The laser is focused to a distance of one Rayleigh length x_R in front of the HHG surface. The plasma surface is spherically curved with a radius of $2x_R$ and the density of the surface is modulated in a way, that the S-parameter $S = n_e/(a_0 n_c)$ is constant everywhere. The harmonics radiation will then be coherently focused to a distance of $2x_R$ in front of the curved surface.

As an example, we have computed the output of this scheme for a laser pulse with a peak intensity of $I_0 = 5 \times 10^{24}\mathrm{W/cm}^2$ as it is expected for the European ELI (extreme light infrastructure) laser facility [5]. Here, our PIC simulations predicted an intensity enhancement by a factor of 3000 with the above geometry, yielding an impressive value of $I \sim 1.5 \times 10^{28}\mathrm{W/cm}^2$. With such a field intensity, it should be possible to observe clear signatures of QED vacuum non-linearities.

In this section, we have discussed the effect of diffraction on the HHG radiation under realistic conditions. To make maximum use of these, techniques to shape the focal spot or the plasma surface have to be implemented. With these techniques, it may be possible to produce intensities that are more than a thousand times higher than the conventional focusing intensity

of the laser, opening up the possibility of verifying vacuum QED effects with ultraintense laser systems.

Conclusions of Chapter 3

The reflection of relativistic light at overdense plasma surfaces, performing a strongly non-linear oscillation, is currently one of the most promising candidates for the production of intense attosecond pulses.

We have taken a fresh look at the theory of their generation. The foundations of the supposedly well-known ROM model have been re-investigated, yielding a clearer picture of the scope of application of the model. Further, the model has been extended to higher order γ-spikes, demonstrating the possibility of modulated spectral structures and power law spectra $I \propto \omega^{-q}$ with exponents $q < 8/3$ even within the ROM model. The explicit formulation of the TROM model and its comparison to the ROM model sheds additional light on the physics of relativistic high harmonics generation.

A third model was motivated by numerical observations: amazingly dense and narrow electron "nanobunches" may form at the plasma surface, emitting coherent synchrotron radiation efficiently. This nanobunching regime of relativistic HHG is optimal for attosecond pulse generation in the sense that the generated pulses bear almost the full energy of the entire optical cycle of the driving laser. Here, we expect a flat power law spectrum with $q \leq 4/3$ up to a smooth cut-off at a frequency which is determined either by the bunch relativistic energy $\omega_{rs} \propto \omega_0 \gamma^3$ or by the nanobunch width $\omega_{rf} \propto c/\delta$.

We have also studied carefully the phase properties of the relativistic harmonics, something that has largely been neglected so far. The relation of the electron surface motion to the spectral fine structure has been investigated. It has been found that the spectral fine structure can deliver valuable information on the motion of the electron surface on a femtosecond timescale.

The phase properties are also crucial when considering the free space propagation of the harmonic radiation. We have shown that diffraction can be harnessed as a spatial spectral filter for the harmonics radiation by designing the target surface or the laser pulse focal spot in the right way. This way, attosecond pulses can be extracted efficiently without the use of optical transmission filters.

Our study can further provide the basis for focusing schemes of the harmonics radiation. CHF (coherent harmonic focusing) has the potential to produce intensities that exceed the one of the driving laser by several orders of magnitude. Our proposed focusing scheme was shown to yield an intensity enhancement by a factor of 3000 with parameters as expected for the ELI facility. Here, unlike previous studies, we took a realistic Gaussian laser pulse geometry into account.

Chapter 4

Coherent Thomson Scattering at Laser Compressed and Accelerated Electron Bunches

The relativistic Doppler effect offers a fundamental means of frequency upconverting electromagnetic radiation. Light reflected by a mirror, that moves with a velocity close to c towards the incident light wave, is frequency upshifted by a factor of $\Gamma \approx 4\gamma^2$. But where to get such a mirror?

In 1993, Esarey *et al.* [61] mentioned the possibility of scattering light from fast moving electrons to upconvert its frequency. However, in the incoherent regime, the conversion efficiency of this process is rather poor. To greatly boost the efficiency, one needs to have a highly compressed bunch of electrons, since only then the scattering process can become coherent. The condition for coherency is, that the scale length of the electron bunch or its density gradient needs to be of the order of the wavelength *to be generated* or smaller. Since we target the VUV or even x-ray regime, this is much smaller than what can be reached by commonly used techniques, including conventional accelerators as well as laser-plasma accelerators.

However, laser acceleration of electrons in vacuum may provide a means to reach these tiny bunch sizes. In this scheme, electrons are extracted from a small droplet or a thin foil by a highly relativistic driver laser ($a_0 \equiv eA_0/mc^2 \gg 1$). The electron bunch becomes accelerated and at the same time compressed by the forces of the laser field. The acceleration can be achieved either by the relativistic $\mathbf{E} \times \mathbf{B}$-force of a conventional laser pulse, as suggested in Ref. [62], or by the longitudinal field on the optical axis of a radially polarized pulse [63], as suggested in Ref. [20]. In both cases, the bunch is compressed because of the laser pulse acting as a "snowplough" on the electrons. Spacecharge forces are counteracting the compression, thus limiting the amount of charge that can effectively be compressed. Nevertheless, in a wide range of parameters the edges of the electron bunches density

profile remain sharp, so that coherent Thomson scattering is still possible.

Consequently, two regimes of the discussed scheme can be distinguished. In the first regime, discussed e.g. in Ref. [62], the bunch as a whole scatters the radiation. Therefore, we refer to this regime as *bunch scattering* here. To achieve the necessary extreme compression, the charge density of the target has to be low enough so that Coulomb forces are negligible at least during the first acceleration phase. In the second regime, discussed e.g. in [64–66], the charge density of the target is higher. Although Coulomb forces are large here, leading to a rapid expansion of the target, the edges of the bunch may still be steep enough to scatter the radiation coherently for a certain interval of time after the electrons have been separated from the ions. In this chapter, we refer to it as the *edge scattering* regime.

In the edge scattering regime, the scattering efficiency is generally higher than in the bunch scattering regime due to the higher amount of charge. However, due to the rapid Coulomb explosion it is usually impossible to utilize more than the first half-cycle of the driver pulse for effective acceleration. Therefore, the bunch velocity is lower compared to the bunch scattering regime. Further, the possible duration of the probe pulse to be scattered is strictly limited.

In this chapter, we study the described scheme with an emphasis on the transition between the bunch scattering and the edge scattering regime. We use analytic models and PIC simulations to describe and analyze thoroughly the important physical effects. In section 4.1, the basic ideas behind the scheme are described. We show, that the snowplough effect in direct laser acceleration is an ideal candidate for the generation of compressed electron bunches for coherent scattering. We directly compare the two possible implementations of an "electromagnetic snowplough", i.e. the use of longitudinal field components on the one hand and the use of transverse components on the other. In section 4.2, we move to the discussion of the schemes under realistic conditions. Multidimensional effects and spacecharge repulsion play a crucial role here. Finally, the conversion efficiency is estimated. Techniques to increase the efficiency and gain further control over the generated radiation are suggested and discussed. Reaching best possible control over the temporal envelope of the driver pulse appears to be the most important issue here.

4.1 Compressing Electron Bunches for Coherent Thomson Scattering (CTS)

Coherent Thomson scattering can be much more efficient than its incoherent counterpart, since for coherent scattering the efficiency is proportional to the square of the number of scatterers and not to the number itself, as in the incoherent case. For a planar layer of resting electrons with a one-

dimensional density structure the efficiency is, expressed in normalized units

$$\eta = \pi^2 \left|\hat{n}(4\pi)\right|^2, \tag{4.1}$$

wherein $\hat{n}(k) = N_{cr}^{-1} \int N(x) e^{ikx} dx$ is the Fourier transform of the density distribution, and x must be measured in units of the laser wavelength. A smooth density profile may be approximated by a Gaussian, $N(x) = N_{cr} n \exp\left(-\left(x/\Delta\right)^2\right)$. For this sort of profile, the efficiency is

$$\eta = \pi^3 \left(n\Delta\right)^2 e^{-8\pi^2\Delta^2}. \tag{4.2}$$

That means, in case of a smooth profile, coherent scattering is most efficient for $\Delta^2 \lesssim 1/(8\pi^2) \sim 0.01$. The radiation is scattered at the bunch as a whole, and we will refer to this type of scattering as *bunch scattering*.

However, it is interesting to also consider density profiles that are not smooth, but contain a sharp edge and therefore cannot be approximated by a Gaussian profile. If there is a sharp edge in the density profile with a scale length much smaller than the scattering wavelength, it can be approximated by a Heaviside function: $N(x) = N_{cr} n\, \Theta(x)$. The function yields a scattering efficiency of

$$\eta = \frac{n^2}{16}. \tag{4.3}$$

This sort of scattering at a density discontinuity provides a chance of reaching reasonable efficiencies even without perfect bunch compression, and we will refer to it as *edge scattering*.

If the electrons are moving fast in the direction opposite to the scattering laser pulse, the frequency of the backscattered radiation will be upshifted by the factor $\Gamma = (1+\beta_x)/(1-\beta_x)$ because of the relativistic Doppler effect. Now, the condition for coherency has to be considered in the rest frame of the scatterers. Transforming it back to the laboratory frame, it yields the condition

$$\Delta_{\text{eff}} \equiv \frac{\Delta}{1-\beta_x} \ll 1. \tag{4.4}$$

We call Δ_{eff} "effective bunch width", since it is the normalized width that effectively has to be considered when the bunch is to be used for backscattering. Eq. (4.4) means, that the bunch length in the laboratory frame has to be distinctly smaller than the wavelength to be produced. Since we aim at VUV and x-ray radiation, this is a challenge indeed. But, as we will see, the snowplough effect may provide a means for achieving the required compression.

Let us start with a simple analytic argument. Assume a force moving with constant speed v_{ph} - such as a plane electromagnetic wave - acting on a small bunch of initially resting electrons. Further assume that the

bunch charge is low, so that spacecharge effects can be neglected. The force will then result in an acceleration α of the bunch electrons that retains the translational symmetry of the original force: $\alpha(x, t) = \alpha(x - v_{ph}t)$. If the force accelerates the electrons in its own propagation direction, the bunch will become compressed like snow in front of a snowplough. Considering only the translational symmetry, we find, that the bunch is compressed to the size

$$\frac{\Delta}{\Delta_0} = 1 - \frac{v_x}{v_{ph}}. \tag{4.5}$$

This simple but highly remarkable result means that in the case $v_{ph} = c$, the effective bunch length Δ_{eff} is preserved during the entire acceleration process. Thus radiation, which could initially be scattered coherently at the electron bunch, can still be scattered by the accelerated bunch, though its wavelength could be much smaller in the rest frame of the electrons. This is the reason why the snowplough compression can be considered an ideal candidate for the compression of electron bunches for CTS.

The question remains, which actual force implements such an acceleration. Two options are discussed here:

- the longitudinal $\mathbf{E} \times \mathbf{B}$-force, provided by the transverse fields of a circularly or linearly polarized laser mode,
- the longitudinal electric field on the optical axis of a radially polarized laser mode.

In both cases, the phase velocity v_{ph} is only a little greater than the vacuum light speed c, so that the compression is close to ideal, as seen from Eq. (4.5). More precisely: A Gaussian or Hermite-Gaussian TM_{01} laser pulse takes on its maximum phase velocity in the focal spot, given by $v_{ph}/c = x_{Rl}^2/\left(x_{Rl}\left(x_{Rl} - g\lambda/(2\pi)\right)\right)$, where $x_{Rl} = \pi\sigma^2/\lambda$ is the Rayleigh length and $g = 1$ for the Gaussian and $g = 2$ for the TM_{01} mode. Since the minimum wavelength that can coherently be generated from an electron bunch is directly related to its size and the minimum compression size is related to the phase velocity via Eq. (4.5), we can estimate a lower limit for the focal spot size that can be used to accelerate and compress an electron bunch that is able to generate radiation with a certain wavelength $\tilde{\lambda}$:

$$\frac{\sigma}{\lambda} > \sqrt{\frac{5\Delta_0}{g\pi^2\tilde{\lambda}}}. \tag{4.6}$$

This limitation is not a very strong one. When e.g. aiming at a wavelength as small as $\tilde{\lambda} = \lambda/1000$, using a foil with initial thickness $\Delta_0 = 0.1\lambda$ and a linearly polarized driver pulse, we get the condition $\sigma > 7\lambda$ - thus still rather small focal spots are allowed.

Let us take a closer look at the direct electron acceleration and compression via the transverse electric field. We express the momentum in terms

of the vector potential. This can be done by making use of the appropriate laws of conservation derived from the Hamiltonian of the particular system. For a plane wave we obtain the well known formulae:

$$\mathbf{P}_\perp = \mathbf{A}_\perp \tag{4.7}$$

$$P_x = \frac{A_\perp^2}{2}, \tag{4.8}$$

where $\mathbf{P}$ is the particle momentum, $\mathbf{A}_\perp$ is the vector potential associated with the electromagnetic wave and relativistically normalized units are used[1]. Using (4.7) and (4.8), the Doppler factor for backscattered light can be determined:

$$\Gamma_{\mathrm{DCR}} \equiv \frac{1+\beta_x}{1-\beta_x} = 1 + A_\perp^2. \tag{4.9}$$

Now we come to the acceleration via longitudinal field. For a particle exactly on the optical axis of a radially polarized pulse the transverse momentum is zero, as there is no transverse field on the optical axis. For the longitudinal momentum we obtain, assuming $v_{ph} = c$:

$$P_x = \frac{A_x - 2}{2A_x - 2} A_x. \tag{4.10}$$

Note that the solution is singular for $A_x \to 1$, meaning that there is no dephasing. A test particle can, in principle, be accelerated to infinite energy even if the vector potential takes on only finite values. On the first look, this may seem unreasonable, but it is not, since our precondition $v_{ph} = c$ also implies $\sigma = \infty$, that means that such a pulse would necessarily contain infinite energy. Therefore, to reveal the actual capability of longitudinal field acceleration, it is mandatory to consider forces with phase velocity different from c. On doing this, we obtain:

$$P_x = \frac{1}{v_{ph}^2 - 1}\left[(A_x - 1)\, v_{ph} + \sqrt{(A_x-1)^2 + v_{ph}^2 - 1}\right] \approx \frac{A_x}{v_{ph} - 1}. \tag{4.11}$$

Because of dephasing there is no singularity anymore. Still, in the common case $v_{ph} \gtrapprox c$, P_x grows extremely fast. Additionally, the fact that there is no transverse velocity component further supports the growth of the Doppler conversion rate Γ. Figure 4.1 shows the expected Doppler conversion ratio as a function of the dimensionless amplitude for longitudinal and transverse fields. From this point of view, the use of radially polarized pulses for direct acceleration appears very tempting.

[1] $\mathbf{P}/m_e c \to \mathbf{P}$, $e\mathbf{A}/m_e c^2 \to \mathbf{A}$

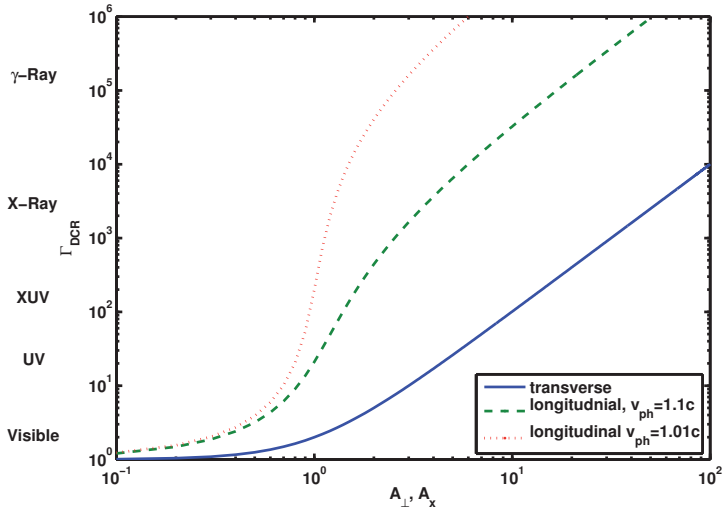

Figure 4.1: Comparison of the theoretically achievable Doppler conversion rate $\Gamma_{\mathrm{DCR}} = (1+\beta_x)/(1-\beta_x)$ for scattering at electrons accelerated via longitudinal field according to Eq. (4.11) or transverse field according to Eq. (4.9). Phase velocities $v_{ph}/c = 1.1\,(1.01)$ correspond to the maximum v_{ph} for TM_{01} laser beams with $\sigma/\lambda = 1.1\,(3.2)$.

4.2 Numerical Studies under More Realistic Assumptions

In the previous section we have demonstrated, that directly laser accelerated electron bunches seem to be ideally suited for light frequency upconversion via CTS. The theoretical minimum requirement is just a laser reaching relativistic amplitudes of $\mathbf{A}_\perp \gg 1$ or even, in case of acceleration via longitudinal field, only $A_x > 1$. This is something that nowadays is available in university scale laboratories. However, in the first simple estimates we have neglected spacecharge and most multidimensional effects. In this section we discuss the effects that have been ignored so far, aiming to answer the question how efficient and controllable the proposed setup can be in reality and which difficulties have to be overcome to realize it experimentally.

Numerical simulations are therefore utilized. Most of the simulations in this chapter are carried out at rather moderate frequency conversion ratios ($\Gamma_{\mathrm{DCR}} \sim 10$), because in this regime many of the interesting effects are already visible and the simulations are very accurate and quick to run so that it is possible to cover a large parameter region. In subsection 4.2.6, we consider the luring possibility to scale the scheme up to very high frequency conversion ratios, as indicated by Fig. 4.1.

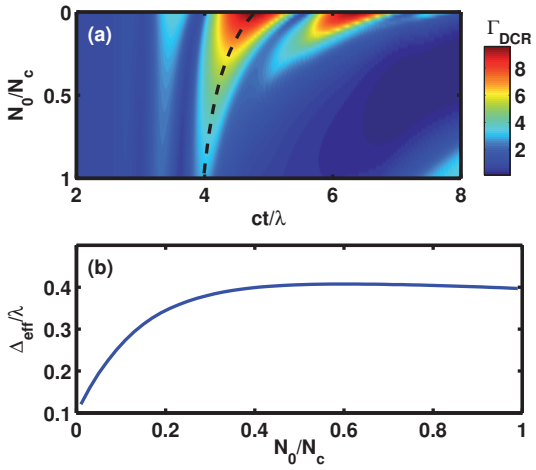

Figure 4.2: Results of a series of 1D PIC simulations of direct electron acceleration in vacuum, using a driver laser with amplitude $a_0 = 3$ and Gaussian temporal profile $E \propto \exp(-(ct/\lambda)^2)$. The initial foil width $\Delta_0 = 0.1\,\lambda$ was chosen and the density N_0 was varied. We display the key magnitudes interesting for frequency upconversion via CTS: (a) the expected Doppler conversion rate $\Gamma_{\mathrm{DCR}} = (1+\beta_x)/(1-\beta_x)$ from the electron bunch and (b) the effective bunch width Δ_{eff} at the time, where the electron bunch reaches its maximum longitudinal velocity. A perfect snowplough effect without the perturbing effect of Coulomb repulsion would lead to $\Delta_{\mathrm{eff}} = \Delta_0$.

4.2.1 Spacecharge effects

Since we know that for CTS the scattering efficiency goes up with the square of the accelerated charge [compare Eq. (4.1)], it is of course desirable to accelerate and compress as much charge as possible. On the other hand, as soon as the electrons are detached from the plasma background charge, a Coulomb explosion will take place, working against the snowplough compression. The speed of the explosion depends on the amount of charge involved. This means, that for a given driver pulse there will be an optimum charge amount, governing the choice of material and foil thickness in a real experiment.

To evaluate the magnitude of this effect, we run a series of 1D PIC simulations. Simulations are carried out for different initial densities N_0 and laser amplitudes a_0. In each simulation, we record the average longitudinal velocity β_x of the bunch electrons and use it to calculate the expected Doppler conversion rate Γ_{DCR} of the electron bunch. Then we denote the value of Δ_{eff} at the instant, when Γ_{DCR} reaches its maximum. In order to calculate Δ_{eff}, the bunch size Δ was obtained by computing the root mean square deviation of the particles positions, $\Delta^2 := \sum_p (X_p - \langle X \rangle)^2$. It is then divided by $1-\beta_x$, yielding the effective bunch width Δ_{eff}. The outcome is

displayed in Fig. 4.2.

In the limit of very low electron numbers, we confirm the results of the previous section 4.1: Γ_{DCR} reaches a maximum of about 10, corresponding to Eq. (4.9), and the bunch becomes compressed according to the ideal snowplough effect, resulting in $\Delta_{\mathrm{eff}} \approx \Delta_0$, as predicted by Eq. (4.5).

For moderate initial charge densities $N_0 \lesssim 0.1\, N_c$, the effective bunch length at the velocity maximum grows approximately linearly with the initial density: $\Delta_{\mathrm{eff}}/\Delta_0 \approx 1 + \alpha N_0/N_c$, with $\alpha \approx 20$ in our case. Simulations show that if higher field amplitudes a_0 are used, yielding higher Γ_{DCR}, the slope of $\Delta_{\mathrm{eff}}(N_0)$ is even steeper. This can be explained because the acceleration takes more time, giving the bunch more time to spread, and further the demand for compression is even higher at high Γ_{DCR}. Furthermore, the maximum average velocity decreases for large average densities, and consequently also the expected Doppler conversion rate Γ_{DCR} for bunch scattering. This leads to Δ_{eff} reaching a quasi-plateau and even declining slightly for large initial densities $N_0 > 0.4\, N_c$.

Let us now estimate the optimal initial density and efficiency for pure bunch scattering. Assuming a Gaussian density profile, we expect the optimal efficiency to lie within the linear density regime, as the exponential decay in Eq. (4.2) yields extremely low efficiency for bunches as wide as $\Delta_{\mathrm{eff}} \approx 0.4\, \lambda$. Thus, we can estimate optimal initial density for CTS applications from the linear relation given above. Taking the wavelengths of the probing and driving laser to be the same ($\lambda_p = \lambda_d$), the resulting optimal density is $N_{opt}/N_c = \alpha^{-1}\left[-0.5 + \sqrt{0.25 + 1/(8\pi^2\Delta_0^2)}\right]$. In the considered example, this amounts to $N_{opt}/N_c \approx 0.04$. By inserting this into Eq. (4.2), we calculate an optimal efficiency of about $\eta \approx 4 \times 10^{-5}$.

This is the optimal scattering efficiency under the assumption of a smooth bunch density profile. However, looking at the real density profiles (Fig. 4.3) of the accelerated electrons, we notice that they are generally not smooth but contain sharp edges. Thus we expect, that although at higher densities CTS is effectively not possible at the bunch as a whole, scattering at the edges may still work. The efficiency of the backscattering process then depends on the height of the density jump, see Eq. (4.3).

During the ultrafast process of acceleration and compression thermal effects are negligible, therefore the numerically observed conservation of the sharp density edges appears physically sound. It is not difficult to show that both the snowplough compression and the Coulomb explosion, considered in isolation, just maintain the initial rectangular density profile of the bunch, changing only its extension. In the highly relativistic regime under consideration, both effects couple in a complicated manner. This leads to an actual change in shape, but still the sharpness of the edges of the density distribution is conserved. For $N_0 = 0.29\, N_c$, the rear edge even turns into a δ-like peak.

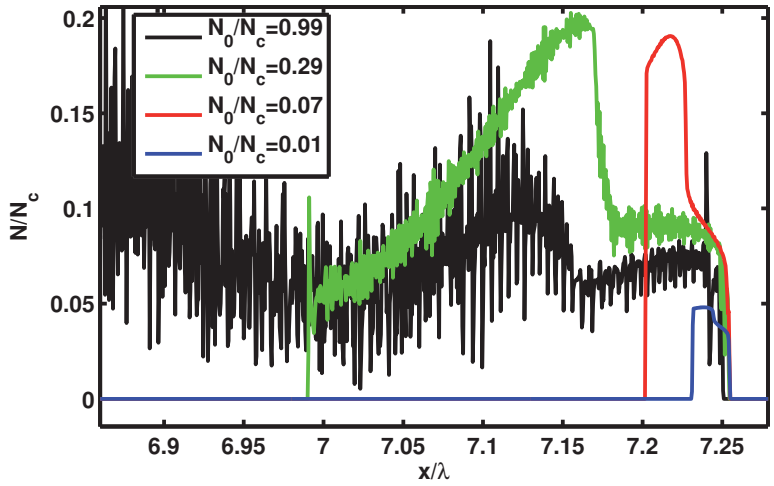

Figure 4.3: Density profiles of the accelerated and compressed electron bunches at maximum velocity for different initial densities. The driver laser was the same as in Fig. 4.2, $a_0 = 3$.

A possible explanation for this is the light pressure gradient inside the thin foil. From a certain point in time, the front part of the bunch reflects a significant part of the driver light, so that a ponderomotive potential gradient builds up inside the foil, leading to an additional compression force that might in certain areas even overcompensate the spacecharge repulsion. Also one notices that, starting from a certain value, the height of the density jump depends only weakly on the initial density. This suggests that the CTS conversion efficiency will reach a plateau at that point for the frequency corresponding to the leading edges velocity.

So far, the motion of electron bunches directly accelerated by lasers in vacuum has been examined. In Fig. 4.4 the light actually backscattered from these bunches is depicted. To keep matters as simple as possible, a non-relativistic scattering laser ($a_0^{(Sc)} = 0.1$) was used with the same frequency as the driver. The polarization of the scattering laser was perpendicular to the one of the linearly polarized driver, so that the scattered radiation could easily be separated from the intense driver radiation with high numerical accuracy. The driver laser in the simulations of Fig 4.4 has an amplitude of $a_0 = 3$, so we can expect a maximum Doppler conversion rate of $\Gamma_{\mathrm{DCR}} = 10$ in the low charge limit according to Eq. (4.9). The average generated frequency is slightly lower though for very low charges and the spectrum is quite broad. This can be understood, because the bunch velocity keeps changing during the scattering process. If the amount of charge is increased, the frequencies generated decrease as expected from Fig. 4.2. Further, for a wide range of initial densities we observe two or even more spectral lines.

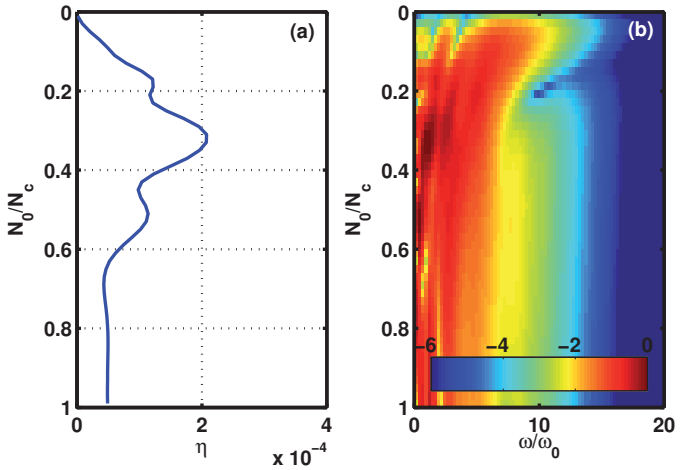

Figure 4.4: (a) Energy conversion efficiency η and (b) spectra of scattered light from laser accelerated bunches of different initial densities. The driver pulse is the same as in the previous figures, temporally Gaussian and $a_0 = 3$. In (b), the colourscale corresponds to the logarithm of the normalized spectral intensity.

This can be explained due to the jumps in the density profiles (see Fig. 4.3) which are moving at different velocities, thus generating separate spectral lines.

4.2.2 Acceleration via longitudinal field of a radially polarized laser pulse

Let us now have a look at the electron bunch acceleration via longitudinal field. As could be seen from Fig. 4.1 in the first section of this chapter, the acceleration via longitudinal field promises much higher frequency conversion ratios especially at moderate field amplitudes. However, there are also additional restrictions arising for longitudinal field acceleration which should not be concealed.

The first restriction is the inherent transverse inhomogeneity of the field. Since the longitudinal field component is closely related to the gradient of the radial field, its transverse extension is fundamentally limited, no matter how big the focal spot is made. For the Hermite-Gaussian TM_{01}-mode one finds the critical radius, where the radial field component overtakes the longitudinal one, to be:

$$r_c = \frac{\pi^2 \sigma}{2} \left(\sqrt{\frac{\sigma^2}{\lambda^2} + \frac{4}{\pi^4}} \right) \underset{\sigma \gg \lambda}{\approx} \frac{\lambda}{\pi^2}. \tag{4.12}$$

This radius also marks an upper limit for the transverse size of an electron

bunch to be accelerated and compressed about uniformly by the longitudinal field component.

The second restriction is caused by the Coulomb forces, which are an even bigger problem in the case of longitudinal field acceleration. For acceleration via transverse field, there are two effects mitigating the Coulomb explosion and thus helping to keep the electron bunch together. First, because of their transverse velocity component, the electrons already reach relativistic velocities before they are detached from the ion background charge. This results in an increased effective mass, slowing down the Coulomb explosion. Second, the magnetic force of the parallel currents partially compensates the electrostatic repulsion, as already mentioned in [62]. These benefits do not exist in the case of acceleration via longitudinal field.

Still, the use of radially polarized drivers appears interesting at least for moderate driver intensities. Therefore, we use a 2D PIC simulation to demonstrate the feasibility of the scheme with a 10 TW driver laser. The PIC results are cross-checked with direct numerical solutions of the equation of motion of test particles in the analytically provided field of the driver laser. The direct solution avoids issues with the finite spatial grid resolution typical for PIC simulation, but does not self-consistently include the Coulomb repulsion of the electrons. However, as we work with quite low bunch charge in the PIC simulation, the results should be comparable. To obtain reasonable agreement between both, it is crucial to employ the exact short pulse description (see Chapter 2) in both PIC simulation and model. For the sake of computational efficiency, the PIC simulation was performed in a Lorentz transformed system, co-moving with the electrons. In the simulation run presented here, a transformation velocity of $\beta = 0.7$ proved to be optimal[2].

Typical results are depicted in Fig. 4.5. We find, that the averaged bunch momentum [Fig. 4.5(a)] reaches a maximum value around $ct_S = 4.8\,\lambda$. Then, after going through a decelerating phase, the bunch becomes accelerated again, entering the second optical cycle of the driver laser. Looking at the bunch spread [Fig. 4.5(b) and (c)], we notice that the bunch is torn apart here. Consequently, coherent scattering is only possible during the first acceleration stage.

A series of further simulations carried out for longitudinal field acceleration at various parameters confirmed, that the phase transitions from one accelerating phase to the next are highly critical for the maintenance of the bunch compression. If the electrons gain different transverse velocities at a point, where $v_x \approx 0$, the bunch instantly looses its shape. This results from a combination of the small transverse component of the laser field near the optical axis and, especially for higher amounts of charge to be accelerated,

[2]For higher transformation velocities, the spatial and temporal offsets required for the simulation box would nullify the efficiency gain from the Lorentz transformation.

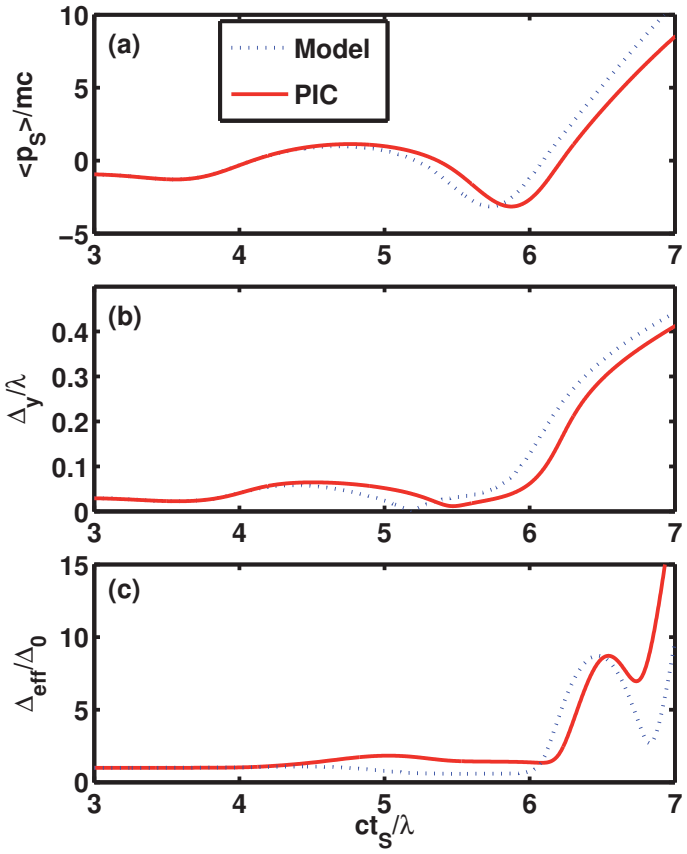

Figure 4.5: The bunch trajectories in 2D PIC and the 2D model, considering the motion of only four test particles in a given laser field. PIC was carried out in a Lorentz transformed system, using $\beta = 0.7$ in direction of the driver pulse. The subscript S indicates, that the magnitude is taken in the simulation frame rather than in the laboratory frame. The plots show (a) the averaged electron momentum in relativistically normalized units, (b) the transverse bunch spread and (c) the effective bunch width, normalized to the initial bunch width. Simulation parameters were: focal spot size $\sigma = 2\lambda$, longitudinal field corresponding to a laser power (assuming actual 3D geometry) $P = 10\,\mathrm{TW}$, initial bunch diameter $\Delta_0 = 0.1\lambda$. In the PIC simulation, the initial electron density was $N = 0.01\,N_c$.

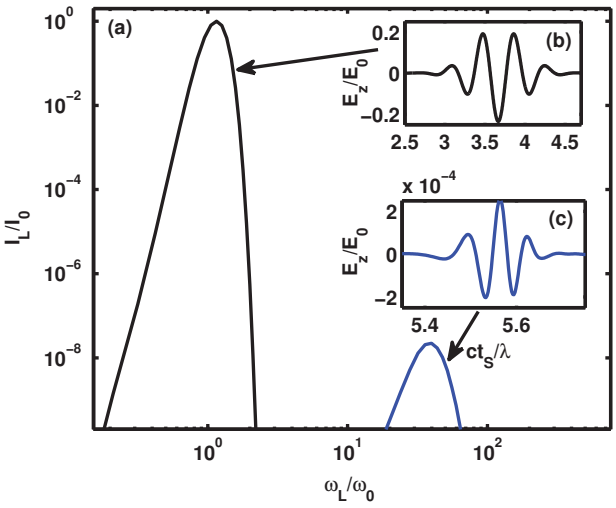

Figure 4.6: Probe and scattered radiation in (a) spectrum and (b)-(c) time domain. The time domain pictures are taken in the simulation frame, but the spectrum is transformed back to the laboratory system.

also from the Coulomb forces between the electrons. During the stages where the electrons are moving fast, they possess a high effective mass $\gamma \gg 1$, so that the transverse forces do not affect the bunch angular spread anymore. It is best to use the electrons in the first acceleration stage to guarantee for a stable, strong enough compression.

In Fig. 4.6, the result of scattering is displayed. Even if only the first acceleration stage could be used, the frequency of the scattered radiation is upshifted by a factor of $\Gamma_{\mathrm{DCR}} = 40$ in the laboratory system. To obtain this factor with an ordinary linearly polarized driver pulse, a power of at least $P \sim 100\,\mathrm{TW}$ would be required. The integrated energy efficiency lies in the order of $\eta = 10^{-6}$, which roughly agrees with Eq. (4.2), when estimating the effective bunch width from Fig. 4.5(c). This indicates that - in contrast to the acceleration via transverse field - the edges of the bunch density profile soften during acceleration, so that the profile becomes approximately Gaussian.

We observe another interesting detail in Fig. 4.6(c). The scattered pulse appears slightly chirped, starting at low frequencies and ending at higher ones. This indicates, that the reflecting electron bunch was accelerated during the scattering process.

To conclude, we found that the scheme utilizing the longitudinal field component of a radially polarized pulse appears interesting especially for moderate driver powers. It was shown via PIC simulation, that the scheme is actually feasible, but its limitations with respect to efficiency are grave. Therefore, we now turn our attention back to acceleration via transverse field

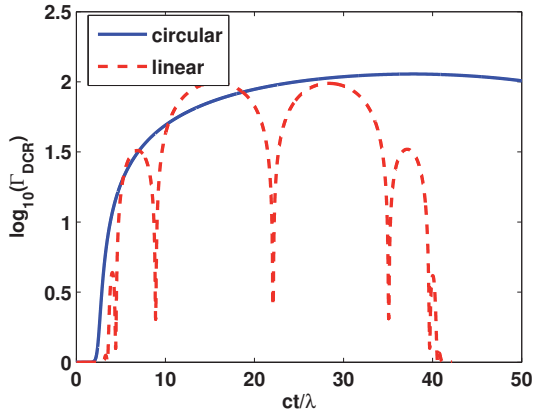

Figure 4.7: Semi-logarithmic plot of the time dependence of the Doppler factor of a single electron (or low charge electron bunch) accelerated by a plane, temporally Gaussian laser pulse. The red dashed line corresponds to a linearly polarized mode, the blue solid line to a circularly polarized one. Both pulses have the same amplitude ($a_0 = 10$) and duration ($\tau = \lambda/c$).

component.

4.2.3 Linear versus circular polarization

For transverse field acceleration, the use of both linearly and circularly polarized driver lasers may be considered. Given the same average power, linearly polarized pulses of course reach higher field amplitudes, but $A_\perp^2(x,t)$ is a strongly oscillating function, thus oscillations of $\Gamma_{\mathrm{DCR}}(t) = 1 + A_\perp^2(x_{el}(t), t)$ follow. For a circularly polarized laser pulse, $\Gamma_{\mathrm{DCR}}(t)$ is determined by the envelope of the laser pulse and not by its optical cycle. This means, that by controlling the envelope of the driver pulse, wide control over the frequency of the scattered radiation can be achieved.

The difference is illustrated by the actual solution of the equation of motion of a test electron in the laser field in both cases, shown in Fig. 4.7. Not only the fluctuations in Γ_{DCR} are much smaller for a circularly polarized driver, but also the net period, where Γ_{DCR} is high, is distinctly longer at the same driver pulse duration. Therefore, the use of a circularly polarized driver is recommended to maximize the stability of the scheme under discussion.

4.2.4 Finite focal spot size

A strict limitation on the transverse bunch size like Eq. (4.12) does not exist for acceleration through the $\mathbf{E} \times \mathbf{B}$-force of a linearly or circularly polarized pulse. The electron bunch can in principle be extended to any size in the directions normal to the optical axis, if only enough power is available to

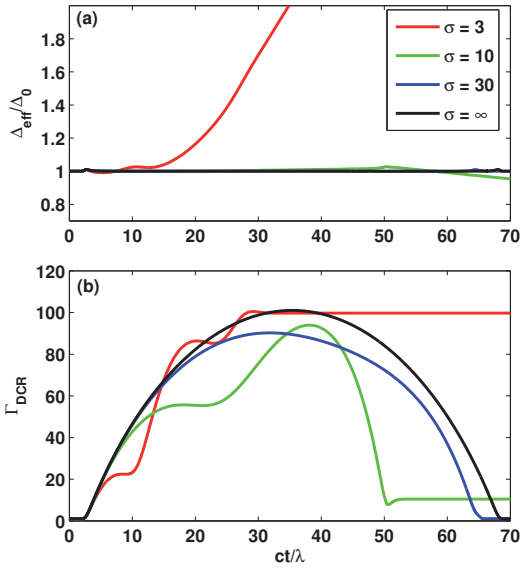

Figure 4.8: The temporal evolution of the Doppler conversion rate Γ_{DCR} and the effective bunch length $\Delta_{\mathrm{eff}}/\Delta_0$ as a function of time for different focal spot sizes σ. The laser pulse is circularly polarized, having a Gaussian profile in both longitudinal and transverse direction. Parameters are $a_0 = 10$, $\tau = \lambda/c$ and the initial electron distance $\Delta_0 = 0.1\lambda$, spacecharge is not taken into account here.

increase the size of the driver laser focal spot accordingly. However, since the power available in real experiments is limited, it is necessary to focus the laser down to small spot sizes to reach sufficient intensities. Small spot sizes on the other hand lead to electrons escaping from the laser beam region sideways.

First, we estimate the lower limit for the focal spot size to capture at least some electrons and compress and accelerate them inside the beam. This condition on the spot size is usually stronger than the one stemming from the increase in phase velocity, Eq. (4.6). Certainly, it should be within the order of magnitude the amplitude of the transverse electron motion in a plane wave: $r_0 = a_0\lambda/2\pi$.

We check and quantify the effects of finite laser pulse diameter by integrating the equation of motion for test particles. Spacecharge effects are purposely not taken into account to examine the effect of finite focal spot size well separated here. Fig. 4.8 shows the key parameters Δ_{eff} and Γ_{DCR}, representing the bunch compression and velocity, for two charges accelerated by a finite-diameter Gaussian pulse.

In Fig. 4.8(a) it can be seen, that for the escaping bunch (red line, $\sigma = 3$) Δ_{eff} is increasing rapidly even without spacecharge effects. Obviously, the strong field inhomogeneity destroys the snowplough compression. Therefore we conclude, that it is not appropriate for CTS. The other electrons, accelerated by a pulse with $\sigma \geq a_0\lambda$, remain inside the field region and are stopped ($\sigma = 30, \infty$) or almost stopped ($\sigma = 10$), when they leave the influence area of the laser pulse due to dephasing. Here, due to the unperturbed snowplough effect, Δ_{eff} is almost constant. These bunches can be utilized for CTS.

It is also interesting to look at $\Gamma_{\text{DCR}}(t)$ for different σ [Fig. 4.8(b)]. For $\sigma = 3\lambda$, because of the strong transverse field inhomogeneity, Eq. (4.8) is invalidated and the electrons can maintain their full momentum outside the pulse region. However, as we have seen before, the bunch compression is poor in this case. Even for a focal spot as large as $\sigma = 10\lambda = 2\pi r_0$, there are considerable deviations from the ideal plane wave case ($\sigma = \infty$). The period of time at maximum velocity is considerably shorter here compared to the plane wave. Only at $\sigma = 30\lambda = 6\pi r_0$, the difference to $\sigma = \infty$ starts to vanish.

We conclude that larger driver beam diameters ($\sigma \gg r_0$) are generally advantageous and yield a more stable acceleration.

4.2.5 Pulses with a sharp rising edge

In subsection 4.2.1 we have seen, that the efficiency for scattering at the electron bunch is mainly determined by the height of the rising edge of the bunch density profile. This edge is widely invariant under changes of the initial foil thickness and charge. However, there is a way to increase the

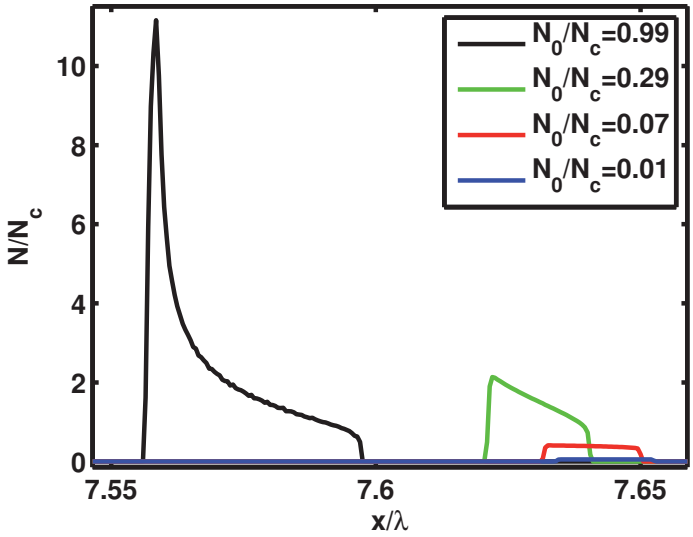

Figure 4.9: Density profiles of the accelerated and compressed electron bunches at maximum velocity for different initial densities. This time the a driver laser ($a_0 = 3$) with a sharp rising edge (eq. 4.13) was used instead of a Gaussian, compare figure 4.3.

scattering efficiency, and that is sharpening the rising edge profile of the driver lasers. To demonstrate the potential, we consider an ideally steep profile, described by[3]:

$$E(t) = E_0\,\theta(\omega_0 t + \pi)\theta(-\omega_0 t + \pi)\,\cos(\omega_0 t). \tag{4.13}$$

With the steep pulse profile a better compression can be expected, because acceleration and compression happen much faster here than in the case of the Gaussian pulse, and so there is less time for the Coulomb explosion.

In figures 4.9 and 4.10, some PIC results for this pulse shape are shown. When comparing Fig. 4.9 to Fig. 4.3, we see that the jump in the density profile at maximum velocity indeed increases considerably. Even at high initial densities ($N_0/N_c \approx 1$) the bunch stays together and is accelerated as a whole. Therefore, we can expect a distinct boost in CTS efficiency η. As a matter of fact, η is increased by about two orders of magnitude, as the reader may verify by comparing Fig. 4.10 to 4.4.

Still we notice, that the denser bunches stay behind in comparison to the less denser bunches. Consequently, also Γ_{DCR} goes down with increased

[3]Although the rear part is not important for our purpose, we write the full pulse profile like this. The reason is that this way the pulse may consistently be extended to a finite 3D structure with linear polarization, fulfilling the integral conditions $\int_{-\infty}^{\infty} \mathbf{E}\,\mathrm{d}t = \int_{-\infty}^{\infty} \mathbf{A}_\perp \mathrm{d}x = 0$. The feasibility of ultrashort pulse structure in 3D has been discussed in detail in chapter 2.

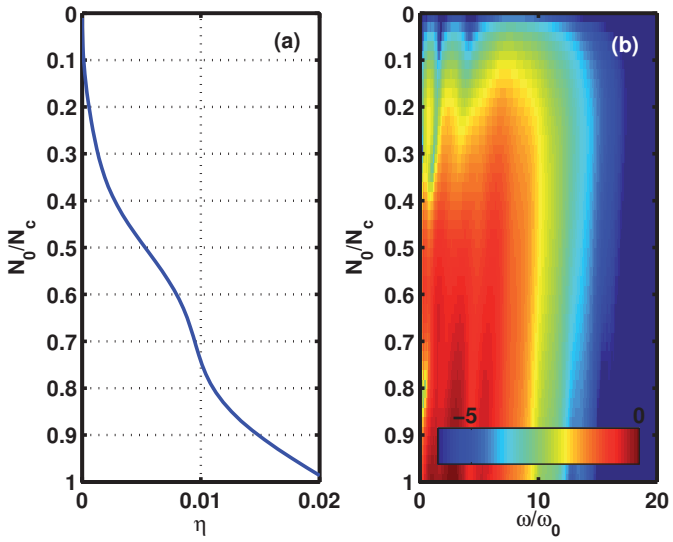

Figure 4.10: (a) Net efficiency and (b) spectra of scattered light from laser accelerated bunches of different initial densities, using a driver laser ($a_0 = 3$) with a sharp rising edge. Compare this to figure 4.4.

charge. For $N_0/N_c \approx 1$, the electron velocity at its maximum is lower by about a factor of two compared to the low charge limit. It appears that now an increase in the bunch charge, instead of causing a Coulomb explosion, results in an increased overall inertia of the bunch. A possible explanation for this is that the bunch reflects some part of the driver radiation during acceleration at these densities. This reflection consumes the driver power after some time, but also causes a gradient of light pressure inside the bunch, steepening the density profile.

To sum up, a steep rising edge of the driver laser leads to a huge gain in scattering efficiency and appears to be an indispensable key factor for the successful implementation of the proposed scheme.

4.2.6 Scaling up to the x-ray regime

Up to now, we thoroughly discussed the scheme for moderate frequency conversion ratios $\Gamma_{\mathrm{DCR}} \lesssim 10$. This discussion gave us some general idea about what is crucial to achieve reasonable conversion efficiencies. Nonetheless it is an exciting question how efficiently it is possible to scale the scheme up to extremely high frequency conversion ratios, finally targeting the x-ray regime.

Scaling up the frequency of course brings about some additional difficulties: Because of the generally longer acceleration period and the need for even smaller bunch sizes, spacecharge repulsion becomes more critical.

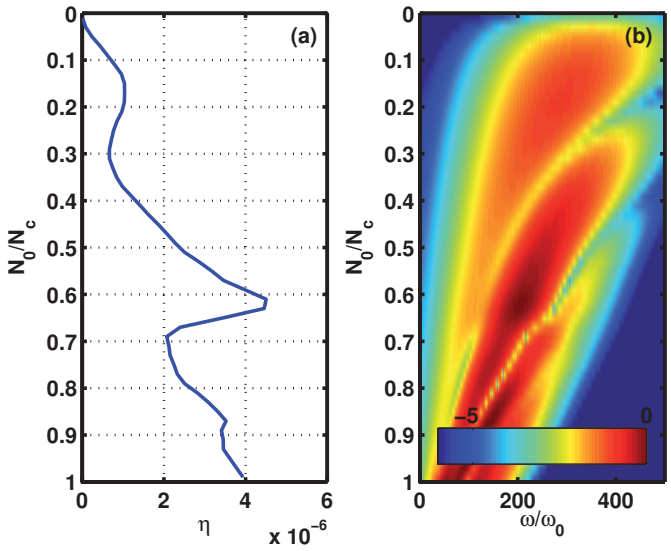

Figure 4.11: (a) Net efficiency and (b) spectra of scattered light from laser accelerated bunches of different initial densities, using a driver laser ($a_0 = 20$) with a sharp rising edge. Compare to Figs. 4.4 and 4.10.

Consequently, conversion efficiencies cannot be expected to be the same as for lower Γ_{DCR}. Our attempts to use conventional, smooth temporal profile laser pulses or radially polarized modes to reach the x-ray regime have resulted in poor efficiencies, hardly measurable even inside our numerical simulations.

But, utilizing a pulse with an extremely sharp leading edge we were able to obtain some more encouraging results. In Fig. 4.11, the outcome of a series of 1D PIC simulations is shown. Here, we used a laser amplitude of $a_0 = 20$, targeting a frequency upconversion rate of $\Gamma_{\mathrm{DCR}} \lesssim 400$. It is observed that the best scattering efficiency can be reached with an initial density of $N_0 = 0.6\, N_c$, leading to an efficiency of $\eta \approx 4 \times 10^{-6}$ with an upconversion ratio of about $\Gamma_{\mathrm{DCR}} \approx 200$. For a Ti:Sa laser ($\lambda = 0.8\,\mu$m), this would correspond to a photon energy of about 300 eV in the soft x-ray regime. The laser amplitude $a_0 = 20$ used in Fig. 4.11 is already within reach of present day laser systems. However, the extremely steep rising edge of the field envelope, which is crucial for the compression of the bunch, is for sure still a challenge for today's experiments.

Conclusions of Chapter 4

In this chapter we have studied coherent Thomson scattering at laser compressed and accelerated electron bunches as a scheme for generation of co-

herent XUV or x-ray radiation.

The condition for coherent scattering at a moving bunch implies that the bunch possesses a structure that is smaller than the wavelength generated in the scattering process. For XUV or x-ray radiation, this is certainly a big challenge. However, it seems that the snowplough effect by laser acceleration in vacuum can actually meet this challenge, since it rigorously conserves the "effective bunch width" $\Delta_{\mathrm{eff}} \equiv \Delta/(1-\beta_x)$ at least when spacecharge and multidimensional effects are neglected. To reveal the magnitude of these effects in a realistic setup, we carry out numerical simulations.

Here, two variants of the acceleration scheme have been examined: (a) the use of the longitudinal electric field on the optical axis of a radially polarized TM_{01} mode and (b) the use of a conventional circularly or linearly polarized laser pulse, utilizing the relativistic $\mathbf{E}\times\mathbf{B}$-force. Both variants have their advantages: Scheme (a) yields extremely high frequency conversion ratios even for moderate driving powers, whereas (b) produces better compression and therefore a higher conversion efficiency. This is attributed to the transverse velocity of the electron layers. The transverse current produces a magnetic field which can partially compensate the Coulomb repulsion.

By analyzing a wide range of parameters it has been found that the most crucial magnitude for the efficiency of the scheme is the rising edge of the driving laser pulse. For a laser pulse with a slowly increasing envelope, the spacecharge of the electrons will lead to massive broadening of the electron bunch. In this case, a good efficiency for coherent scattering cannot be achieved. If on the other hand the rising edge is sufficiently steep, the electron bunch will be compressed and accelerated extremely rapidly, so that the bunch reaches relativistic velocities before the spacecharge repulsion can take effect. In this case, the bunch remains compressed and can efficiently be used for coherent Thomson scattering.

Further we observe, that a higher initial foil charge generally favours the scattering efficiency, but leads to a decrease in the frequency conversion ratio. Very recently, there has been an interesting proposal to overcome this drawback. In Ref. [67], it is suggested to reflect the driver pulses from a high density foil during the bunch acceleration. This rids the electron bunch of the driver field, leaving them in a constant motion. Further, before the electrons leave the field region, the reflected part of the pulse acts on the electrons in a way so that their direction of motion is turned exactly in the forward direction. Therefore, the Doppler conversion ratio is increased in this scheme. However, it should also be noted, that the efficiency may again be decreased by this process, as the width or the gradient scale length remains the same, but β_x is increased.

Chapter 5

Conclusions

In this thesis, the physics of ultrashort light pulses was enlightened from various viewpoints.

We introduced a novel mathematical description of few-cycle electromagnetic pulses. The new description enables us to write down accurate analytical closed form expressions even for pulses, where the classical monochromatic approximation clearly fails. We have considered Gaussian and Hermite-Gaussian transverse modes, combined with an arbitrary temporal shape, defined in the centre of the focal spot. It is found that, when assigning these fields directly to the transverse electric field or vector potential, not all temporal shape functions are physically sound. Most of them would produce an infinitely extended field structure containing infinite energy. With the new method, employing the *second potential* $\mathbf{\Psi}$, exactly those pulse shapes that actually possess finite energy are selected. Comprehensive numerical benchmarks were applied to test the validity and accuracy of the new description. Further, the tests readily demonstrate the suitability of the new pulse representation for numerical simulations.

The theory of high harmonics generation (HHG) in the highly relativistic regime was reviewed and extended systematically. The foundations of the popular relativistically oscillating mirror (ROM) model in its refined version [45] have been discussed and newly laid. The model has been extended by the novel concept of *higher order γ-spikes*, demonstrating the possibility of different spectra even within the supposedly well-understood model. In addition, a variant of the ROM model, the totally reflecting oscillating mirror (TROM), has been introduced. Though its physical realization might be difficult, the comparison between the TROM and the ROM model should bring greater clarity into the ongoing discussion about models for relativistic harmonic generation.

It has been found that in p-polarized oblique incidence, one can often observe the formation of highly compressed electron bunches in front of the plasma surface. These *nanobunches* emit synchrotron radiation coherently,

and it is seen in PIC simulations that they can contribute the largest part of the HHG. The spectrum can be obtained within an analytical model again, yielding a power law of $\omega^{-6/5}$ in excellent agreement with the numerical results.

Further, the spectral fine structure and the diffraction in a real 3D geometry, aspects that had often been disregarded so far, were examined closely in this thesis. We have found that the fine structure in the highly relativistic regime serves as an excellent plasma diagnostic, containing information about the cycle averaged motion of the electron plasma surface. Diffraction phenomena can be exploited as *spatial spectral filters*.

The *coherent focusing of harmonics* has been investigated in a realistic geometry. Due to the temporal focusing provided by the HHG mechanism, it should be possible to achieve focal intensities that exceed the one of the generating laser by more than three orders of magnitude.

An alternative scheme for the frequency upconversion of ultrashort, ultraintense laser pulses has been discussed: coherent Thomson scattering at electron layers compressed by the relativistic snowplough effect. It is found, that the rising edge of the driving laser pulse is crucial for a successful realization of this scheme. Provided a sufficiently powerful laser pulse with an extremely steep rising edge is available, this method may offer a great deal of control over the generated radiation.

Appendix A

Analytical Techniques

A.1 Stationary Phase Method

In this section, the asymptotic evaluation of integrals via the stationary phase method is explained. The method has e.g. been applied to diffraction integrals and the calculation of synchrotron spectra and plays a vital role in the theory of high harmonics generation at overdense plasma surfaces. For a comprehensive introduction to this method and related ones, consider e.g. the book by Wong [68]. Here, we describe the method briefly with the applications from section 3.1 in mind.

We are interested in integrals of the form

$$F(\omega) = \int_{-\infty}^{\infty} g(t)\, \exp\left[i\,\omega\, f(t)\right]\, dt, \tag{A.1}$$

where $g(t)$ and $f(t)$ are assumed to be smooth functions. We want to find an asymptotic approximation for $F(\omega)$ in the limit of big ω. Then, the rapidly oscillating integrand cancels everywhere except for the regions of "stationary phase" where $df(t)/dt \approx 0$.

In the simplest case, we can find a set of well separated points $\{t_k\}$ on the real axis where $df(t_k)/dt = 0$ and $d^2f(t_k)/dt^2 \neq 0$. Then $f(t)$ and $g(t)$ can be Taylor expanded around these points: $f(t \approx t_k) \approx a_k + b_k(t - t_k)^2$ and $g(t \approx t_k) \approx c_k$. Now, the integral can be evaluated analytically:

$$\begin{aligned} F(\omega) &\approx \sum_k c_k e^{i\omega a_k} \int_{-\infty}^{\infty} \exp\left[i\,\omega\, b_k (t - t_k)^2\right]\, dt \\ &= \sqrt{\frac{\pi}{i\omega}} \sum_k b_k^{-1/2} c_k\, e^{i\omega a_k} \end{aligned} \quad .$$

It can be seen that the behaviour of the integral depends on two factors. The first factor scales $\propto \omega^{-1/2}$ and constitutes a spectral envelope, whereas the sum determines if the contributions from each stationary point interfere

positively or negatively and is thus responsible for the structure of the single "harmonic" lines. This sort of behaviour also extends to the more complicated cases discussed below, but the envelope factor varies sensitively according to the exact structure of the stationary phase points. Let us now go on to discuss the relevant cases.

A.1.1 First order γ-spikes

Taking a look at the integrals that we encounter in the models presented in Section 3.1, we find that none of them ever contains points where the condition $df(t)/dt = 0$ is exactly fulfilled. It is possible to understand this in terms of physics. The phase functions $f(t)$ in the models are always connected to the difference between the trajectory of a point, that is somehow connected to the plasma motion and the motion of the emitted light wave. Since the plasma cannot be faster than light, $f(t)$ is strictly monotonic, consequently $df/dt \neq 0$.

Still it is possible to apply the stationary phase method by considering points where $df(t)/dt \approx 0$. Technically, this can be viewed as a region where two saddle points, that are located in the complex plane slightly off the real axis, closely merge.

The ROM model, as discussed in Sec. 3.1.2 leads us to integrals of the sort

$$F_{\pm}(\omega) = \int \exp\left[i\left(t(\omega \pm \omega_0) + x(t)(\omega \mp \omega_0)\right)\right]\,(1 + \dot{x}(t))\,dt. \tag{A.2}$$

This integral has to be handled with attention: Note that although $\omega \gg \omega_0$ is assumed, we must not neglect ω_0 in the exponent. The reason for this will become evident later.

The Taylor expansion of $x(t)$ around the velocity maximum can be written down as $x(t) = -vt + \alpha t^3/3$. In the case $\alpha \neq 0$, we speak about a "γ-spike of the order 1". In the case, when $\alpha = 0$, higher orders of the Taylor expansion have to be considered. It is discussed in subsection A.1.2.

We shift the stationary phase point to $t_0 = 0$ without loss of generality here, as we are not interested in absolute phase terms. Using the abbreviation $\delta = 1 - v \approx 1/(2\gamma^2)$, we get $F(\omega) = F_1(\omega) + F_2(\omega)$ with

$$\begin{aligned} F_1(\omega) &= \delta \int \exp\left[i\left(t\left(\delta\omega \pm (2-\delta)\omega_0\right) + \alpha(\omega \mp \omega_0)\frac{t^3}{3}\right)\right] dt \\ F_2(\omega) &= \alpha \int t^2 \exp\left[i\left(t\left(\delta\omega \pm (2-\delta)\omega_0\right) + \alpha(\omega \mp \omega_0)\frac{t^3}{3}\right)\right] dt \end{aligned}. \tag{A.3}$$

By now it should become clear why F_2 and the above mentioned ω_0-terms could not be neglected: We want to presume $\omega \gg \omega_0$, but not $\delta\omega \gg \omega_0$. Later on, we may neglect ω_0 compared to ω and δ compared to 1.

F_1 and F_2 can now be expressed in terms of the well-known Airy function $\mathrm{Ai}(x) \equiv (2\pi)^{-1} \int_{-\infty}^{\infty} \exp\left(i\left(xt + t^3/3\right)\right) dt$:

$$F_1(\omega) = \frac{2\pi\delta}{\sqrt[3]{\alpha\left(\omega \mp \omega_0\right)}} \mathrm{Ai}\left(\xi\right) \tag{A.4}$$

$$F_2(\omega) = \frac{-2\pi\xi}{\omega \mp \omega_0} \mathrm{Ai}\left(\xi\right). \tag{A.5}$$

with $\xi = \left(\delta\omega \pm (2-\delta)\omega_0\right) / \left(\alpha\left(\omega \mp \omega_0\right)\right)^{1/3}$. For the calculation of F_2, we made use of $\mathrm{Ai}''(x) = x\mathrm{Ai}(x)$. After taking the sum of F_1 and F_2, the $\omega^{-1/3}$ terms cancel and only the $\omega^{-4/3}$ term remains, which represents the leading order now:

$$F_{\pm}(\omega) = \frac{\pm 4\pi}{\sqrt[3]{\alpha}\left(\omega \mp \omega_0\right)^{4/3}} \mathrm{Ai}\left(\xi\right). \tag{A.6}$$

Taking the absolute square yields the famous $-8/3$-power law spectrum.

For the TROM model (section 3.1.3), the integral looks a bit different:

$$F_{\pm}(\omega) = \int \exp\left[i\left(t(\omega \pm \omega_0) + x(t)(\omega \mp \omega_0)\right)\right]\left(1 - \dot{x}(t)\right) dt. \tag{A.7}$$

The integration works in complete analogy to the case shown above, but in this case, the $\omega^{-1/3}$-terms do not cancel out. Therefore, we obtain in highest order:

$$F_{\pm}(\omega) = \frac{4\pi}{\sqrt[3]{\alpha\left(\omega \mp \omega_0\right)}} \mathrm{Ai}\left(\xi\right). \tag{A.8}$$

In the case of CSE (section 3.1.4), the integral is of the sort:

$$F(\omega) = \int \dot{y}(t) \exp\left[-i\omega\left(t + x(t)\right)\right] dt. \tag{A.9}$$

To get some meaningful result out of this, we need to make an assumption about the relation between $y(t)$ and $x(t)$. We assume, that during the time of harmonic generation, the absolute velocity $(\dot{x}^2 + \dot{y}^2)^{1/2}$ is approximately constant and close to the speed of light. This is reasonable in the ultra-relativistic regime. With this assumption, the stationary phase points are exactly the points, where $\dot{y}$ vanishes and the electrons move towards the observer. Now we can Taylor expand $\dot{y}(t) = \alpha_0 t$ and $x(t) = -vt + \alpha_1 t^3/3$. Substituting into Eq. (A.9) yields:

$$F(\omega) = \alpha_0 \int t \exp\left[i\left(-\omega\delta t - \omega\alpha_1 \frac{t^3}{3}\right)\right] dt, \tag{A.10}$$

where $\delta = 1 - v$ as above. Again, the result can be expressed in terms of the Airy function:

$$F(\omega) = \frac{-2\pi\alpha_0 i}{\left(\alpha_1\omega\right)^{2/3}} \mathrm{Ai'}\left(\frac{\delta\omega^{2/3}}{\sqrt[3]{\alpha_1}}\right). \tag{A.11}$$

A.1.2 Higher order γ-spikes

In the previous subsection (Sec. A.1.1), we dealt with the case when the transverse velocity of the electrons pass zero. Together with the assumption of ultrarelativistic motion this lead us to the Taylor expansion $x(t) = -vt + \alpha t^3/3$. In this section we deal with the possibility, that the transverse velocity does not go through, but touches zero, so that the third order of $x(t)$ vanishes.

In general, if the first $2n$ orders of $x(t)$ vanish, it can be written: $x(t) = -vt + \alpha t^{2n+1}/(2n+1)$. We refer to this case as a "γ-spike of the order n". Inserting this into Eq. A.2 yields:

$$\begin{aligned} F_1(\omega) &= \delta \int \exp\left[i\left(t\left(\delta\omega \pm (2-\delta)\omega_0\right) + \alpha(\omega \mp \omega_0)\frac{t^{2n+1}}{2n+1}\right)\right] dt \\ F_2(\omega) &= \alpha \int t^{2n} \exp\left[i\left(t\left(\delta\omega \pm (2-\delta)\omega_0\right) + \alpha(\omega \mp \omega_0)\frac{t^{2n+1}}{2n+1}\right)\right] dt \end{aligned} . \tag{A.12}$$

These integrals can now be expressed by a generalized Airy function, which we define as $\mathrm{gAi}_n(x) \equiv (2\pi)^{-1} \int_{-\infty}^{\infty} \exp\left[i\left(xt + t^{2n+1}/(2n+1)\right)\right] dt$. Note that for $n = 1$ we retain the Airy function and for $n = 2$ we obtain a special case of the canonical swallowtail integral [53]. Since the $\mathrm{gAi}_n(x)$ are not available in general purpose numerical libraries, their numerical computation is explained in Sec. B.3.

In analogy to the Airy function, the $\mathrm{gAi}_n(x)$ fulfil ODEs: $d^{2n}\mathrm{gAi}_n(x)/dx^{2n} + (-1)^n x\,\mathrm{gAi}_n(x) = 0$. Exploiting this, F_1 and F_2 become

$$F_1(\omega) = \frac{2\pi\delta}{\sqrt[2n+1]{\alpha(\omega \mp \omega_0)}}\,\mathrm{gAi}_n(\xi) \tag{A.13}$$

$$F_2(\omega) = \frac{-2\pi\xi}{\omega \mp \omega_0}\,\mathrm{gAi}_n(\xi), \tag{A.14}$$

where $\xi = \left(\delta\omega \pm (2-\delta)\omega_0\right) / \left(\alpha\left(\omega \mp \omega_0\right)\right)^{1/(2n+1)}$. After again taking the sum of F_1 and F_2, the $\omega^{-1/(2n+1)}$ terms cancel and what remains is:

$$F_\pm(\omega) = \frac{\pm 4\pi}{\sqrt[2n+1]{\alpha}(\omega \mp \omega_0)^{2n+2/2n+1}}\,\mathrm{gAi}_n(\xi). \tag{A.15}$$

In complete analogy the TROM model, represented by the integral (A.7), yields:

$$F_\pm(\omega) = \frac{4\pi}{\sqrt[2n+1]{\alpha(\omega \mp \omega_0)}}\,\mathrm{gAi}_n(\xi). \tag{A.16}$$

Finally we calculate the CSE integral (A.9) for higher orders of the γ-spike. Here, this means $\dot{y}(t) = \alpha_0 t^n$ and, consequently, $x(t) = -vt +$

$\alpha_1 t^{2n+1}/(2n+1)$. Since this works in complete analogy to the hitherto discussed cases, we just present the result:

$$F(\omega) = \frac{-2\pi\alpha_0 i^n}{(\alpha_1\omega)^{n+1/2n+1}} \frac{d^n \mathrm{gAi}_n(\xi)}{d\xi^n}, \tag{A.17}$$

wherein $\xi = \omega^{2n/2n+1}\delta/\alpha_1^{1/(2n+1)}$.

A.2 Analytic Signal

Here the analytic signal, a powerful tool from signal theory, is explained in brief[1]. In the present work it has been used to derive an analytical finite energy solution of the 3D scalar wave equation in paraxial approximation.

Given a real-valued function $f(t)$, we are looking for a complex function $f_a(t)$ that fulfils two conditions:

1. Its real part is identical with $f(t)$: $\mathrm{Re}\,[f_a(t)] = f(t)$.
2. The Fourier transform of $f_a(t)$ must not contain any negative frequency components: $\tilde{f}_a(\omega < 0) = 0$.

$f_a(t)$ is then called the *analytic signal*. One well known example is the exponential function of an imaginary argument. One can easily verify, that for $f(t) = \cos(\Omega t)$ with $\Omega > 0$ the corresponding analytic signal is $f_a(t) = \exp(i\Omega t)$.

There is a straightforward way to obtain $f_a(t)$ for any real signal $f(t)$. At first, the Fourier transform of $f(t)$ is computed:

$$\tilde{f}(\omega) = \int_{-\infty}^{\infty} f(t)\, e^{-i\omega t}\, dt.$$

Then, we identify $\tilde{f}_a(\omega) = 2\theta(\omega)\tilde{f}(\omega)$, and finally the analytic signal can be obtained by applying the inverse Fourier transformation:

$$f_a(t) = \frac{1}{2\pi}\int_{-\infty}^{\infty} \tilde{f}_a(\omega)\, e^{i\omega t}\, d\omega = \frac{1}{\pi}\int_{0}^{\infty} \tilde{f}(\omega)\, e^{i\omega t}\, d\omega.$$

From this algorithm it is immediately clear that f_a fulfils condition 2. Recalling the symmetry property $\overline{\tilde{f}(-\omega)} = \tilde{f}(\omega)$, that is valid for all real-valued $f(t)$, it is also not hard to see that condition 1 is fulfilled.

The above recipe allows us to evaluate the analytic signal numerically via fast Fourier transformation (FFT) algorithms and in some cases also analytically. Fig. A.1 shows the analytic signal of a Gaussian pulse as an example. Note that the absolute value of the analytic signal represents a

[1] For a more comprehensive discussion, consider e.g. Ref. [69].

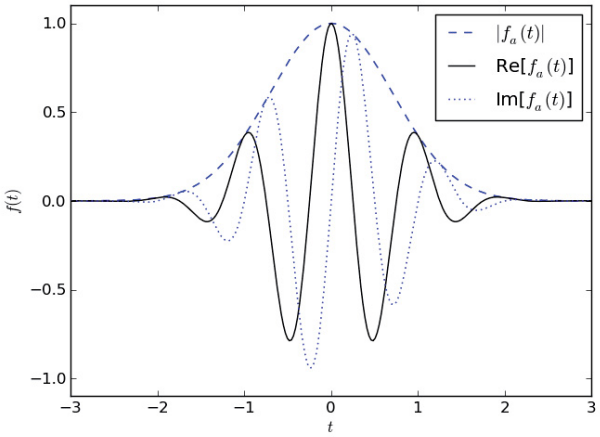

Figure A.1: Analytic signal of a Gaussian pulse $f(t) = \mathrm{Re}\,[f_a(t)] = \cos(2\pi t)\exp\left(-t^2\right)$

smooth envelope to the Gaussian pulse. This is no coincidence but a general property of the analytic signal. Therefore, determining the absolute value of the analytic signal is a natural way to obtain the slowly varying envelope of a given real signal with a well-defined carrier frequency.

For our purpose, it is needed to calculate the analytic signal of a complex-valued argument $t' = t + iu$. Even in this case, the procedure is basically the same. We find $\tilde{f}_a(\omega) = 2\theta(\omega)\exp(-u\omega)\,\tilde{f}(\omega)$. The additional exponential factor thus causes no trouble for $u > 0$, as it is always the case in the applications in chapter 2.

Appendix B

Numerical Techniques

B.1 Particle-in-Cell (PIC) Simulation

In physics, simulations provide a tool to bridge the gap between analytical theory and experiment. While experiments of course are the foundation of empirical science, especially in plasma physics diagnostics are often very indirect, and it is difficult to gain immediate insight from experiments alone. In addition to this, modification of single parameters may require big efforts and costs, but it can quickly be performed within a simulation. Analytical theory on the other hand yields a profound understanding of physical processes. However, especially plasma theory has to rely on extensive approximations and assumptions, so that it is often hard to directly compare its results to real experiments.

For these reasons, simulations have over the last decades become an indispensable tool in plasma physics. One of the most powerful simulation tools for plasma physics known today are PIC (Particle-in-Cell) simulations. Especially in the field of laser-plasma interaction, there is now barely a publication, in which the results are *not* backed up by PIC simulations.

The PIC algorithm is based on the Maxwell equations and the Vlasov equation

$$\partial_t f + \frac{\mathbf{p}}{m\sqrt{1+\mathbf{p}^2}}\partial_{\mathbf{x}} f + \frac{\mathbf{F}}{m}\partial_{\mathbf{p}} f = 0, \tag{B.1}$$

which provides the full kinetic description of a collisionless plasma. Therefore, PIC codes are - unlike hydro-codes, which rely on momenta equation derived from (B.1) - capable of dealing with highly non-thermal plasmas, which play a crucial role in laser-plasma interaction. In contrast to so called Vlasov codes, PIC codes do not directly sample the particle distribution function $f(\mathbf{x}, \mathbf{p}, t)$ on a Eulerian mesh. Instead, they sample the distribution with so called macroparticles: $f(\mathbf{x}, \mathbf{p}, t) = \sum_p W_p\, S(\mathbf{x} - \mathbf{x}_p(t), \mathbf{p} - \mathbf{p}_p(t))$, where W_p refers to the weight and S to the shape function of the individual particles. This picture is highly intuitive: The macroparticles correspond to

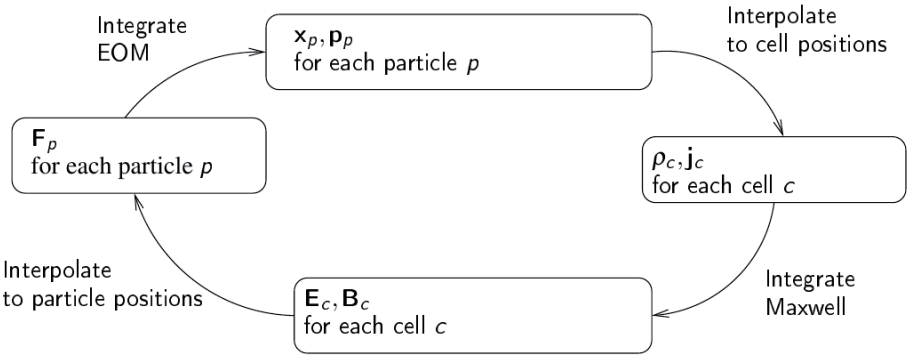

Figure B.1: Computational cycle of a PIC simulation

"clouds" of real particles, which simply move according to the laws of mechanics. Besides its intuitive simplicity, this model has the advantage of being computationally effective, since sampling of empty phase space regions is avoided.

Let us now have a look at how the PIC algorithm works. A simulation run starts by initializing the physical constituents (laser fields, plasma particles) in the simulation box[1]. After that, the fields and particles are propagated in time step by step. Therefore, the computational cycle (see Fig. B.1) is executed repeatedly: From the momenta $\mathbf{p}_p$ and positions $\mathbf{x}_p$ of the macro-particles, currents $\mathbf{j}_c$ and charge densities ρ_c are calculated at each cell[2] by an interpolation algorithm. Using these values, the electric and magnetic fields $\mathbf{E}_c$ and $\mathbf{B}_c$ are propagated in time by a Maxwell solver. Interpolating these fields to the particle positions, the forces $\mathbf{F}_p$ on the particles are computed. Finally, the particle positions and momenta are updated and the cycle starts again.

Several variants of this algorithm exist, varying e.g. in the dimensionality of the considered system, the system of equations they are based on (whether or not the equations of motion are relativistic, magnetic fields are included or only electric, etc.) and the numerical algorithms used to propagate fields and particles. Further, there are a lot of possible extensions to the basic algorithm like including ionization effects, collisions, etc..

In this work, the code VLPL (Virtual Laser Plasma Laboratory) [29] by Alexander Pukhov has been used, a fully relativistic PIC code, which exists in 1D, 2D and 3D versions. Also, some extensions have been implemented and applied, e.g. for initializing ultra-short, focused laser pulses and for simulating in Lorentz transformed systems.

[1] the spatial region to be simulated
[2] point of the spatial simulation grid

B.2 Lorentz Transformation to Describe Oblique Incidence in 1D

In laser-plasma theory, it is often convenient to describe things in a one dimensional (1D) slab geometry, i.e. all spatial derivatives perpendicular to the optical axis are neglected. For not too small laser focal spot sizes, this is very often a reasonable approximation and leads to great simplifications in numerical as well as analytical theory. In numerical computations, the grid size can be reduced by orders of magnitude, allowing for higher resolution in the critical dimension. In analytical calculations, it sometimes enables us to give closed form solutions and straightforward, comprehensible models. Whereas it is obvious that the 1D treatment can be employed in situations of normal laser incidence, it can also be extended to oblique laser incidence. Therefore, as shown by Bourdier in Ref. [70], a Lorentz transformation does the job.

From the lab frame $\mathcal{L}$, we transform to the inertial frame $\mathcal{S}$, in which the laser is normally incident. Let the light wave in $\mathcal{L}$ be described by the frequency 4-vector $\left(\omega_0^{\mathcal{L}},\, ck_x^{\mathcal{L}},\, ck_y^{\mathcal{L}},\, 0\right) = \omega_0^{\mathcal{L}}\,(1,\, \cos\alpha,\, \sin\alpha,\, 0)$, wherein x denotes the direction normal to the surface and α is the angle of incidence. In $\mathcal{S}$, we claim $ck_y^{\mathcal{S}} \stackrel{!}{=} 0$. Thus, the Lorentz transformation is given by the matrix

$$\Lambda = \begin{pmatrix} \gamma & 0 & -\beta\gamma & 0 \\ 0 & 1 & 0 & 0 \\ -\beta\gamma & 0 & \gamma & 0 \\ 0 & 0 & 0 & 1 \end{pmatrix}, \tag{B.2}$$

with $\beta = \sin\alpha$ and $\gamma = (\cos\alpha)^{-1}$. Now, we can derive all interesting magnitudes. In the frame $\mathcal{S}$, the plasma is streaming with the velocity $v_y^{\mathcal{S}} = -c\beta$, the laser wavelength is altered by $\lambda^{\mathcal{S}} = \gamma\lambda^{\mathcal{L}}$ and therefore the corresponding critical density changes to $n_{cr}^{\mathcal{S}} = \gamma^{-2} n_{cr}^{\mathcal{L}}$. The electron density itself changes to $n^{\mathcal{S}} = \gamma n^{\mathcal{L}}$, thus the *normalized* density

$$\bar{n}^{\mathcal{S}} \equiv \frac{n^{\mathcal{S}}}{n_{cr}^{\mathcal{S}}} = \gamma^3 \bar{n}^{\mathcal{L}} \tag{B.3}$$

scales even with γ^3.

Especially in the theory of harmonics generation (chapter 3) this transformation is often used, so it is handy to have these formulae down pat.

B.3 Numerical Calculation of the Generalized Airy Function

This section explains the numerical computation of the integral

$$\mathrm{gAi}_n(x) \equiv \frac{1}{2\pi} \int_{-\infty}^{\infty} e^{i\left(xt + \frac{t^{2n+1}}{2n+1}\right)} dt. \tag{B.4}$$

The unmindful immediate application of a trapezoidal formula would fail here due to the rapidly oscillating integrand, which further does not vanish at infinity. The integral only converges because of the steadily decreasing oscillation period for $t \to \pm\infty$.

However, a simple trick can be applied to calculate the integral numerically: We shift the contour of integration along the imaginary axis by a margin of $a > 0$. Due to Cauchy's integral theorem, this will not change the results[3]. Next, the symmetry of the integrand can be exploited, so that the contour of integration can be halved. We obtain:

$$\mathrm{gAi}_n(x) = \frac{1}{\pi}\int_0^\infty \exp\left[-\mathrm{Im}\left(f(x,t)\right)\right] \times \cos\left[\mathrm{Re}\left(f(x,t)\right)\right]\, dt \quad \text{(B.5)}$$

$$f(x,t) = (t+ia)x + \frac{(t+ia)^{2n+1}}{2n+1}. \quad \text{(B.6)}$$

Note that, since $a > 0$, $f(x, t)$ possesses the highly desirable property $\lim_{t\to\infty}\left[\mathrm{Im}\left(f(x,t)\right)\right] = +\infty$. This means, that the integrand vanishes exponentially for large t, and we can approximate (B.5) with a trapezoidal formula.

Since a does not affect the value of the integral, it can be chosen in a way so as to minimize the computational effort. For too small a, the integrand vanishes only slowly for $t \to \infty$ so that the numerical upper boundary would have to be very high. For too large a, the integrand oscillates more rapidly, so that the time step would have to be very small. Our experience showed, that the best choice for a depends mainly on the order n of the function. For $n \leq 2$ we found $a = 1$ a good choice, whereas for $n > 2$, smaller a work better.

[3]For large t, the contours connecting the real axis to the new integration path yield vanishing contributions.

Bibliography

[1] D. Strickland and G. Mourou. Compression of amplified chirped optical pulses. *Optics Communications*, 56(3):219–221, 1985.

[2] A. Dubietis. Powerful femtosecond pulse generation by chirped and stretched pulse parametric amplification in BBO crystal. *Optics Communications*, 88(4-6):437–440, 1992.

[3] Wiliam L. Kruer. *The Physics of Laser Plasma Interaction.* 1987.

[4] Paul Gibbon. *Short pulse laser interactions with matter : an introduction.* Imperial College Press, London, 2005.

[5] Ed Gerstner. Laser physics: Extreme light. *Nature*, 446(7131):16–18, 2007.

[6] Julian Schwinger. On gauge invariance and vacuum polarization. *Physical Review*, 82(5):664–679, 1951.

[7] T. Tajima and J. Dawson. Laser electron accelerator. *Phys. Rev. Lett.*, 43(4):267–270, 1979.

[8] A. Pukhov, S. Gordienko, S. Kiselev, and I. Kostyukov. The bubble regime of laser plasma acceleration: monoenergetic electrons and the scalability. *Plasma Physics and Controlled Fusion*, 46(12B):B179, 2004.

[9] J. Faure, Y. Glinec, A. Pukhov, S. Kiselev, S. Gordienko, E. Lefebvre, J. P. Rousseau, F. Burgy, and V. Malka. A laser-plasma accelerator producing monoenergetic electron beams. *Nature*, 431(7008):541–544, Sep 2004.

[10] D. an der Brügge and A. Pukhov. Ultrashort focused electromagnetic pulses. *Phys. Rev. E*, 79(1):016603, Jan 2009.

[11] D. an der Brügge and A. Pukhov. Enhanced relativistic harmonics by electron nanobunching. *Physics of Plasmas*, 17(3):033110, 2010.

[12] D. an der Brügge and A. Pukhov. Propagation of relativistic surface harmonics radiation in free space. *Physics of Plasmas*, 14(9):093104–+, September 2007.

[13] D. an der Brügge and A. Pukhov. SPIE Europe conference proceedings 2009, prague, czech republic. In D. Jaroszynski and A. Rousse, editors, *Harnessing relativistic plasma waves as novel radiation sources from terahertz to x-rays and beyond*, Bellingham, Wash., 6 May 2009. SPIE (Society).

[14] G. A. Mourou, C. L. Labaune, M. Dunne, N. Naumova, and V. T. Tikhonchuk. Relativistic laser-matter interaction: from attosecond pulse generation to fast ignition. *Plasma Physics and Controlled Fusion*, 49(12B):B667–B675, 2007.

[15] D. J. Jones, S. A. Diddams, J. K. Ranka, A. Stentz, R. S. Windeler, J. L. Hall, and S. T. Cundiff. Carrier-Envelope Phase Control of Femtosecond Mode-Locked Lasers and Direct Optical Frequency Synthesis. *Science*, 288(5466):635–639, 2000.

[16] L. Xu, Ch. Spielmann, A. Poppe, T. Brabec, F. Krausz, and T. W. Hänsch. Route to phase control of ultrashort light pulses. *Opt. Lett.*, 21(24):2008–2010, 1996.

[17] Y. I. Salamin and Ch. H. Keitel. Electron acceleration by a tightly focused laser beam. *Phys. Rev. Lett.*, 88(9):095005, Feb 2002.

[18] Ch. Varin, M. Piché, and M. A. Porras. Acceleration of electrons from rest to gev energies by ultrashort transverse magnetic laser pulses in free space. *Phys. Rev. E*, 71(2):026603, Feb 2005.

[19] Yousef I. Salamin. Electron acceleration from rest in vacuum by an axicon gaussian laser beam. *Phys. Rev. A*, 73(4):043402, Apr 2006.

[20] A. Karmakar and A. Pukhov. Collimated attosecond gev electron bunches from ionization of high-z material by radially polarized ultra-relativistic laser pulses. *Laser and Particle Beams*, 25(03):371–377, 2007.

[21] Alexander Pukhov. Relativistic plasmas: X-rays in a flash. *Nature Physics*, 2(7):439–440, Jul 2006.

[22] N. M. Naumova, J. A. Nees, B. Hou, G. A. Mourou, and I. V. Sokolov. Isolated attosecond pulses generated by relativistic effects in a wavelength-cubedfocal volume. *Opt. Lett.*, 29(7):778–780, 2004.

[23] B. Dromey, D. Adams, R. Horlein, Y. Nomura, S. G. Rykovanov, D. C. Carroll, P. S. Foster, S. Kar, K. Markey, P. McKenna, D. Neely, M. Geissler, G. D. Tsakiris, and M. Zepf. Diffraction-limited performance and focusing of high harmonics from relativistic plasmas. *Nature Physics*, 5(2):146–152, Feb 2009.

[24] P. B. Corkum and Ferenc Krausz. Attosecond science. *Nat Phys*, 3(6):381–387, Jun 2007.

[25] L. E. Helseth. Strongly focused polarized light pulse. *Phys. Rev. E*, 72(4):047602, Oct 2005.

[26] M. Lax, W. H. Louisell, and W. B. McKnight. From maxwell to paraxial wave optics. *Phys. Rev. A*, 11(4):1365–1370, Apr 1975.

[27] Miguel A. Porras. Ultrashort pulsed gaussian light beams. *Phys. Rev. E*, 58(1):1086–1093, Jul 1998.

[28] M. Abramowitz and I. A. Stegun. *Handbook of Mathematical Functions with Formulas, Graphs, and Mathematical Tables.* Dover, New York, 1972.

[29] A. Pukhov. Three-dimensional electromagnetic relativistic particle-in-cell code vlpl (virtual laser plasma lab). *Journal of Plasma Physics*, 61(03):425–433, 1999.

[30] P. B. Corkum and F. Krausz. Attosecond science. *Nature Physics*, 3(6):381–387, 2007.

[31] G. D. Tsakiris, K. Eidmann, J. Meyer-ter-Vehn, and F. Krausz. Route to intense single attosecond pulses. *New Journal of Physics*, 8(1):19, 2006.

[32] R. Ramis. MULTI — a computer code for one-dimensional multigroup radiation hydrodynamics. *Computer Physics Communications*, 49(3):475–505, 1988.

[33] R. L. Carman, D. W. Forslund, and J. M. Kindel. Visible harmonic emission as a way of measuring profile steepening. *Phys. Rev. Lett.*, 46(1):29–32, Jan 1981.

[34] R. L. Carman, C. K. Rhodes, and R. F. Benjamin. Observation of harmonics in the visible and ultraviolet created in co2-laser-produced plasmas. *Phys. Rev. A*, 24(5):2649–2663, Nov 1981.

[35] B. Bezzerides, R. D. Jones, and D. W. Forslund. Plasma mechanism for ultraviolet harmonic radiation due to intense co2 light. *Phys. Rev. Lett.*, 49(3):202–205, Jul 1982.

[36] D. von der Linde, T. Engers, G. Jenke, P. Agostini, G. Grillon, E. Nibbering, A. Mysyrowicz, and A. Antonetti. Generation of high-order harmonics from solid surfaces by intense femtosecond laser pulses. *Phys. Rev. A*, 52(1):R25–R27, 1995.

[37] S. Kohlweyer. Harmonic generation from solid-vacuum interface irradiated at high laser intensities. *Optics Communications*, 117(5-6):431–438, 1995.

[38] A. Tarasevitch, A. Orisch, D. von der Linde, Ph. Balcou, G. Rey, J.-P. Chambaret, U. Teubner, D. Klöpfel, and W. Theobald. Generation of high-order spatially coherent harmonics from solid targets by femtosecond laser pulses. *Phys. Rev. A*, 62(2), 2000.

[39] S. V. Bulanov, N. M. Naumova, and F. Pegoraro. Interaction of an ultrashort, relativistically strong laser pulse with an overdense plasma. *Physics of Plasmas*, 1(3):745, 1994.

[40] R. Lichters, J. Meyer ter Vehn, and A. Pukhov. Short-pulse laser harmonics from oscillating plasma surfaces driven at relativistic intensity. *Phys. Plasmas*, 3(9):3425–3437, 1996.

[41] D. von der Linde and K. Rzàzewski. High-order optical harmonic generation from solid surfaces. *Applied Physics B: Lasers and Optics*, 63(5):499–506, 1996.

[42] Paul Gibbon. Harmonic generation by femtosecond Laser-Solid interaction: A coherent "Water-Window" light source? *Phys. Rev. Lett.*, 76(1):50–53, 1996.

[43] F. Brunel. Not-so-resonant, resonant absorption. *Phys. Rev. Lett.*, 59(1):52–55, 1987.

[44] F. Quéré, C. Thaury, P. Monot, S. Dobosz, Ph. Martin, J.-P. Geindre, and P. Audebert. Coherent wake emission of high-order harmonics from overdense plasmas. *Phys. Rev. Lett.*, 96(12):125004, 2006.

[45] T. Baeva, S. Gordienko, and A. Pukhov. Theory of high-order harmonic generation in relativistic laser interaction with overdense plasma. *Phys. Rev. E*, 74(4):046404, 2006.

[46] B. Dromey, M. Zepf, A. Gopal, K. Lancaster, M. S. Wei, K. Krushelnick, M. Tatarakis, N. Vakakis, S. Moustaizis, R. Kodama, M. Tampo, C. Stoeckl, R. Clarke, H. Habara, D. Neely, S. Karsch, and P. Norreys. High harmonic generation in the relativistic limit. *Nature Physics*, 2(7):456–459, Jul 2006.

[47] A. Tarasevitch, R. Kohn, and D. von der Linde. Towards intense attosecond pulses: using two beams for high order harmonic generation from solid targets. *Journal of Physics B: Atomic, Molecular and Optical Physics*, 42(13):134006, 2009.

[48] A. Tarasevitch, K. Lobov, C. Wunsche, and D. von der Linde. Transition to the relativistic regime in high order harmonic generation. *Phys. Rev. Lett.*, 98(10):103902, 2007.

[49] S. Gordienko and A. Pukhov. Scalings for ultrarelativistic laser plasmas and quasimonoenergetic electrons. *Phys. Plasmas*, 12(4):043109, 2005.

[50] Teodora Baeva. *High harmonic generation from relativistic plasma.* PhD thesis, Heinrich-Heine-Universitaet Duesseldorf, May 2008.

[51] T. J. M. Boyd and R. Ondarza-Rovira. Anomalies in universal intensity scaling in ultrarelativistic laser-plasma interactions. *Phys. Rev. Lett.*, 101(12):125004, 2008.

[52] John D. Jackson. *Classical Electrodynamics.* J. Wiley & Sons Inc., 3rd ed. edition, 1998.

[53] J. N. L. Connor, P. R. Curtis, and D. Farrelly. The uniform asymptotic swallowtail approximation: practical methods for oscillating integrals with four coalescing saddle points. *Journal of Physics A: Mathematical General*, 17:283–310, February 1984.

[54] A. Pukhov, T. Baeva, D. an der Brügge, and S. Münster. Relativistic high harmonics and (sub-)attosecond pulses: relativistic spikes and relativistic mirror. *The European Physical Journal D*, 55(2):407–414, 2009.

[55] A. Tarasevitch, C. Dietrich, C. Blome, K. Sokolowski-Tinten, and D. von der Linde. 3/2 harmonic generation by femtosecond laser pulses in steep-gradient plasmas. *Phys. Rev. E*, 68(2):026410, Aug 2003.

[56] Daniel an der Brügge. PIC Simulationen zur Erzeugung Harmonischer an Plasmadichtegradienten mit fs-Laserpulsen. Diploma thesis, Universität Essen, 3 November 2004.

[57] F. Quéré, C. Thaury, J-P. Geindre, G. Bonnaud, P. Monot, and Ph. Martin. Phase properties of laser High-Order harmonics generated on plasma mirrors. *Phys. Rev. Lett.*, 100(9).

[58] S. Gordienko, A. Pukhov, O. Shorokhov, and T. Baeva. Coherent focusing of high harmonics: A new way towards the extreme intensities. *Phys. Rev. Lett.*, 94(10):103903, Mar 2005.

[59] A. Pukhov, T. Baeva, and D. an der Brügge. Relativistic laser plasmas for novel radiation sources. *The European Physical Journal Special Topics*, 175(1):25–33, 2009.

[60] E. Brezin and C. Itzykson. Pair production in vacuum by an alternating field. *Phys. Rev. D*, 2(7):1191–1199, 1970.

[61] E. Esarey, S. K. Ride, and Ph. Sprangle. Nonlinear thomson scattering of intense laser pulses from beams and plasmas. *Phys. Rev. E*, 48(4):3003–3021, Oct 1993.

[62] V. Kulagin, V. A. Cherepenin, and H. Suk. Compression and acceleration of dense electron bunches by ultraintense laser pulses with sharp rising edge. *Physics of Plasmas*, 11(11):5239–5249, 2004.

[63] G. Miyaji, N. Miyanaga, K. Tsubakimoto, K. Sueda, and K. Ohbayashi. Intense longitudinal electric fields generated from transverse electromagnetic waves. *Applied Physics Letters*, 84(19):3855–3857, 2004.

[64] V. Kulagin, V. Cherepenin, Min Hur, and H. Suk. Theoretical investigation of controlled generation of a dense attosecond relativistic electron bunch from the interaction of an ultrashort laser pulse with a nanofilm. *Physical Review Letters*, 99(12), 2007.

[65] B. Qiao, M. Zepf, M. Borghesi, B. Dromey, and M. Geissler. Coherent x-ray production via pulse reflection from laser-driven dense electron sheets. *New Journal of Physics*, 11(10):103042, 2009.

[66] J. Meyer-ter-Vehn and H.-C. Wu. Coherent thomson backscattering from laser-driven relativistic ultra-thin electron layers. *The European Physical Journal D*, 55(2):433–441, 2009.

[67] H.-C. Wu, J. Meyer-ter-Vehn, J. Fernández, and B. M. Hegelich. Uniform Laser-Driven relativistic electron layer for coherent thomson scattering. *Physical Review Letters*, 104(23), 2010.

[68] R. Wong. *Asymptotic approximations of integrals*. Society for Industrial and Applied Mathematics, Philadelphia, 2001.

[69] Ronald N. Bracewell. *The Fourier Transform and Its Applications*. McGraw-Hill, New York, 2nd edition, 1986.

[70] A. Bourdier. Oblique incidence of a strong electromagnetic wave on a cold inhomogeneous electron plasma - Relativistic effects. *Physics of Fluids*, 26:1804–1807, July 1983.

Danksagung

Schließlich möchte ich mich bei allen Menschen bedanken, die zum Zustandekommen dieser Arbeit auf die eine oder andere Weise beigetragen haben.

Zuerst ist da selbstverständlich mein Betreuer Prof. Alexander Pukhov, dem ich für seine geduldige und hilfreiche Unterstützung danken möchte. Ich denke, ich habe viel von Ihnen gelernt, sowohl auf fachlicher Ebene als auch über die klare und eingängige Präsentation wissenschaftlicher Ergebnisse. Ich bedanke mich auch bei Prof. Karl-Heinz Spatschek für die Übernahme der Zweitbetreuung und bei Prof. Gerhard Paulus, dafür dass er meine Arbeit begutachtet.

Dann bedanke ich mich bei allen derzeitigen und ehemaligen Kollegen, die mir nicht selten durch anregende Diskussionen Inspiration und Motivation gegeben haben. Namentlich nennen muss ich hier wenigstens Dr. Naveen Kumar, Tobias Tückmantel, Sebastian Münster, Tongpu Yu, Dr. Anupam Karmakar, Dr. Adriane Schelin und natürlich Dr. Christoph Karle und Dr. Götz Lehmann von der anderen Seite des Flures, die mir oft auch beim Lösen vertrackter Computerprobleme helfen konnten.

Ich danke auch Michael Behmke, Prof. Georg Pretzler und allen Beteiligten an der erfolgreichen Kooperation aus Düsseldorf und Jena, die zu den Ergebnissen geführt hat, welche in Abschnitt 3.2 dieser Arbeit vorgestellt wurden. Ebenfalls bedanke ich mich bei den Mitgliedern und Organisatoren des Graduiertenkollegs 1203, welches dazu beigetragen hat, mein Verständnis von Plasmaphysik auch in der Breite zu erweitern.

Frau Elvira Gröters, die mich in allen bürokratischen Aspekten meiner Arbeit umfassend unterstützt hat, kann ich natürlich nicht unerwähnt lassen, sowie Eugen Bleile und Herrn Eckhard Zügge, die für das fast immer reibungslose Funktionieren der Rechnersysteme verantwortlich waren. Herr Zügge ist traurigerweise letztes Jahr verstorben.

Nicht zuletzt ist es mein Anliegen, mich bei meinen Freunden und bei meiner Familie zu bedanken, dafür dass sie mein Leben während der letzten Jahre auch außerhalb der wissenschaftlichen Arbeit lebenswert gemacht haben. Vor allem meine liebe Freundin Alexandra Kessler, die mich selbst dann geduldig erträgt, wenn ich gerade noch ein physikalisches Problem im Kopf herumwälze und daher eigentlich unausstehlich bin, muss hier genannt werden.

Erklärung

Hiermit erkläre ich, dass ich die vorliegende Dissertation selbstständig verfasst habe. Dabei habe ich keine anderen als die angegebenen Quellen und Hilfsmittel benutzt, Zitate wurden kenntlich gemacht.

Düsseldorf, den